# Surface treatment in a cathodic arc plasma : Key step for interface engineering.

SCHONJAHN, Cornelia.

---

**Published version**

SCHONJAHN, Cornelia. (2001). Surface treatment in a cathodic arc plasma : Key step for interface engineering. Doctoral, Sheffield Hallam University (United Kingdom)..

---

# Surface treatment in a cathodic arc plasma - key step for interface engineering

Cornelia Schönjahn

A thesis submitted in partial fulfilment of the
requirements of Sheffield Hallam University for
the degree of Doctor of Philosophy

February 2001

## Abstract

The effect of substrate surface treatment (substrate sputter cleaning) in a cathodic arc plasma prior to unbalanced magnetron deposition of transition metal nitride coatings on the performance of the coated components has been investigated. In particular the influence of parameters such as ion species, ion energy and exposure time on the changes in substrate surface topography, microstructure and microchemistry were studied employing transmission electron microscopy, energy dispersive X-ray analysis, electron energy loss spectroscopy, X-ray diffraction, atomic force microscopy and optical microscopy. The consequences for both the microstructure of subsequently grown transition metal nitride coatings and their adhesion were elucidated. The relevance for practical applications was demonstrated using the example of dry high-speed milling tests, which showed that an appropriate choice of substrate surface pre-treatment parameters can double the life time of the coated tools. This was found to be due to an improved adhesion as a result of a combination of reduced oxygen incorporation at the interface between coating and substrate and local epitaxial growth of the coating. The latter is promoted by certain substrate surface pre-treatment procedures, which provide clean surfaces with preserved crystallographic order.

# Advanced Studies

The following conferences and workshops were attended during the studies for this thesis:

(I) Elektrochemische and Physikalische Oberflächenbeschichtung, April 1998, Freiberg, Germany

(II) Fourth Sheffield Arc bond Sputtering (ABS) Days, July 1998, Sheffield, UK

(III) 14th International Vacuum Congress, August/ September 1998, Birmingham, UK

(IV) European Materials Research Society (E-MRS) Spring Meeting, Strasbourg, June 1999, France

(V) Fifth Sheffield ABS Days, July 1999, Sheffield, UK

(VI) Institute of Physics Electron Microscopy and Analysis Group Conference (EMAG), August 1999, Sheffield, UK

(VII) American Vacuum Society (AVS) 46th International Symposium, October 1999, Seattle, USA

(VIII) Sixth Sheffield ABS Days, July 2000, Sheffield, UK

(IX) AVS 47th International Symposium, October 2000, Boston, USA

An extremely valuable experience was to be a guest in Professor J.E. Greene's Thin Film Group at the University of Illinois at Urban Champaign, USA and the close collaboration with the Center for Microanalysis of Materials thanks to Professor I. Petrov.

# Publications & Patents

(I) C. Schönjahn, H. Paritong, L.A. Donohue, W.-D. Münz, R.D. Twesten, and I. Petrov. Influence of $Cr^+$ and $Nb^+$ substrate sputter cleaning on the formation of $Ti_{1-x}Al_xN$/steel interfaces generated in a combined cathodic arc/unbalanced magnetron deposition system. *Inst. Phys. Conf. Ser.* **161** (1999) 75-78

(II) C. Schönjahn, M. Bamford, L.A. Donohue, D.B. Lewis, S. Forder, and W.-D. Münz. The Interface between TiAlN hard coatings and steels substrates generated by high energetic $Cr^+$ bombardment. *Surf. & Coat. Technol.* **125** (2000) 66-70 (Young scientist best paper prize awarded by E-MRS)

(III) C. Schönjahn, L.A. Donohue, D.B. Lewis, W.-D. Münz, R.D. Twesten, and I. Petrov. Enhanced adhesion trough local epitaxy of transition-metal nitride coatings on ferritic steel promoted by metal ion etching in a combined cathodic arc/unbalanced magnetron deposition system. *J. Vac. Sci. Technol. A* **18**(4) (2000) 1718-1723

(IV) C. Schönjahn, D.B. Lewis, W.-D. Münz, and I. Petrov. Substrate Ion Etching in a Combined Steered Cathodic Arc-UBM Deposition System: Effects on Interface Architecture, Adhesion and Tool Performance. *Surf. Eng.* **16**(2) (2000) 176-180

(V) C. Schönjahn, A.P. Ehiasarian, D.B. Lewis, R. New, W.-D. Münz, R.D. Twesten, and I. Petrov. Optimization of In-Situ Substrate Surface Treatment in a Cathodic Arc Plasma: A Study by TEM and Plasma Diagnostics. *J. Vac. Sci. Technol. A*, July/August 2001

(VI) C. Schönjahn, H. Paritong, W.-D. Münz, R.D. Twesten and I. Petrov. Influence of the Interface Composition on the Corrosion Behavior of Unbalanced Magnetron Grown Niobium Coatings on Steel. *Submitted for publication in J. Vac. Sci. Technol. A*

(VII) W. D. Münz, I. J. Smith, C. Schönjahn, A. P. Deeming, and S. Clapham. PVD Superlattice Structured Hard Coatings Designed for Dry High-Speed Machining. Conference Proceedings, Nantes, June 2000.

(VIII) W.-D.Münz, C. Schönjahn, H. Paritong, and I.J. Smith. Source combinee, arc cathodique et magnetron desequilibre pour le depot de couche minees (Arc Bond Sputtering : ABS). *Le Vide* **205** (2000) 297-314

(IX) W.-D. Münz, D.B. Lewis, P.Eh. Hovsepian, C. Schönjahn, and I.J. Smith. Superlattice structured hard PVD coatings. *Surface Engineering* **17**(1) (2001)

(X) H. Paritong, C. Schönjahn, L.A. Donohue, and W.-D. Münz. PVD Interface Design by Cathodic Arc Generated High Energy Ion Bombardment. Accepted for publication in proceedings EUROMAT, Munich, September 1999.

(XI) H. Paritong, C. Schönjahn, and W.-D. Münz. Einfluss der Teilchenenergie von Nb-Ionen beim Ätzen von Substraten auf das Korrosionsverhalten nach der Beschichtung, Patent Pending, DPA 100 22 274.9

(XII) A.P. Ehiasarian, K. Macák, C. Schönjahn, R. New, and W.-D. Münz. Influence of the Ion Flux Density on the Efficiency of the Metal Ion Etching Process in Cathodic Arc Discharges. Accepted for publication in proceedings EUROMAT, Munich September 2000.

(XIII) P. Hovsepian, D.B. Lewis, C. Schönjahn, W.-D. Münz, S. Lyon, and K. Fletcher. Hard PVD Multilayer Coatings consisting of niobium and chromium protected mild steel against corrosion and wear. To be submitted for Proceedings of the International Conference on Metallurgical Coatings and Thin Films. San Diego April/May, 2001

# Acknowledgement

Many people to whom I wish to express my gratitude contributed to the present work. First I would like to thank my director of studies *Professor W.-D. Miinz* who gave me the chance to carry out this research project, for his supervision involving some heavy but finally always fruitful discussions and encouraging and helping me to gain international experience. I am also very grateful to my supervisor *Dr D.B. Lewis* who always had an open ear for all sorts of problems, for motivating me when I needed it most and all his valuable ideas and advice. My gratitude yields *Professor J.M. Rodenburg* for the same reasons but in addition for teaching me TEM and English and making lunch very enjoyable by a refreshing humour. The latter is also true for *P. Slingsby*, *T. Hudson* and *Dr M.C. Simmonds*. I also like to thank all other MRI staff in particular *S. Porter, P. Allender* and *C. Shaw* for all technical support and friendly chats. The same applies to all *members of the Surface Engineering Group* and *Bodycote SHU Coatings Ltd. staff.* Specifically I like to thank *R. Day, G. Robinson* and *C. Sellars* for always giving me a hand and teaching me English heritage, English language and South Yorkshire, respectively. I also thank *Dr I. Smith* for all the lifts he gave me but more importantly for always being there when nobody else was and there was trouble with the ABS machine. For helping me at the machine my thanks goes to *Dr P. Hovsepian, Dr K. Macak* and *A. P. Ehiasarian.* Besides machine time I also shared many pub and party hours with *A.P. Ehiasarian, H. Paritong* and many other fellow students whom I like to thank for all that happy hours. Special thanks go to *M. Lembke* and *A. Crecelius* who helped me a lot sharing my problems and providing me accommodation.

There are many people outside Sheffield Hallarn University to whom I indebted, first of all to *Professor I. Petrov* for giving me the chance to carry out research at the University of Illinois and his hospitality. I thank *Dr R. Twesten* for teaching me American English and his endless patience dealing with an infinite number of magnetic specimens in the STEM.

I also like to thank all members of *Professor J.E. Greene's Thin Film Group* for their hospitality and very warm welcome. In particular I like to thank *V. Petrova and S. Kodambak* who made me feel so comfortable in Illinois that I always found it hard to leave.

I like to thank *Dr T. English* and his *Surface Analysis Group at Corus* for teaching me English, British Humour and a little bit AFM and surface analysis.

Many thanks to *Dr H. Kheyrandish* and *Dr S. Romani* from MATS UK for inviting me to their Lab, teaching me some SIMS and SNMS and our discussions.

Last but not least I want to thank my parents and sister for their support and Bernd for so many things that it is impossible to list them.

# Contents

# Chapter 1

# Introduction

Within the last decades a fast development in a range of physical vapour deposition (PVD) techniques for modifying the surface of engineering components has taken place. This led to a new field of surface engineering - the design of a composite system (coating plus substrate) that produces a performance which cannot be achieved by either the coating or substrate materials [1].

One application for these composite systems is the wear and oxidation protection of cutting tools, in particular under very harsh conditions like dry high speed machining.

Often it is pointed out that the coating/substrate interface plays a major role for the functionality of coated systems [2], [3]. In particular high shear loads in the interface caused by high adhesive forces produced during dry machining demand a special high interface strength of the coated tools. To overcome the limitations in life time or an abated functionality of coated systems caused by interfacial failure (adhesive failure) a deeper understanding of the interface properties is indispensable. A brief introduction regarding interfaces and interface strength is given in Section 2.2.2 and it shows that the characterisation of the interface with respect to its chemical composition and morphology is required. However, detailed interface studies in conjunction with investigation of the functionality of the coated system other than in semiconductor applications are rare. The interface as the transition from the substrate to the coating can have sub-nanometre dimensions or can be in the range of a few nanometres for graded interfaces. This means that interface analysis is a challenge for most analytical techniques. Therefore the first aim of the work presented here was to establish a procedure, which is suitable for the characterisation of the TiAlN/ steel interfaces with respect to their chemical composition and microstructure.

To engineer interface properties successfully, which was the main objective of this project, the influence of process variables for coating deposition has to be known. Various PVD processes have different limitations. Therefore a brief review about selected PVD techniques is given in Section 2.1. Special attention is paid to the ABS (Arc Bond Sputtering) technique, which combines two PVD techniques in one coating unit, namely unbalanced magnetron sputtering (UBM) and cathodic arc (CA) evaporation. Main driving force for this development was the superior adhesion usually observed for arc deposited coatings in comparison to the much smoother sputter deposited films. The main emphasis of this project was to explore and optimise the potential of a cathodic arc source for interface engineering. An industrial sized ABS coating unit (Hauzer 1000-4) was used for all experiments to ensure a direct transfer of the experimental results of this study to commercial applications.

The standard PVD process consists of ex-situ pre-cleaning of substrates, loading to the vacuum chamber and pump down, substrate heating, in-situ substrate cleaning, interface formation, film deposition and substrate cooling and unloading [3]. In-situ substrate cleaning is the key step for interface formation because it may alter the original substrate surface considerably as discussed in detail in Chapter 4. Likewise, the interface strength depends on the microstructure of the coating as described in Section 2.2.3. Therefore a brief overview about microstructure evolution is given in Section 2.3.

Parameters, which determine the coating microstructure in the interface region can be divided into two groups. Substrate surface related parameters e.g crystallography and surface energy of the substrate and deposition related parameters. In this study the latter set of parameters was kept constant while the substrate surface was intentionally altered by various in-situ substrate cleaning procedures. The use of a cathodic arc ion source for substrate cleaning enabled us to investigate the substrate surface modification produced by bombardment with various metal ions including chromium, vanadium, niobium and titanium ions. For comparisons ion bombardment with inert gas ions, here Ar ions, extracted from a glow discharge was also performed. The latter method is commonly used prior to sputter deposition because of the availability of these ions in sputter coating units. However, it is well known that coatings deposited by arc evaporation, where metal ion bombardment is usually employed for in-situ substrate sputter cleaning, exhibit better adhesion of the coating to the substrate. The disadvantage of this PVD method is the coating roughness, which is caused by growth defects resulting from droplets. Those are emitted from an arc source, when the cathode spot moves across the target and no filter is used. Previous investigations ([4], [5]) have shown that Cr with its medium atomic mass, high melting point and extremely high vapour pressure is well suited for metal ion etching employing a steered cathodic arc as ion source because of small droplet sizes. Therefore, special attention was paid in this investigation to Cr ion bombardment for substrate sputter cleaning. In addition to the choice of the metal ion, process parameters such as ion energy, exposure time and working gas pressure (Ar is required to stabilise the arc discharge) were investigated with respect to cleaning efficiency and interface integrity in Chapter 4. It was also shown in this work how these parameters affect the microstructure of a subsequently grown TiAlN coating (Chapter 5). The impact of the interface properties and the microstructure of TiAlN on the adhesion was studied in Chapter 6. Furthermore, a correlation between performance in practical adhesion testing (scratch test) and life time in dry high speed milling of hardened A2 steel (58HRC) was established.

# Chapter 2

# Literature review

## 2.1 Selected PVD techniques for transition metal nitride deposition

### 2.1.1 Basics

The PVD (physical vapour deposition) method is the deposition of coatings by condensation of vapour in vacuum. The deposition process consists of three main steps, which are independent of the particular deposition technique [6]. These are

(I) vaporisation of the material to be deposited,

(II) transport of this material towards the substrate,

(III) film growth [3].

**Vaporisation**

The material to be deposited can be vaporised by evaporation or sputtering. Sputtering involves the ejection of atoms from a surface by momentum transfer from bombarding energetic atomic-sized particles [7]. Evaporation is a process of thermal vaporising of the target in which heating is carried out at a low pressure [8].

### Transport

During the transport the vapour atoms can collide elastically or inelastically with gas atoms. Elastic scattering influences mainly the distribution of the vapour in the deposition chamber and therefore film-thickness uniformity. Inelastic collision processes, such as ionisation, determine the flux of activated species (e.g. ions). Because of the significant effect of gas presence one can classify the following processes:

(I) vacuum processes (line-of-sight movement of metallic particles),

(II) processes in an inert gas atmosphere (scattering of metallic particles),

(III) reactive processes (formation of compounds) [8].

### Film growth

Film growth on the substrate surface is influenced not only by the substrate material and temperature, but also by the fluxes and energies of all bombarding species. The following dominant parameters have to be considered [3]:

(I) the flux and energies of metallic particles,

(II) the flux and energies of reactive gas particles, and

(III) the flux and energies of ions (relevant for *ion plating*, see below).

The term ion plating is applied to atomistic film deposition processes in which the substrate is subjected to a flux of high energy ions sufficient to cause appreciable sputtering before and during film formation ([9],[10], and [11]) [1] , independent on the source of the ions. Particle bombardment effects include

(I) modifying the substrate surface (cleaning, defect formation),

---

[1] A more recent definition for ion plating is given in [12] as follows: Ion plating is a generic term for deposition processes (vacuum-based and plasma-based) where concurrent or periodic energetic heavy particle bombardment during deposition is used to modify the composition, morphology, microstructure, and properties of the deposited material. These energetic particles can arise from (i) the acceleration of charged particles, (ii) high-energy neutrals from reflection from bombarded surfaces, or (iii) charge exchange processes [13].

(II) momentum transfer processes in the surface region (sputtering, desorption, recoil implantation, defect formation),

(III) addition of heat to the surface region,

(IV) formation of secondary electrons that can affect reactions [13].

Various PVD techniques have been developed combining different vaporisation-, transport-, and film growths conditions. These techniques vary in their deposition rate, the possibility of alloy deposition, and differences in coating microstructure and adhesion. So called structure zone models were developed to correlate the microstructure of the coating and process parameters. The dependence of the microstructure of evaporated films on the substrate temperature is given by the structure zone model from Movchan and Demichishin [14]. It classifies the microstructure of metallic coatings as a function of homologous temperature $T/T_m$ (where $T$ stands for substrate temperature and $T_m$ for the melting point of the coating material) in three groups (zones). The microstructures reaches from porous columnar (zone1) at homologous temperatures $\leq 0.3$ to fully dense equiaxed grains for $T/T_m \geq 0.5$. The Movchan and Demichishin model was extended by Thornton by adding a second axis to account for the effect of argon working gas pressure in sputtering [15]. Messier [16] replaced the pressure axis with a substrate bias axis therefore, introducing the effect of ion energy. A third axis accounting for the thickness of the film was also introduced. In addition to thermal and ion bombardment induced mobility "chemically induced mobility" should be considered. The chemically induced mobility refers to a control over the vapour species involved, their adsorption-desorption characteristics, and thus the ad-atom bond strength. Therefore it would account for surface chemical interactions [16].

The two methods relevant for this work, magnetron sputter ion plating and cathodic arc ion plating, will be reviewed next.

### 2.1.2 Magnetron sputter ion plating

In a sputter process coating material is dislodged and ejected from the solid surface due to momentum transfer associated with surface bombardment by energetic particles (high energy ions or neutrals). A certain energy (20 to 40 eV) is required for sputtering to occur. Above this threshold energy the sputtering yield (i.e. number of emitted target atoms per incident particle) increases with increasing energy until it reaches a maximum in the energy range of 5 keV to 50 keV [17]. For a particle of a given energy and incidence angle the sputtering yield depends on the mass of the target atoms, the degree of crystalline order and crystal orientation of the target, and its surface binding energy. An advantage of the sputter technique is that the chemical composition of sputtered coatings is often the same as the composition of the target, even when the components differ considerably in their sputtering yield [6].

In glow discharge sputter deposition the source of coating material (the target) is bombarded by working gas ions. Some working gas atoms are ionised due to the collision with secondary electrons and then accelerated to the negatively biased target. When these highly energetic ions hit the target surface momentum transfer can initiate collision cascades, such that target atoms are ejected from the target surface. In addition, various other events can take place at the target surface and within the target. These include backscattering, photon generation, desorption of gas atoms from the target surface, local heating, implantation, compound formation, amorphisation, and the creation of point defects, as shown in Figure 2.1. Furthermore, secondary electrons can be emitted. Those are necessary for further ionisation of the working gas in order to sustain the glow discharge.

A special technique is the magnetron sputter technique, where the secondary electrons are confined in a closed ring near the target surface, in which they drift in the $\mathbf{e} \times \mathbf{b}$ direction [3]. The electric field $\mathbf{e}$ is created in the space charge shield between the plasma and the cathode, and the magnetic field $\mathbf{b}$ is provided by permanent- or electro-magnets behind the target. The plasma density is increased in the magnetically confined region, which leads to a decreased discharge impedance and therefore

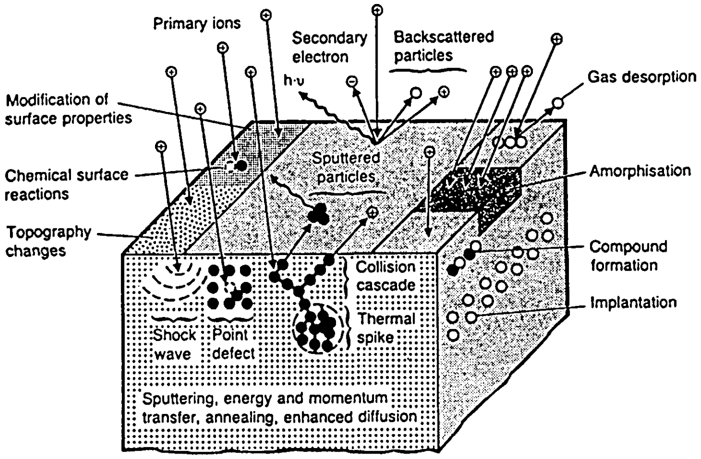

**Figure 2.1:** Possible ion-target interactions (from [18]).

to a higher current density. The latter one gives rise to an increase in deposition rate in comparison to a conventional diode sputtering arrangement [19].

In the conventional magnetron sputtering, the flux of high energetic particles towards the substrate is rather low. This is due to a very sharp decrease in ionisation with increasing distance from the target to the substrate surface [20]. A so called unbalanced magnetron (UBM) can be used to achieve an ion plating effect in magnetron sputtering. Here the magnetic field is modified by an additional magnetic field in such a way that a dense plasma is confined by the total magnetic field between the target and the substrate [21]. A multipolar magnetic plasma confinement (MMPC) can be achieved using a planar unbalanced magnetron, equipped with two magnetic coils, and a set of permanent magnets located on the internal surfaces of the deposition chamber ([22] and [23]). A similar effect can be obtained, when the magnetic fields of an even number of unbalanced magnetrons is arranged to to form a closed magnetic field. For plasma conditions achieved by a closed field configuration a special structure zone model has been published recently by Kelly and Arnell [15]. It describes the microstructure determined by the homologous temperature, the bias voltage, and the average energy carried by the arriving ions per condensing atom.

### 2.1.3 Cathodic arc (CA)-ion plating/CA-metal ion etching

The evaporated species are produced by striking one or more electric arcs on the surface of the material to be evaporated (cathode of the arc discharge). The evaporation is a consequence of high local cathode surface temperatures. The evaporated material is ionised by collisions with electrons and then accelerated away from the cathode due to the nonuniform potential distribution and plasma expansion [3]. The plasma is highly ionised up to 100% and contains macroparticles (also called droplets) in addition to electrons, ions, and atoms, as shown in Figure 2.2a.

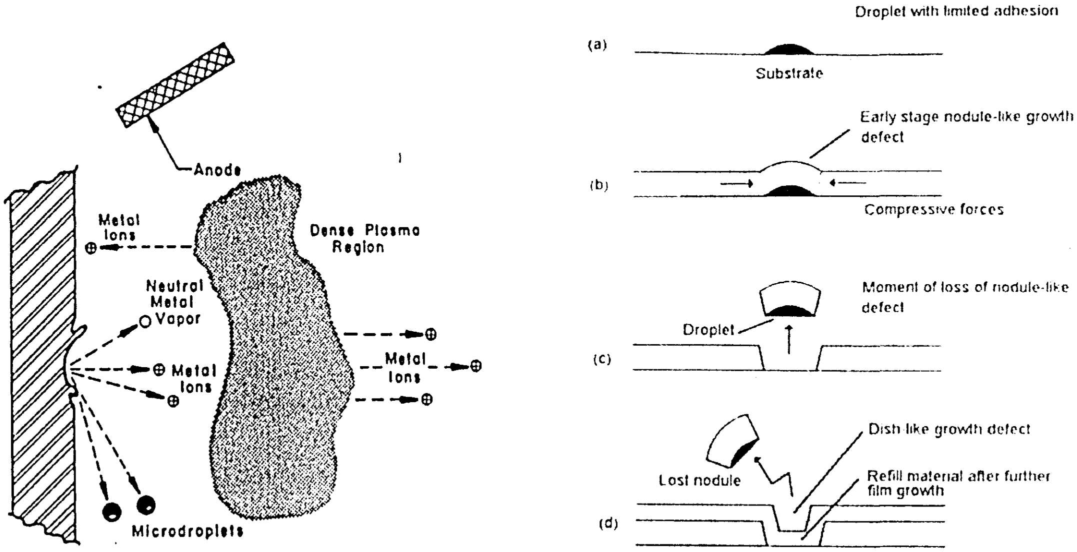

(*a*) (*b*)

**Figure 2.2:** Cathodic arc evaporation: (a) cathode spot region of a vacuum arc showing neutral, ion, and microdroplet emission (from [24]); (b) effect of weakly bound microdroplets on hole generation in the coating (from [25])

The macroparticles can cause growth defects and, when expelled, holes in the coating as shown in Figure 2.2b. Therefore one tries to minimise the number of macroparticles reaching the substrate surface. This can be achieved by steering the arc with a magnetic field [26], various filter designs [27], pulsed laser-arc deposition, where the arc discharge is ignited by short laser pulses [28], or the use of a low arc

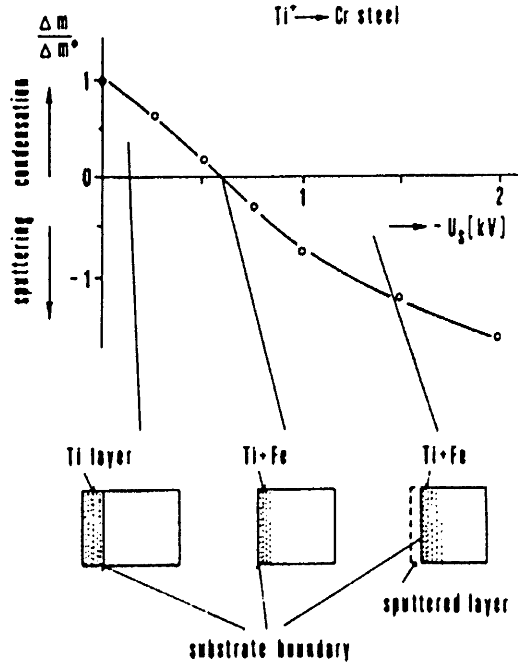

**Figure 2.3:** Effect of the substrate bias on substrate surface modification by metal ion bombardment . From [3].

current. At low arc currents (below 50 A) the main loss of cathode material occurs in the form of ions (greater 50%) [29].

When a highly negative substrate bias is applied during the arc evaporation metal ions are accelerated towards the substrate surface, which now becomes a target for positively charged ions. Consequently, besides the condensation process, other interactions may take place at the substrate surface, in analogy to ion target interactions described in Section 2.1.2. Which of those processes dominates is determined by the energy of the impinging particles in relation to the degree of ionisation (number of ions to total number of particles). This is shown in Figure 2.3. The energy of the ions is determined by the applied potential difference and the charge state of the ions. Ions of a wide energy range will be involved because, for example, Cr-ions generated by arc evaporation exist up to a triple charged state [30]. At low energies metal ions condense at the substrate surface. A metal deposition layer is formed. With increasing energy re-sputtering of these metal atoms becomes more pronounced. At even higher ion energy, in addition to the condensed metal atoms, substrate material is removed. In that case one often refers to substrate sputter

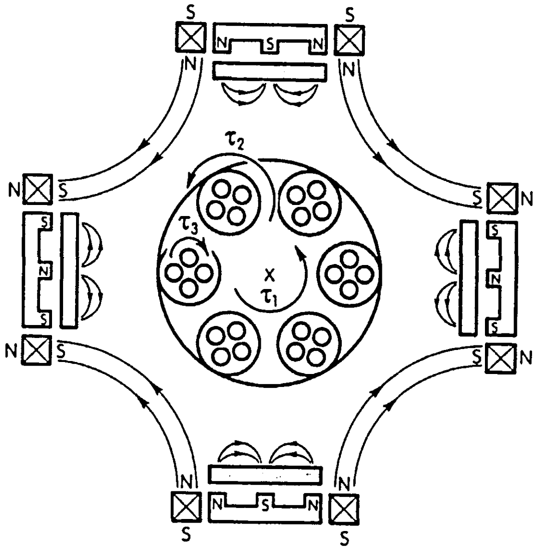

Figure 2.4: Schematic diagram of the combined UBM/CA four-target deposition system used in these experiments.

cleaning or metal ion etching.

### 2.1.4 The ABS (arc bond sputtering) technology

The ABS technology was developed in order to combine the advantages of the arc technology (i.e. good adhesion due to metal ion etching) with the versatility of material selection given by the application of magnetron sputtering for deposition of smooth coatings [31]. The ABS technology is realised in the *Hauzer Techno Coating Europe B.V. HTC 1000-4* combined CA/UBM system (see Figure 2.4) [31] by moving the permanent magnets in a manner shown in Figure 2.5. The typical deposition sequence consists of the following steps:

(I) pump down,

(II) heating and degassing,

(III) target sputter cleaning,

(IV) CA metal ion etching,

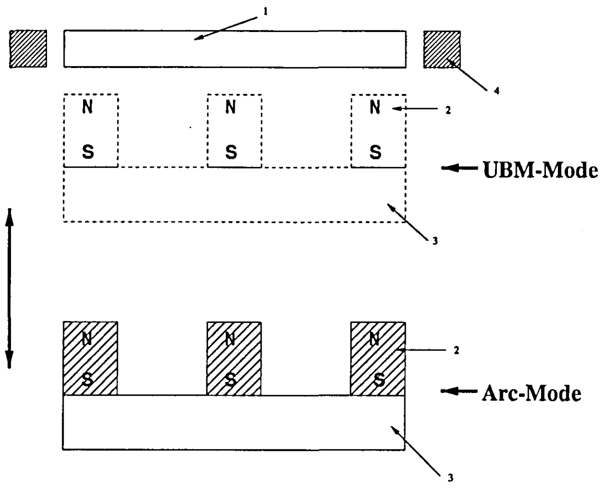

**Figure 2.5:** Cathode design for alterative arc and UBM modes: 1 - target; 2 - permanent magnets; 3 - magnetic yoke; 4 - magnetic coils.

(V) UBM film deposition,

(VI) cool down.

Of special interest here was CA metal ion etching prior to the deposition of TiAlN. Different cathode materials (metal ions) may be used. In order to generate a graded interface (see Section 2.2.2) the use of a TiAl cathode would seem to be appropriate. However, the low melting point of this material results in many large droplets [4]. An investigation of droplet number and size for different materials was carried out previously ([4], [5]). The maximum droplet diameter decreases rapidly with increasing melting point [2] . A higher vapour pressure may also result in a further decrease of droplet size since even solidified droplets may shrink due to sublimation during the flight or after arrival at the substrate surface ([4], [5]). Therefore, Cr seems to be well suited as target material, not only due to its high melting point but also because of its high vapour pressure.

In fact, a reduction of roughness (by reduced droplet size and number, hence, less pronounced and fewer growth defects) by using Cr instead of TiAl led to a doubling of the life time in dry drilling tests carried out in cast iron [32].

---

[2] Melting point of Cr: 1870°C; Melting point of TiAl: 1450°C.

## 2.2 Adhesion

### 2.2.1 Definitions

Fundamental adhesion refers to nature and strength of the binding forces between two materials in contact. It is defined as the summation of all interfacial intermolecular interactions between the contacting materials [33]. These binding forces can be classified as follows [34, 35]:

(I) primary valence type or chemical bonding (ionic, covalent or metallic),

(II) pseudo primary valence type (hydrogen bridge bonding),

(III) secondary valence type (Debye, Keesom and London dispersion forces - collectively known as Van der Waals forces).

The last two types of forces are classified in [35] as physical bonds. Chemical bonds reveal a relatively strong interaction energy between $110\frac{\text{kJ}}{\text{mol}}$ and $1000\frac{\text{kJ}}{\text{mol}}$ for metallic bonds and covalent or ionic bonds, respectively. The physical bond strength is rather weak with less than $50\frac{\text{kJ}}{\text{mol}}$. The forces of adhesion resulting from these energies vary from $500\frac{\text{N}}{\text{mm}^2}$ in the case of hydrogen bonding to $5000\frac{\text{N}}{\text{mm}^2}$ and more for chemical bonds [36].

Adhesion can also be expressed in thermodynamical terms. Thermodynamic adhesion signifies the change in free energy when an interface is formed, and is expressed as

$$W_A = \gamma_{S1} + \gamma_{S2} - \gamma_{S1S2}, \tag{2.1}$$

where $W_A$ is the work of adhesion [3] and $\gamma_{S1}$ and $\gamma_{S2}$ represent the surface free energies of material 1 (substrate) and material 2 (film), respectively. The interfacial free energy is written as $\gamma_{S1S2}$ [33]. This shows that the work of adhesion increases when the interfacial free energy decreases. It means that more work is required to separate strongly bounded low energy interfaces than weekly bound high energy

---

[3] More precisely, this is the reversible work of adhesion, which means that no energy dissipation, for example in form of plastic deformation, takes place.

ones [37]. The relation between interfacial free energy and work of adhesion for various ceramic-metal systems is shown in Figure 2.6.

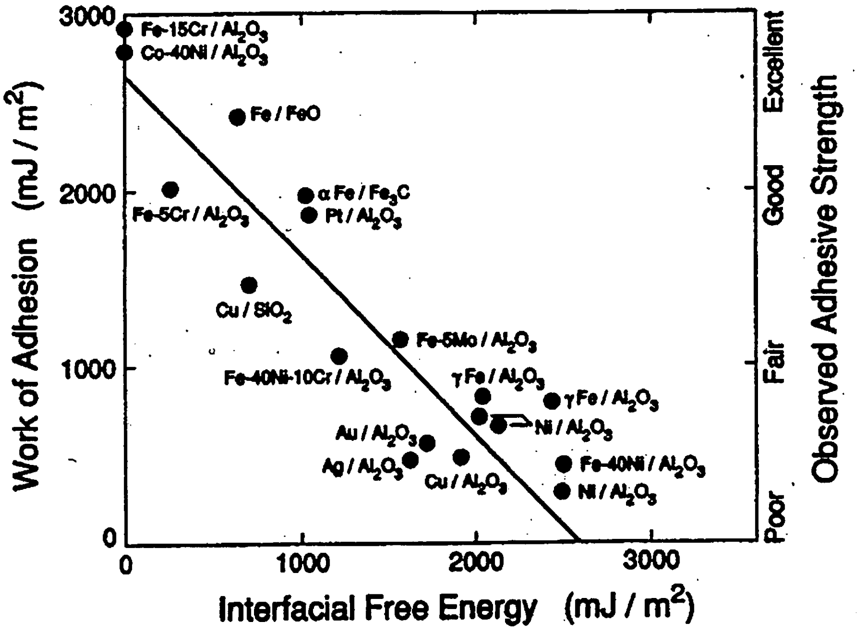

**Figure 2.6:** Inverse correlation between the thermodynamic work of adhesion and the interfacial energy for various ceramic-metal systems (from [37]).

To the authors knowledge currently there is no method available to measure the fundamental adhesion for ceramic hard coatings. What is measured instead is the practical adhesion, which signifies the force or the work required to remove or detach the coating from the substrate if the locus of the failure is interfacial or interphaseial. Practical adhesion is a function of fundamental adhesion together with other factors. These include coating thickness, internal stress of the coating, and mechanical properties of the coating and the substrate [33].

### 2.2.2 Interfaces

#### Overview

The transition region from the substrate material to the coating material is the interface region. It can be classified in abrupt-, mechanical-, diffusion-, compound-, pseudo-diffusion-, and reactively graded interfaces, or as a combination of them [38] (see Figure 2.7).

Weiss [35] prefers a different classification that distinguishes between a monolayer by monolayer interface, a diffusion interface, an intermediate phase interface, a physical bond interface, and an interlocking interface.

The type and extent of the interface region depends on the deposition process, and it influences the adhesion of the coating to the underlying substrate. A certain depth of the interface region may result in an increase of the adhesion as well as a graded interface. In the latter case the stress level can be reduced by avoiding abrupt changes in interplanar spacing. A particular interfacial composition may be beneficial in order to guarantee a better compatibility between substrate and coating material [39].

#### Mechanical aspects

An interface on a rough surface where the rough surface is filled to give rise to mechanical interlocking is called a mechanical interlocking interface. The interlocking sites can vary from mechanically machined dove-tails, grooves to micro-roughness produced by grit blasting [35]. There are three different mechanisms of mechanical interlocking involved. These are an increased surface area, friction locking, and dovetail locking [35] (see Figure 2.8).

#### Elemental Distribution Consideration

- *Abrupt interface or physical bonding interface:* These types of interfaces are both characterised by an abrupt change from the substrate material to coating material in a distance of the order of the atomic spacing. In other words, the

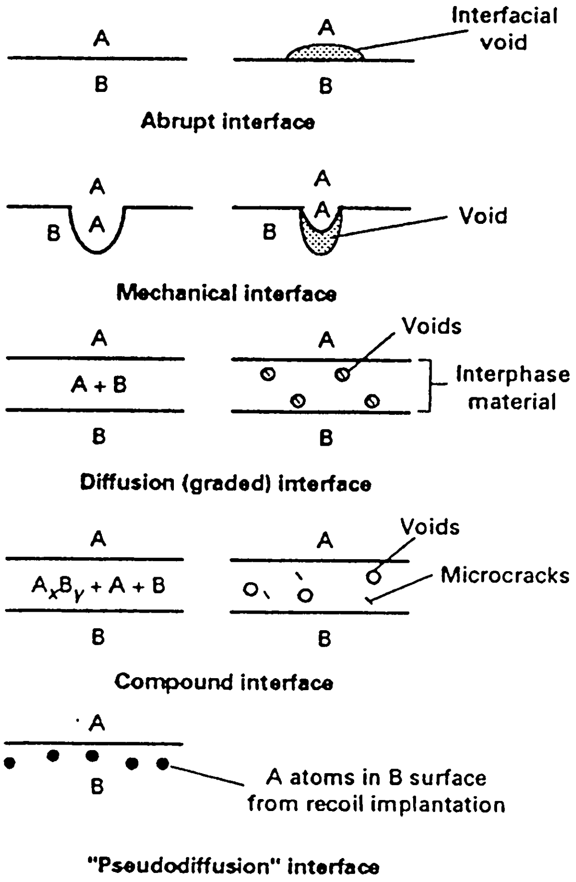

**Figure 2.7:** Schematic drawing of different types of interfacial regions (from [38]).

interface is considered to be a two-dimensional plane. The abrupt interface defined in [38] is formed when only weak chemical reactions are involved and if no bulk diffusion is observed. Quasi-interaction free interfaces are formed if both the coating and the substrate material bonding are of the covalent type [40].

- *Diffusion, pseudo-diffusion and intermediate phase interfaces:* All these interfaces are characterised by a gradual change in chemical composition. This can be either caused by diffusion, by "grading" the deposition material from one material to the other, or by recoil implantation during concurrent or subsequent ion bombardment (pseudo-diffusion interface). If separate phases are formed in the zone of diffusion or pseudo-diffusion an intermediate phase in-

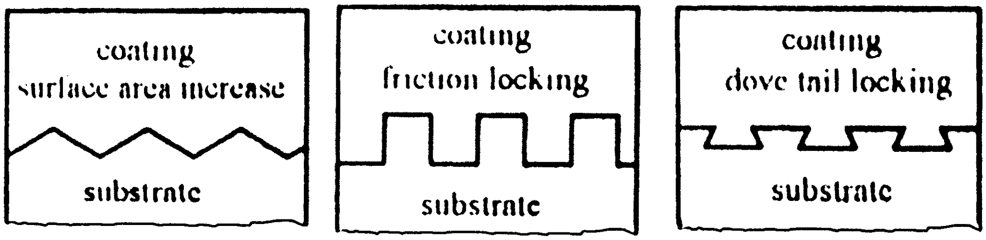

Figure 2.8: Different types of mechanical interlocking (from [35]).

terface is created. This type can be expected for interfaces between metallic and ionic hard materials [40]. These interfaces are most likely to be formed by ion assisted deposition.

- *Compound, reactively graded interfaces:* The compound interface requires diffusion along with chemical reaction to form a compound interfacial region. The compound containing interface can also be formed by controlling the availability of reactive gases during the reactive deposition. These interfaces are most likely to be formed by ion assisted deposition and nitriding.

### Structural matching

The interface might be crystalline/amorphous or crystalline/crystalline (single- or polycrystalline). If both materials in contact are crystalline they can either have a different (for example b.c.c/f.c.c interface) or similar *bravais lattice* (f.c.c/f.c.c). In the latter case, despite differing lattice parameters for heterophase interfaces, the two layers of neighbouring phases might fit together by generating misfit dislocations (semi-coherent interface) or introducing stress in the coating material (coherent interface). This type of interface is characterised by almost perfect chemical bonding. Metallic hard materials are able to form such coherent or semi-coherent interfaces with metals [40]. Coherent and semi-coherent interfaces are observed when the film growth is epitaxial. It is possible to find semi-coherent interfaces or coherent interfaces even when materials with different bravais lattice are in contact, eg. b.c.c/f.c.c. This is of special interest for this work and therefore further elucidated in Section 2.3.2.

### 2.2.3 Dependence of adhesion on the interface type

#### Mechanical aspects

An increased substrate surface roughness may result in mechanical interlocking, where fracture along this interface requires changing stress tensors. Thus, the practical adhesion can be high [38]. An example of mechanical interlocking are diamond-metal composite coated cemented carbide tools [41], where "anchoring roots" are formed on the interface. It is also reported that the increased adhesion of $SiO_2$ films, deposited by radio-frequency (RF) sputtering onto stainless steel substrates, is due to the formation of microvoids in the interface layer. This allows mechanical interlocking between the coating and the substrate. The microvoids were induced by extended ion bombardment [42].

If the cavities resulting from surface roughness cannot be filled the adhesion will be lower due to a lack of contact and interfacial voids. For example, Koski [43] stated that with decreased substrate roughness ($Ra = 116nm, 77nm, 27nm$) the adhesion was improved (measured with cantilever and 3 point bending test) for a DC planar magnetron deposited coating. Liu *et al.* [44] found the same tendency on ion plated CrN coatings. According to Carvalho *et al.* [45] a smoother surface leads to a longer fatigue life for low contact stress. At higher contact stress the surface roughness seems to have only very little influence.

#### Elemental distribution consideration

Improved practical adhesion (scratch test) was found when a Ti interlayer was deposited on AISI D2 steel prior to TiN deposition using a hollow cathode discharge (HCD) ion plating technique [46]. Here it was reported that depth profiles by secondary ion mass spectrometry (SIMS) indicate that the adhesive strength of the coating/substrate interface increased with increasing interdiffusion depth. Diffusion is not always beneficial for a high adhesive strength, as in case of carbon nitride thin films. Poor adhesion on tool steel was found owing to diffusion of nitrogen or carbon atoms into the substrate at the deposition temperature of $T \geq 325$ ℃ [47]. It is also reported by Helmersson *et al.* [48] that a Ti interfacial layer deposited above 400 °C reduces the adhesion of a TiN coating on HSS (high-speed steel), whereas below this temperature it has a beneficial influence on the adhesion. The reduced adhesion at higher temperature is explained to be the result of TiC formation.

A detrimental effect of compound formation on the adhesion is frequently reported for the so called duplex treatment ([49],[50]), which comprises plasma nitriding of the substrate prior to hard coating deposition when the nitride-layer includes a compound zone ($\epsilon - Fe_{2-3}N$ and $\gamma^{|} - Fe_4N$) [51]. Nitriding of the substrate is performed to increase the load bearing capabilities in order to support a tribological coating under applied stresses [49], to reduce oxidation [52], and for being beneficial for the adhesion of hard coatings ([53],[54],[55],[56] and [57]). The latter is only the case when no compound layer, resulting from the nitriding process, is formed [58]. A reduced practical adhesion of the hard coating on a compound containing surface is explained by the brittleness of the compound layer, compared to a non-nitrided substrate surface. D'Haen also [59] reports bad adhesion of Ti-TiN coatings deposited on plasma nitrided AISI 304 steels caused by the formation of CrN precipitates. The explanation for the bad adhesion is, according to D'Haen, the brittleness, which is a result of CrN formation.

As mentioned above Ti is used as a bond layer for TiN coatings, so too is Cr. A Cr bond layer is followed by a graded CrN interlayer, which is gradually changing to a Cr-Ti-N layer before the actual coating - the Cr-Ti-N layer - is deposited. This results in an improved adhesion when compared with the adhesion of CrN or Cr-Ti-N deposited directly onto the steel substrate [60].

The formation of CrN during a low pressure plasma treatment of AISI 440 C and AISI 316 L was observed by Göning *et al.* [61] using X-Ray photoelectron spectroscopy (XPS) investigation. But in contrast to D'Haen [59], the authors expect an improved adhesion of a TiN coating because TiN and CrN are isostructural and have similar lattice parameters (see Table 2.1).

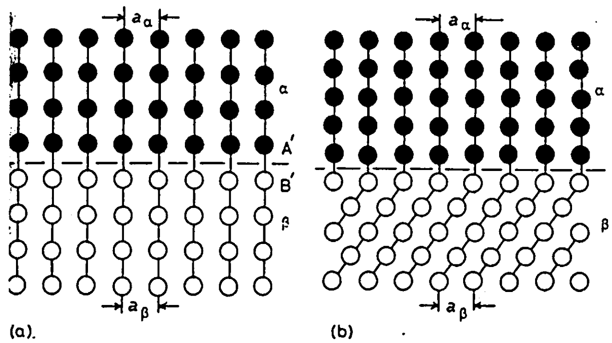

**Figure 2.9:** Coherent interfaces with no mismatch (strain free interfaces): (*a*) different chemical composition, same crystal structure; (*b*) different composition and crystal structure (from [62], page 143).

### Structural matching

The work of adhesion or interface strength, as given by equation 2.1 in Section 2.2.1, depends not only on the free energies of the materials in contact but also on the interfacial energy $\gamma_{S1S2}$. There are two factors which can contribute to the interfacial energy; a compositional $\gamma^c$ and a structural component $\gamma^s$ as expressed by equation 2.2.

$$\gamma_{S1S2} = \gamma^c_{S1S2} + \gamma^s_{S1S2}. \tag{2.2}$$

If there is no mismatch between the two materials as shown in Figure 2.9 (for example two phases $\alpha$ and $\beta$ which differ only in their composition) the only contribution to the interfacial energy is the compositional component [4] .

Therefore, in that case the interfacial free energy is low. Typical values for coherent interfaces are $\gamma_{S1S2} \leq 200\frac{\mathrm{mJ}}{\mathrm{m}^2}$ [62]. In semi-coherent lattices the mismatch can be accommodated by elastic strain in the film or in form of misfit dislocations as shown in Figure 2.10 *a* and *b*, respectively.

An expression for the misfit dislocation energy $\gamma^M_{S1S2}$ was formulated by van der Merwe [65] and is presented in equation 2.3

$$\gamma^M_{S1S2} = \frac{\mu(a_1 + a_2)}{8\pi^2}(1 + \Lambda - \sqrt{1+\Lambda^2} - \Lambda \ln 2\Lambda\sqrt{1+\Lambda^2} - 2\Lambda^2), \tag{2.3}$$

---

[4] $\gamma^c_{S1S2}$ can be estimated using the model given by Becker [63] for alloys with large positive enthalpy of mixing or otherwise the Cahn-Hillard model [64].

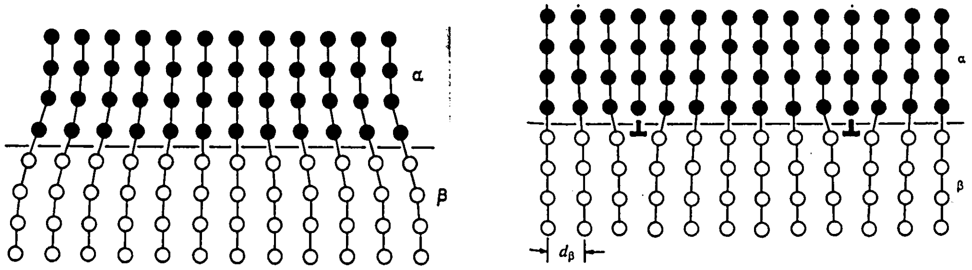

(a) (b)

**Figure 2.10:** Interfaces with small lattice mismatch: (*a*) with coherency strains; (*b*) with misfit accommodation via a series of edge dislocations (from [62], page 144 and 145).

where

$$\Lambda = 2\pi\delta\frac{C_8}{\mu} \tag{2.4}$$

$$C_8 = \frac{1}{\frac{1-\nu_1}{\mu_1} + \frac{1-\nu_2}{\mu_2}}. \tag{2.5}$$

$\mu$ is the interfacial shear modulus, and $\mu_1$ and $\mu_1$ are the shear moduli of phase 1 and phase 2, respectively. Accordingly, $\nu_1$ and $\nu_2$ are the Poisson ratios for these phases, and $a_1$ and $a_2$ are the lattice parameters and $\delta$ is the misfit. For small differences in the lattice parameters $\delta$ is given by equation 2.6

$$\delta \cong \frac{a_1 - a_2}{a_1} \tag{2.6}$$

. The $C_8$ term in equation 2.2.3 is an effective elastic constant that accounts for elastic interactions within each crystal, whereas $\mu$ accounts for such interactions across the interface. For a small misfit it can be energetically favourable to strain the film. The elastic strain energy $E_{el}$ can be calculated using equation 2.7 [37]

$$E_{el} = \frac{\mu_1(1-\nu_1)L\delta^2}{1-2\nu_1}. \tag{2.7}$$

$L$ is the thickness of the film (phase 1).

As long as the elastic strain energy is smaller than the misfit dislocation energy the film can form a fully coherent interface. However, with increasing film thickness

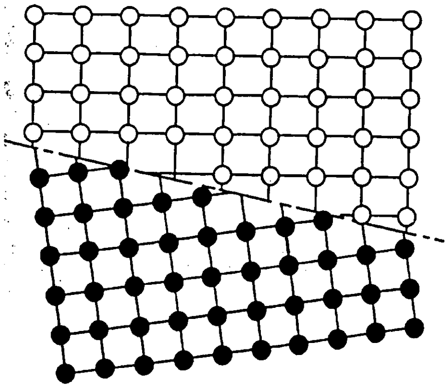

**Figure 2.11:** Incoherent interface as it occurs for very different patterns of matching atoms or similar patterns but intertatomic distances $\geq$ 25% (from [62], page 147).

the strain energy increases. When it reaches the value of the misfit dislocation energy dislocations are formed. That critical thickness depends not only on the misfit but also on the elastic constants of the film. Elastic strain energy or misfit dislocation increase the interfacial energy according to equation 2.2. Typical values of the interfacial energy are given in [62] to be in the range of $200\frac{\text{mJ}}{\text{m}^2} \leq \gamma_{S1S2} \leq 500\frac{\text{mJ}}{\text{m}^2}$. According to Howe [37] the upper limit is $800\frac{\text{mJ}}{\text{m}^2}$. Howe [37] gives a comparison of the structural and the compositional components of the interfacial energy for two f.c.c crystals with different lattice parameters as a function of temperature for two different misfits of 0.2% and 2%. It is shown that the compositional contribution $\gamma^c$ dominates for the smaller misfit but at the large misfit the structural contribution $\gamma^s$ can be more than twice the value for $\gamma^c$. The structural contribution depends much less on temperature compared to the compositional contribution, which drops sharply at increased temperatures. Hence, at high temperatures the structural component becomes more dominant.

In incoherent interfaces the misfit is evenly spread out along the entire interface, as shown in Figure 2.11. For such interfaces the interfacial energy is said to be in the range of $800\frac{\text{mJ}}{\text{m}^2} \leq \gamma_{S1S1} \leq 2500\frac{\text{mJ}}{\text{m}^2}$ [37] or between $500\frac{\text{mJ}}{\text{m}^2} \leq \gamma_{S1S1} \leq 1000\frac{\text{mJ}}{\text{m}^2}$ according to [62]. This shows that structural matching, as it is the case in epitaxial grown coatings, can, from the thermodynamical point of view, lead to an increased adhesion compared to incoherent interfaces.

The effect of structural matching on practical adhesion of transition metal nitrides on steel or carbides will be reviewed next. However, only few data are available because epitaxial growth can only occur under certain conditions (substrate and deposition related), as described in more detail in Section 2.3.2. For example, Helmersson *et al.* [48] found an increased practical adhesion of TiN (scratch-test) when the HSS substrate surface was covered with a thin FeO (NaCl structure $a_{\mathrm{FeO}} = 0.431\mathrm{nm}$) layer instead of $Fe_2O_3$ or $Fe_3O_4$. They concluded that the increased adhesion could be a result of structural matching. On the other hand, in [66] poor adhesion (scratch-test) of a TiN coating deposited directly on to austenitic stainless steel without titanium underlayer was reported, in spite of the local epitaxial growth of TiN on the substrate (with a Ti interlayer epitaxial growth has not been observed). However, in [67] it has been suggested that this could be due to the stable native $Cr_2O_3$ of the substrate (therefore less stable CrN, which provides chemical bonding, is not formed). The same problem occurs in case of TiN directly deposited to HSS [67] as substrate. But the adhesion is better when compared to TiN on stainless steel. In case of stainless steel AISI-304 the misfit is larger (see Table 2.1) and epitaxial growth is apparently insufficient to compensate for the poorer chemical bonding of nitrogen to the substrate. Therefore, it seems that epitaxial growth is of advantage for practical adhesion in general. However, epitaxial growth process conditions may imply other parameters that result in a lower practical adhesion value due to changes in the compositional component of the interfacial free energy.

### 2.2.4 Adhesion measurement methods for hard coatings

#### Introduction

Even though there is no test method available to measure the fundamental adhesion directly a large number of methods exists which give information about the practical adhesion. Some more frequently cited techniques which can be used to asses practical adhesion of hard coatings on steel substrates are

- scratch test ([68, 69, 2, 70, 71]),
- indentation test ([72, 71, 73, 74]),
- laser spallation ([71, 75, 76]),
- surface acoustic wave methods ([77, 78]), and
- fatigue methods ([45, 79]).

Several review papers are available about the subject ([80], [81],[82]).

Here, only the Scratch test will be considered in more detail, as it is the most commonly used test. Besides the *Rockwell indentation test* [83], which provides qualitative information [5] , it is the only test available for this project.

### Scratch-test

The Scratch-test is a widespread method to judge practical adhesion. In the Scratch test a Rockwell C diamond is drawn over the sample surface under a stepwise or continuously increasing normal force. The resulting damage can be observed either employing an optical microscope, measuring the frictional force or by using the acoustic emission correlated to the appearance of certain failure modes (fairly good correlation is only given in the case of thin coatings on soft substrates [71]). A critical load value is defined, but there is more than one definition of this value. For example, the critical load is often referred to the load at which the coating is removed in a regular way along the whole channel length. There are approaches to relate the work of adhesion to the critical load but the applied models are not universal applicable. This is not only because of the complex stress field generated by the moving stylus but also due to a number of extrinsic parameters, like residual stress in the coating or the coating thickness. If, for example, the coating is under compressive stress the critical load is decreased because the effective stress is the summation of

---

[5] In the Rockwell indentation test the area of delaminated coating area and crack propagation caused by a Rockwell C indentation are observed. Assessing scratch test values the Rockwell indentation test should also be considered because it yields complementary information due to different stress fields.

the residual compressive stress and the stress generated by the moving indenter. Adhesive failure (spalling or buckling) occurs when the elastic strain energy stored in the coating exceeds about twice the surface energy required for the generation of a crack within the interface between coating and substrate. This means, the load at which adhesive failure is observed is determined by the ratio between elastic strain and surface energy. This ratio, and therefore the critical load, depends on the coating thickness [84].

## 2.3 Film growth and microstructure evolution

### 2.3.1 Structure evolution of polycrystalline films

Work about this subject is often limited to certain deposition techniques and material classes. This Section summarises general aspects involved in microstructure evolution independent of the detailed deposition parameters. This Section is mainly based on a recent review paper by Thompson [85].

The following key process are involved in the microstructure evolution:

(I) nucleation of isolated crystals,

(II) growth of nuclei,

(III) impingement, grain boundary formation, and

(IV) thickening.

The first three steps determine the initial grain structure. The last process can lead to further grain structure evolution in two fundamentally different ways, depending on the mobility of the grain boundaries. In case of immobile boundaries the grain structure developed during the first three steps is retained. Thickening occurs usually via epitaxial growth and development of columnar grains and competitive growth. On the other hand, when the grain boundaries are mobile grain structure evolution continues within the coating during thickening so that the grain size scales with the film thickness.

### Nucleation

The nucleation rate $I$ is given by

$$I = I_o R^n e^{\frac{-\Delta G_n}{kT}}, \tag{2.8}$$

where $I_o$ is a temperature and deposition-flux-independent constant, R is the flux of atoms arriving at substrate surface, $k$ is Boltzman's constant and $T$ is the temperature of the substrate. $\Delta G_n$ is the energy of formation of a cluster of size $n$, where $n$ is the critical cluster size. For PVD processes n has a low integer value, often only one (so that the minimum stable cluster size is two). Because the degree of supersaturation decreases with increasing T, as T increases, n increases (eg. form one to three) and $\Delta G_n$ increases, so that the temperature dependence of the nucleation rate becomes stronger at higher temperatures. It is generally found that the nucleation rate decreases with increasing temperatures. It is important to note that selective nucleation can occur when specific nuclei orientations will minimise surface and interface energies.

### Growth of nuclei

Stable nuclei can grow to form islands. Again, the growth of islands with specific surface- and interface-energy minimising crystallographic orientations will be favoured.

### Impingement, grain boundary formation, and grain growth

Once islands impinge island coarsening can occur through exchange of atoms via grain boundary motion or via diffusion of atoms on the surfaces of the islands. When two islands of the same size have just grown to the point of contact, there is a driving force to eliminate the energy of the free surfaces in exchange for the lower energy of a newly formed grain boundary. This can happen without diffusive processes, through elastic distortion of the islands as they are brought together through grain boundary formation which initiates at the base of the islands, where they first make contact. This results in substantial strain if there is no sliding at the island/substrate interface.

Grain growth can occur in order to reduce grain boundary energy. Interface and surface energy affect the grain growth, which leads to texture development. Crystallographic orientations which minimise the sum of interface and surface energy are favoured. On amorphous substrates surface energy minimisation does not favour growth of grains with specific in-plane orientations. However, for polycrystalline films on single crystal substrates the interface energy depends on the in-plane orientation of the grain and grain growth is expected for films composed of grains with three-dimensionally constraint or epitaxial orientations. In addition grain growth can favour orientations which provide a strain minimisation. Grain growth can be suppressed by impurities (oxide formation), leading to smaller deposited grain sizes and immobile grain boundaries for materials which would have mobile grain boundaries, when deposited under clean conditions.

### Thickening

Once a continuous film has formed through nucleation, growth and coalescence thickening is normally expected to occur via epitaxial growth on preexisting grains, even at quite low temperatures. However, re-nucleation due to impurities can occur preventing epitaxial growth. This was demonstrated by the incorporation of small amounts of Yttrium in $Ti_{0.43}Al_{0.52}Cr_{0.03}Y_{0.02}N$ films, which leads to a fine grained near equiaxed microstructure in contrast to the conventional columnar $Ti_{0.44}Al_{0.53}Cr_{0.03}N$ coating morphology ([86] and [87]). A similar observation was described for Yttrium incorporation in TiN films [88] and was explained as follows. Yttrium atoms have a low surface mobility and a strong bonding tendency with oxygen. So Yttrium atoms promote heterogeneous nucleation by forming fine oxide particles at the substrate surface.

For very low self diffusities of ad-atoms, kinetic roughening can occur. Under conditions of severely limited ad-atom mobility roughness at the surface of even thickening amorphous films can become accentuated, which can result in columnar

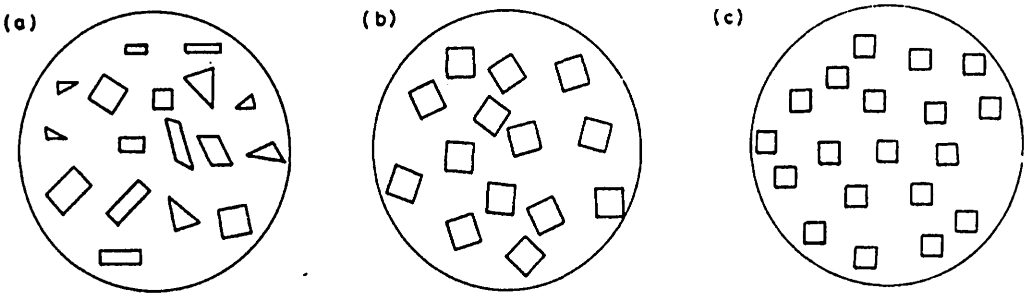

**Figure 2.12:** Different possibilities of orientational relations between host and guest crystals: (a) fully non-oriented, (b) texture, (c) epitaxy (from [89]).

growth. When ad-atoms arrive at normal incidence to the film surface, perturbations are stabilised and columnar structures develop. Here the columns meet at regions of low density relative to the density in the interiors of the columns.

### 2.3.2 Epitaxy

Epitaxy is a nucleation and growth relationship between two crystalline phases, where a crystalline phase "g" grows in a structural dependent manner onto a given phase of a given structure "h" of the host crystal [89]. There are three different possibilities of orientational relationship between host and guest crystal (see Figure 2.12):

(I) completely random orientation (fully non oriented),

(II) guest crystallites all grow with the same low index stable lattice planes on the substrate surface (texture),

(III) guest crystallites and the crystallites of the substrate show both the textural and azimuthal orientation towards one another (epitaxy).

It follows that epitaxial growth can only occur if for special crystal faces (hkl) the free interfacial energy (host-guest) as a function of the azimuthal orientation shows marked minima (as a result of the atomic structure of the host surface) [90].

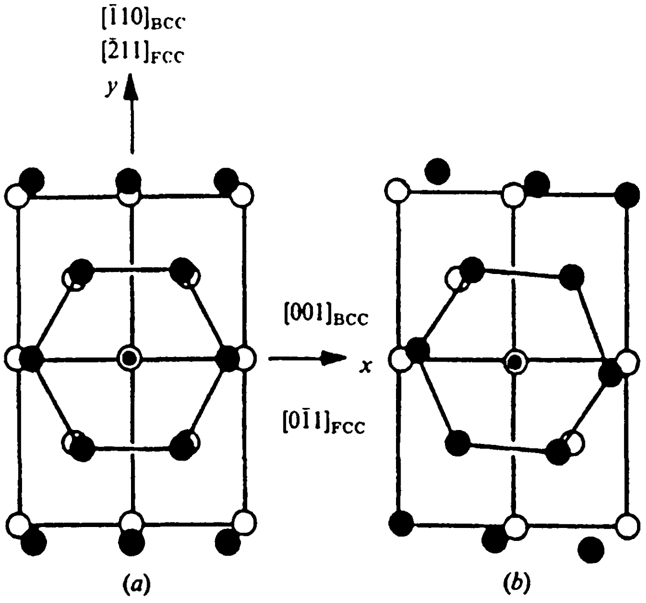

**Figure 2.13:** Overlay of an f.c.c(111) monolayer (filled circles) onto a b.c.c (110) substrate surface (open circles): (a) f.c.c $[0\bar{1}1]$ parallel to b.c.c [001]; (b) 5.26$^o$

For example in the case of an f.c.c. (111) monolayer (nearest neighbour distance $a$) on top of the close packed (110) surface of a b.c.c substrate (nearest neighbour distance $b$) for a particular value of $a/b = 1.0887$ one can achieve matching along the most closed packed row of these lattices by rotating the overlayer through 5.26 degree (see Figure 2.13b). That means that many overlayer atoms sit (on average) in the minima of the substrate corrugation potential. If so one says that the lattices exhibit a Kurdjumov-Sachs (KS) orientational relationship [6] .

### Local Epitaxy on steel/hard coating interfaces

As described before the misfit between two crystals in contact is important for epitaxy to occur. Lattice parameter and crystal type for some hard coating materials and phases present in high-speed steel (HSS) are summarised in Table 2.1.

---

[6] Another minimum occurs for a miss- orientation angle of zero degree, which corresponds to the so called Nishiyama-Wassermann (NW) orientational relationship, which is obtained by row matching parallel to the x-axis (see Figure 2.13a).

| Phase | Type | a in Å | c in Å | Ref. |
|---|---|---|---|---|
| TiN | B1 NaCl f.c.c | 4.24 | | [48] |
| TiAlN | B1 NaCl f.c.c. | 4.17 | | [32] |
| α-Fe | A2 W b.c.c | 2.86641 | | [91] |
| MC, M mainly V | B1 NaCl f.c.c | 4.18 | | [48] |
| WC (at 6.13% C ) | $B_h$ WC simple hexagonal | 2.9004 | 2.8311 | [92] |
| $W_2C$ | $L'_3$ $W_2C$ hexagonal | 2.99704 | 4.7279 | [91] |
| FeO | B1 NaCl f.c.c | 4.31 | | [48] |
| γ-Fe | A1 Cu f.c.c | 3.60 | | [91] |
| Cr | A2 W b.c.c | 2.8839 | | [91] |
| CrN | B1 NaCl f.c.c | 4.140 | | [92] |

**Table 2.1:** Lattice parameters and crystal type of steel phases and various coatings.

Helmersson *et al.* [48] observed an increased adhesion of TiN (scratch test, corrected for different substrate hardness) for a higher metal-carbide (MC) content in the HSS substrate. The same was valid for the presence of FeO instead of $Fe_2O_3$ or $Fe_3O_4$ on the interface. Both observations were explained to be a result of structural matching (see Table 2.1) and therefore low energy interface formation. The epitaxial growth of TiN on the MC phase of HSS was shown by XTEM investigations [93], [94]. For ion plating with an ion to Ti arrival rate ratio of $\geq 6.7$ an epitaxial relationship between TiN grain and the martensitic phase of the substrate material was found by XTEM observation [95]. Local epitaxy of TiN on the austenitic phase is reported by Håkansson *et al.* [96]. An epitaxial relation between $Ti_{0.501}Al_{0.498}Nb_{0.001}N$ grown on ferritic steel (after cathodic arc ion etch from a $Ti_{0.5}Al_{0.5}$ target) was found by Petrov *et al.* [97]. The film grains were rotated about 45 degree with respect to the [001] substrate grain axis in order to reduce the lattice mismatch of 31% to 3% compression. In comparison, a coating grown under the same parameters on the same substrate material but after $Ti_{0.85}Nb_{0.15}$ cathodic arc ion etching shows no sign of local epitaxy. XTEM imaging indicated that the ion etch modified region in the latter case appears to be amorphous (Nb-interlayer). For the growth of $Ti_{0.44}Al_{0.53}Cr_{0.03}N$ and $Ti_{1-x-y}Al_xNb_yN$ coatings deposited on austenitic stainless steel after $Ti_{0.5}Al_{0.5}$ CA ion etching local epitaxy was observed [86].

# Chapter 3

# Experimental methods

## 3.1 Coating deposition

### 3.1.1 Substrate preparation

The experiments were carried out on four different substrate materials, namely low carbon steel, austenitic stainless steel high speed steel (HSS) and tungsten carbide (WC-Co, 6-9 % Co). The chemical compositions for these materials are summarised in Tables 3.1 to 3.3.

HSS and tungsten carbide are of special interest since these substrate materials are used in metal cutting applications. However, these materials are not always suitable for evaluation of certain properties. For example, stress determination is carried out on austenitic stainless steel and low carbon steel. Low carbon steel was chosen for several reasons: low carbon steel

(I) does not contain any of the elements used as bombarding species such that no interference occurs for elemental profiling across the interface;

| El. | C | Si | Mn | S | P | Fe |
|---|---|---|---|---|---|---|
| % | 0.08 | 0.07 | 0.85 | 0.23 | 0.05 | rest |

**Table 3.1:** Composition of low carbon steel,

| El. | Cr | Ni | Mo | Mn | Si | Cu | N | C | S | P | Fe |
|---|---|---|---|---|---|---|---|---|---|---|---|
| % | 16.83 | 11.03 | 2.10 | 1.54 | 0.48 | 0.41 | 0.038 | 0.029 | 0.027 | 0.027 | rest |

**Table 3.2:** Composition of stainless steel

| El. | W | Mo | Cr | V | C | Co | Si | Mn | P | S | Fe |
|---|---|---|---|---|---|---|---|---|---|---|---|
| % | 6.00-<br>6.57- | 4.86-<br>5.02- | 3.76-<br>4.06- | 1.83-<br>1.84- | 0.85-<br>0.88 | 0.42-<br>0.51 | 0.25-<br>0.27 | 0.18-<br>0.25 | 0.030-<br>0.027 | 0.016-<br>0.019 | rest |

**Table 3.3:** Composition of HSS

(II) has large grain sizes compared to all other substrate materials, such that light microscopy can be employed to reveal topographical changes and substrate related crystal size effects in the TiAlN coating are easily detected;

(III) has the same crystal structure as the matrix of HSS (b.c.c. with a similar lattice parameter);

(IV) is easy to use for Transmission Electron Microscopy (TEM) sample preparation, in spite of handling in the TEM is difficult due to its magnetism.

The shape of all substrate materials is summarised in Table 3.4. Sheet material was used for a fast preparation of TEM samples whereas all other investigation were carried out on the disks when not stated differently.

All samples were polished using 1 $\mu$m diamond paste in the final stage. This

| Material | Disk | Sheet | Tool |
|---|---|---|---|
| Stainless steel | 30 mm × 3 mm | 25 mm × 25 mm × 0.7 mm | none |
| Low carbon steel | 30 mm × 3 mm | 25 mm × 25 mm × 0.7 mm | none |
| HSS | 30 mm × 3 mm | none | none |
| Tungsten carbide | 15 mm × 6 mm | none | 8 mm milling cutter |

**Table 3.4:** Summary of substrates used

resulted in a roughness of $R_a = 5\,\text{nm}$ for stainless steel and low carbon steel and $R_a = 10\,\text{nm}$ for HSS. The substrates were cleaned in an automatic ten station industrial cleaning line containing a range of aqueous based alkali detergents, de-ionised water and were dried in vacuum by radiant heating shortly before loaded to the vacuum chamber.

### 3.1.2 Deposition process

All ion bombardment and coating deposition experiments were performed in an industrial scale combined steered cathodic arc/unbalanced magnetron (CA/UBM) deposition system HAUZER HTC 1000-4-ABS ([98] and [31]), as shown schematically in Figure 3.1. The Cr target/cathode (alternatively Ti, Nb or V) is operated in the steered CA mode using the permanent magnets shown in the withdrawn position ($B \approx 50\,\text{G}$). For Ar-ion bombardment and during all coating depositions, the TiAl

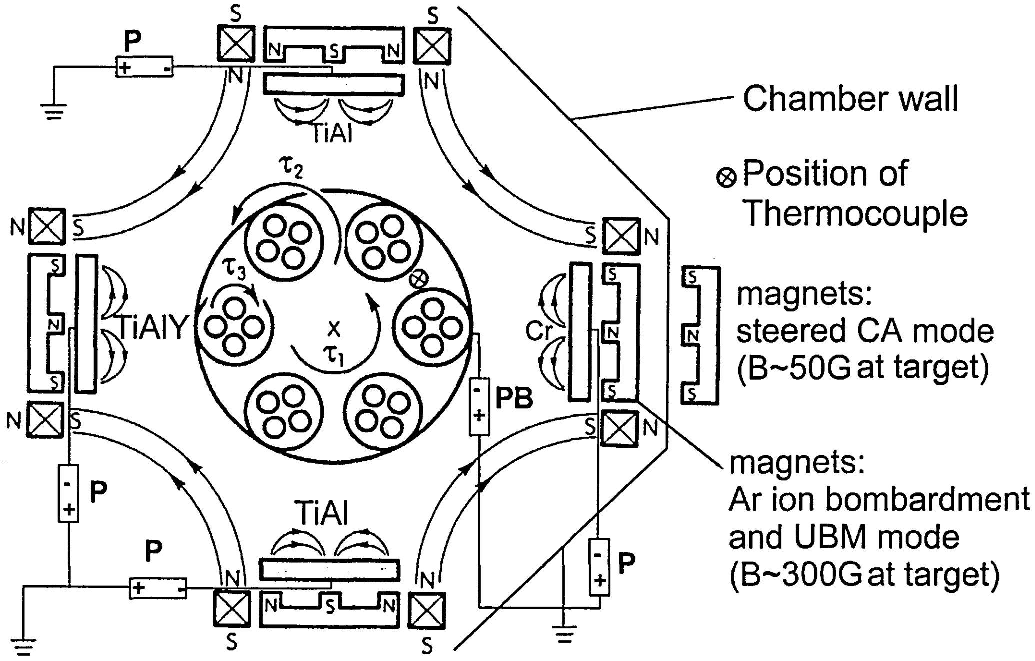

**Figure 3.1:** Schematic cross-section of HAUZER HTC 1000-4-ABS. The four individual power supplies for each cathode are labelled with P and PB stands for the bias power supply. The power supplies for the electro-magnetic coils are not shown.

and TiAlY target/cathodes are used in the UBM mode ($B \approx 300\,\mathrm{G}$) magnetically coupled to form a closed field for an enhanced ionisation and a high ion current density at the substrate surface. The substrates undergo 3-axis planetary rotation during ion bombardment as well as deposition. The average distance between the targets/cathodes and the substrates is 25 cm. The vacuum chamber is evacuated to a pressure of $6 \times 10^{-3}$ Pa and heated to a temperature of 400 °C (measured using a thermocouple) prior to any plasma experiments in order to minimise target poisoning due to desorption of residual gases (mainly water vapour). The pump down and heating cycle is followed by a 20 minute (if not stated differently) ion bombardment step. Five types of experiments were carried out, varying

(I) the ion species (Figure 3.2a),

(II) the ion energy (Figure 3.2b),

(III) exposure time to ion bombardment (Figure 3.3a),

(IV) working gas pressure (Figure 3.3b), and

(V) arc current (Figure 3.3c).

In most cases ion bombardment was followed by the deposition of 100 nm TiAlN. In addition, samples with 300 nm TiAlN followed by 3.2 $\mu$m TiAlYN were fabricated. For experiment (II) a series of exclusively sputter cleaned samples (no coating deposition) was produced. During ion bombardment the substrate temperature rises from 400°C to 450°C for a negative bias voltage $U_s = 1200\,\mathrm{V}$. In the case of Ar-ion bombardment and Cr-ion bombardment at lower bias voltage additional radiant heating is required to maintain a temperature of 450 °C. This temperature was kept constant during the TiAlN reactive deposition process taking place at a gas pressure of 0.35 Pa (Ar/$N_2$ mixture). The gas flow was controlled by a proportional integrating differential controller with feedback to total pressure with a constant Ar flow. The target power on the two TiAl targets was 8 kW, resulting in the deposition of 100 nm TiAlN in 10 minutes.

Pump down & heating
T=400°C p=$6\times10^{-3}$Pa

Target cleaning
2min 3x 1kW

| **Ar (UBM)** | **Cr arc** | **V arc** | **Ti arc** |
|---|---|---|---|
| $U_s$=1200V | $U_s$=1200V | $U_s$=1200V | $U_s$=1200V |
| 4x175V | 1x $I_a$=100A | 1x $I_a$=100A | 1x1=100A |
| $p_{Ar}$=5x10''Pa | $p_{Ar}$=$6\times10^{-2}$Pa | $p_{Ar}$=$6\times10^{-2}$Pa | $p_{Ar}$=$6\times10^{-2}$Pa |
| t=20min | t=20min | t=20min | t=20min |
| T->450°C | T->450°C | T->450°C | T->450°C |

UBM: Us=75V T=450°C
2x8kW(TiAl): 30 min
3x8kW: 3h 30 min

UBM: Us=75V T=450°C
2x8kW(TiAl): 10 min

Cool down

Pump down & heating
T=400°C p=$6\times10^{-3}$Pa

Target cleaning
2min 3x 1kW

| Cr arc | Cr arc | Cr arc | Cr arc |
|---|---|---|---|
| **U=400V** | **U=600V** | **U=1000V** | **U=1200V** |
| 1x $I_a$=100A | 1x $I_a$=100A | 1x1=100A | 1x1=100A |
| $p_{Ar}$=$6\times10^{-2}$Pa | $p_{Ar}$=$6\times10^{-2}$Pa | $p_{Ar}$=$6\times10^{-2}$Pa | $p_{Ar}$=$6\times10^{-2}$Pa |
| t=20min | t=20min | t=20min | t=20min |
| T->450°C | T->450°C | T->450°C | T->450°C |

UBM: Us=75V T=450°C
2x8kW(TiAl): 30 min
3x8kW: 3h 30 min

UBM: Us=75V T=450°C
2x8kW(TiAl): 10 min

Cool down

**Figure 3.2:** Process parameters: variation of substrate sputter cleaning step in (a) ion species, (b) ion energy given by bias voltage *Us*.

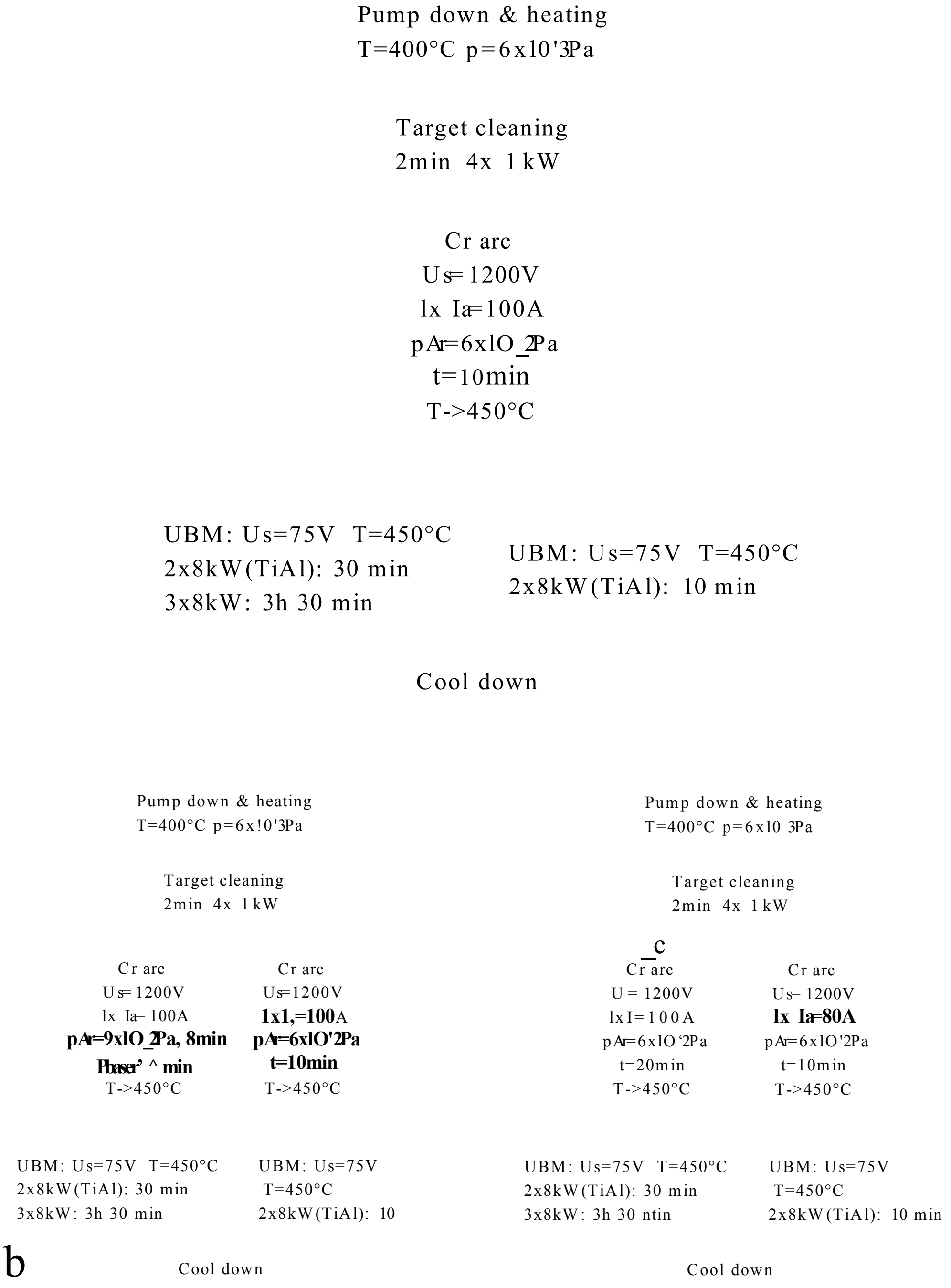

**Figure 3.3:** Process parameters: variation of substrate sputter cleaning step in (a) exposure time, (b) gas pressure, and (c) arc current.

In case of the deposition of $3.5\mu$m nm thick TiAlN based coatings the two TiAl targets were used at power of 8 kW each for 30 minutes. Then 8 kW were also applied to the third (TiAlY) target. TiAlYN deposition was carried out for 210 minutes. Unbalancing coils at a current of 6 A were used for increased ionisation and to improve the control of the magnetic coupling. The bias voltage during UBM deposition was routinely $U_s = 75$ V.

## 3.2 Topography of surfaces

### 3.2.1 Reflected light microscopy

An *Olympus microscope* with attached CCD-camera was used. This, together with the *analysis 3.0* software, allowed to record digital images. No image processing was performed to enhance the contrast. For maximum contrast a very small aperture size was used.

### 3.2.2 Atomic force microscopy (AFM)

A METRIS 2000 AFM was used in contact mode. In the AFM the sample is moved relative to a sharp tip, which is integrated into the end of a cantilever spring. The atomic forces between the sample and the tip are measured employing a laser and detector to measure the cantilever motion. The laser beam is focused on to a split photodiode detector. The beam reflected by the cantilever is then focused onto the middle of the split detector such that the difference signal between the two halves is zero.

Deflection of the cantilever results in a difference of the illumination of the upper and lower half of the split detector. The difference signal is compared to a selectable reference set point. The error signal is amplified and the sample is moved up and down in order to eliminate the measured error signal. In this way, the desired interaction force is maintained constant. The vertical sample movement is recorded as a function of x-y sample position and corresponds to the topography of the sample surface [99].

## 3.3 Structure and phase analysis

### 3.3.1 X-ray diffraction (XRD)

In XRD monochromatic X-rays of wavelength $\lambda$ are focused on the crystalline specimen, where they are reflected according to Bragg's law (equation 3.1)

$$n\lambda = 2d \sin\theta, \tag{3.1}$$

with $n$ an integer and $d$ the inter-planar spacing. The angle $\theta$ is measured between the crystal plane and the incident beam. In *parallel beam glancing angle XRD* the angle of incidence with respect to the sample surface remains fixed at a low angle, in this case 0.5 degrees, and the detector is moved. The number of counts as a function of detector position contains information about the orientation and spacing of the reflecting planes. The latter is characteristic for the phases present. Phases can be identified by comparison with the JCPDS [91] data base. The advantage over conventional XRD is that it is surface sensitive as a result of the grazing incidence of the X-ray beam. Measurements were carried out in a *Philips PW 1710* automated diffractometer using $\mathrm{CuK}_\alpha$ radiation.

### 3.3.2 Transmission electron microscopy (TEM)

A typical TEM consists of a condenser lens, objective lens, and intermediate and projector lenses. An electron transparent sample (thickness of less than 200 nanometres) is illuminated by a spread electron beam (parallel illumination). For this experiment the electron beam was generated in an electron source equipped with a $\mathrm{LaB}_6$ crystal. An accelerating potential of 200 kV was used.

The image contrast can arise from several sources, such as atomic number difference, phase difference, or diffraction contrast. The sample is assumed to be crystalline with diffraction occurring according to Bragg's law. All rays diffracted through the same angle are focused to a single point at the back focal plane of the objective lens. The array of spots formed at the back focal plane is the diffraction pattern. From its spacing and shape the lattice parameter, crystal structure, and orientation of the diffracting crystal can be determined.

By placing the objective aperture to allow only the undiffracted beam to pass a *bright field (BF) image* is obtained. Thus, in the BF image dark areas indicate that diffraction is occurring. An aperture can be used to limit the specimen volume that contributes to the formation of the diffraction pattern, which is then called *selected area diffraction pattern* (SADP). Alternatively, the objective lens aperture may be placed such that only a diffracted beam passes and the image obtained is a *dark field (DF) image.* The drawback of TEM analysis is the time and effort required for specimen preparation [100].

TEM specimens were prepared by mechanical grinding and polishing and subsequent ion beam milling in a GATAN PIPS 691. A step-by-step guide including details for the ion beam milling parameters is found in Appendix B.

## 3.4 Measurement of the elemental distribution across interfaces in the scanning transmission electron microscope

### 3.4.1 Scanning transmission electron microscope (STEM)

In contrast to the parallel illumination in conventional TEM, in the STEM a very fine focused electron beam is rastered across the specimen. This is achieved by demagnifying the electron source (here a field emission gun (FEG)) in which case probe sizes of several Å can be realised. However, there is a trade-off between probe size and electron current that strikes the specimen.

The electrons can interact with the core electrons in the specimen. The incident electron can excite a core electron in the specimen to some unoccupied state (inelastic interaction). Thus, it looses energy. Conversely, it may be elastically scattered with no energy loss. In *electron energy loss spectroscopy* (EELS) the transmitted electron beam passes through an magnetic prism such that the energy loss spectrum can be recorded. This reveals the one-electron conduction band density of states (DOS) partitioned by element, site, and angular momentum [101]. Thus, EELS provides information on the nature of atoms and their bonding [102]. The excitation process leaves behind a core hole in the exited atom, which can be filled by any less deeply bound core level or valence electrons. The excited core-hole state can decay either by emitting Auger-electrons or by emitting an X-ray photon. The latter process is used in energy dispersive X-ray analysis (EDX). The techniques of EELS and EDX are complementary in many respects. EDX is more widely spread because it is easier to use and to interpret. Both techniques were available in the *Vacuum Generators HB 501* used for these experiments. The HB 501 was operated at an accelerating voltage of 100 kV. A *Link ISIS* system was used for EDX analysis and a GATAN spectrometer for EELS.

For interface investigations a high spatial resolution is desirable. This is limited not only by probe size and beam broadening in the specimen but also by positioning the cross-section exactly in an edge on orientation with respect to the electron beam. To achieve this for the samples investigated here (polycrystalline with unknown crystal orientation with respect to the interface plane) annular DF imaging was used. The specimen was tilted until a maximum contrasts at the interface was observed.

### 3.4.2 STEM-EELS

As mentioned above EELS is a more complex technique than EDX but it yields additional information. For example, it provides rapid information regarding the sample thickness. The sample thickness is a major limitation for this technique because multiple scattering can greatly increase the background of ionisation edges below 1000eV, making these edges invisible for specimen thicker than 100 nm or even 50 nm [103]. Furthermore, it is a complex experimental procedure, and quantification requires extensive processing of the spectrum.

### Experimental procedure

The spectrometer is focused by adjusting a pair of pre-spectrometer quadrupoles such that the zero loss peak has a gaussian shape with a minimum width and maximum height. Next, the spectrometer was calibrated by using known energies spanning the spectral range. Here, the zero loss peak and the Fe L edge were used. A PEELS (parallel EELS) system was employed. It comprises a YAG scintillator coupled via a fibre to a semiconductor photodiode array in the dispersion plane of the spectrometer. The resultant spectrum accumulates across the whole energy range simultaneously during the selected integration time (here 10 $s$). The integration time is very small compared to the one used for EDX because in EELS the collection efficiency can approach 100 %. This is because it relies on the energy losses of the primary beam that is strongly peaked in the forward direction. There was no need for correction of sample or beam drift, due to this short integration time. For each point at the specimen the dark current was collected before the spectrum was recorded. In addition to the high loss region the zero loss peak and the adjacent low loss region were collected. A collection angle of 15 mrad was used.

### Quantification

The GATAN ELP software was applied for all spectrum processing and quantification. The dark current was subtracted from each spectrum. The edges were identified and the background subtracted. The background was fitted using equation 3.2

$$I = AE^{-r}, \tag{3.2}$$

with $I$ as the intensity of the channel of energy loss, and $E$ the energy, $A$ and $r$ the constants for a particular fit. Edge integration windows with a width between 20 and 70 eV were used starting at the edge onset. For the determination of the partial ionisation cross-section the *Hartee-Slater* model was used.

The sample thickness $t$ (in units of mean free path $\lambda$) was estimated from the intensity of the zero loss peak $I_0$ and the total intensity of the spectrum. The latter was approximated by the intensity in the low-loss region $I_l(E \leq 50eV)$ using equation 3.3.

$$t = \lambda \ln \frac{I_l}{I_0}. \tag{3.3}$$

### 3.4.3 STEM-EDX

An integration time of 100 s (lifetime) was necessary in order to ensure a peak in the order of 1000 counts above background. To avoid the loss of spatial resolution due to beam or specimen drift a manual drift correction was performed every 25 seconds. The ISIS software was used for quantification assuming a sample thickness of 50nm.

## 3.5 Etch rate determination

Etch rates were measured on polished austenitic stainless steel substrates. The centre part of a round specimen was covered by a wedge shaped washer in order to minimise an influence of sample geometry. Care was taken to fix the washer such that no gap remained between substrate and washer. These samples were fixed together with other specimen on substrate holders, which were undergoing 3 axis planetary motion during metal ion bombardment. No coating was deposited. The step height was measured using both a *UBM Laser profilometer* and a *Talysurf*, respectively. A profile line of 1 mm length was recorded and then levelled in order to measure the step height.

## 3.6 Stress measurements by X-ray diffraction

### 3.6.1 Basic principles

XRD can be used to determine stress due to the change in lattice parameters for a strained material. Relative to the normal of the sample surface the strain $\epsilon_{\phi\psi}$ in a direction inclined to it at angle $\psi$ and at an angle $\phi$ to the principal stress axis is related to the lattice spacing in that direction $d_{\phi\psi}$ and the equilibrium lattice spacing $d_0$ by equation 3.4 [104]

$$\begin{aligned}
\epsilon_{\phi\psi}^{hkl} = \frac{d_{\phi\psi}^{hkl} - d_0^{hkl}}{d_0^{hkl}} = \\
\frac{1+\nu^{hkl}}{E^{hkl}}(\sigma_x \cos^2\phi + \tau_{xy}\sin^2\phi + \sigma_y \sin^2\phi - \sigma_z)\sin^2\psi \\
+\frac{1+\nu^{hkl}}{E^{hkl}}\sigma_z - \frac{\nu^{hkl}}{E^{hkl}}(\sigma_x + \sigma_y + \sigma_z) \\
+\frac{1+\nu^{hkl}}{E^{hkl}}(\tau_{xy}\cos\phi + \tau_{yz}\sin\phi)sin^2\psi \qquad (3.4)
\end{aligned}$$

where *hkl* denotes a specific Bragg reflection and $\nu^{hkl}$ and $E^{hkl}$ are Poisson's ratio and Youngs modulus, respectively in that direction. $\sigma_x$ and $\sigma_y$ are the stresses acting in x and y direction, respectively. $\tau_{xy}$ stands for the shear stress acting normal to the x axis in the direction of the y axis. When shear stress is not present (biaxial and triaxial stress conditions) equation 3.4 can be simplified. In particular in the case of a biaxial stress the out of plane z-related components are all zero and assuming an uniform biaxial stress one obtains

$$\epsilon_{\phi\psi}^{hkl} = \frac{d_{\phi\psi}^{hkl} - d_0^{hkl}}{d_0^{hkl}} = \frac{1+\nu^{hkl}}{E^{hkl}}\sigma_\psi \sin^2\psi - \frac{2\nu^{hkl}}{E^{hkl}}\sigma_\psi. \qquad (3.5)$$

Equation 3.5 can be used to measure stress employing two different XRD geometries, namely *Bragg-Brentano geometry* using an $\Omega$ goniometer. In that case an average stress value considering the depth is derived. The second method is the *glancing angle technique* that can be used for depth profiling.

### 3.6.2 Bragg-Brentano geometry

In the usual Bragg-Brentano geometry sample and detector movement are coupled such that for a rotation of the sample about an angle $\theta$ the detector is moved about an angle $2\theta$. Hence, only lattice planes parallel to the sample surface ($\psi = 0°$) will give diffraction peaks when Braggs law (Equation 3.1) is obeyed. This is shown in Figure 3.4 for two different lattice spacings. Thus the the lattice spacing (*d-spacing*) in z-direction is measured. Since the film can expand freely in that direction the stress is zero and the change in lattice spacing compared to a non deformed cell has an maximum value (see Figure 3.5). For stress measurements sample and

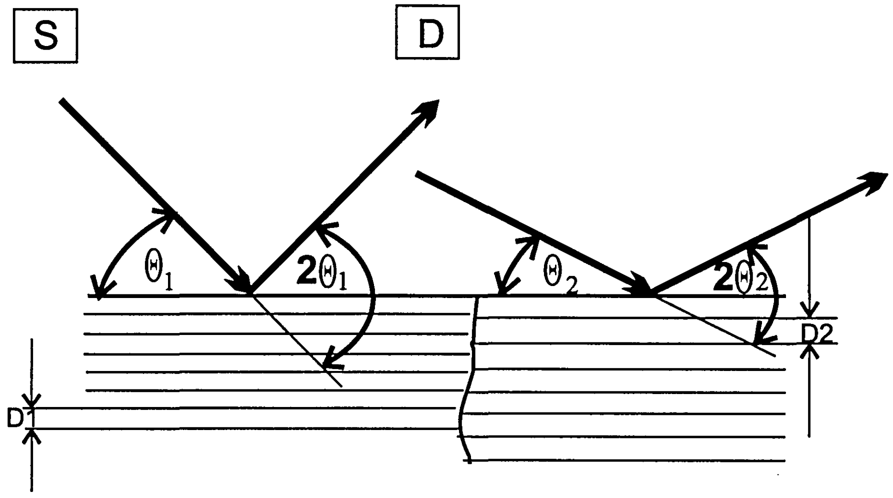

**Figure 3.4:** Normal Bragg Brentano geometry, where only lattice planes parallel to the sample surface give rise to peaks. This is because the movement of source and detector is coupled such that when the incident angle is changed by $\theta$ the detector is moved about $2\theta$.

detector movements are decoupled. The detector is set to a known diffraction peak in ($\psi = 0$ conditions) thus selecting a certain set of (hkl) lattice planes with a certain d-spacing. Then the specimen is stepped trough a defined range of angles $\pm\psi$ as shown in Figure 3.6. A plot of the lattice spacing as a function of $sin^2\psi$ yields a straight line with a slope $\frac{1+\nu^{hkl}}{E^{hkl}}\sigma_\psi$.

### 3.6.3 Glancing angle method

The Glancing angle method is suited for thin films as it is the case here (film thickness 100 nm). When the angle of incidence $\gamma$ is set the diffraction angle $\chi$ is given by equation 3.6

$$\chi = \theta - \gamma \tag{3.6}$$

with the *Bragg angle* $\theta$. Small incidence angles are utilized, here $0.5^o$, which results in a small penetration depth of the X-rays. For example using $CuK_\alpha$ radiation and $\gamma = 0.5^o$ results in a penetration of about 100nm in TiN [104]. In the glancing angle technique all diffraction peaks within the instrumentally permitted range are used for stress determination and diffraction occurs at a given, near constant depth of

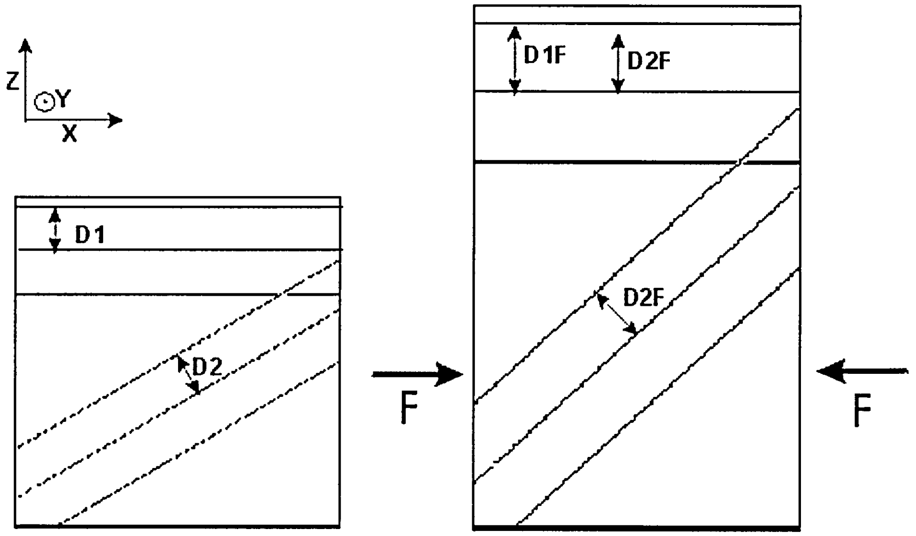

**Figure 3.5:** Principle of stress measurements: Lattice planes with the same lattice spacing ($D1 = D2$) with different $\psi$ in a cubic cell are shown on the left. On the right the cube is deformed in $z$-direction due to the forces in the $xy$ plane. Deformation in $x$ and $y$ direction is not possible resulting in stress in the xy plane. A maximum change in lattice spacing $\Delta D1 = D1_F - D1$ is observed for planes with $\psi = 0°$). For all other planes $\Delta D$ is smaller as can be seen by comparing $D1_F$ and $D2_F$. For $\psi = 90°$ one obtains $\Delta D = 0$ and hence a lattice spacing equal to that in the non deformed cell.

penetration see Figure 3.7. Equation 3.5 can be written as

$$\begin{aligned}\epsilon_{\phi\psi}^{hkl} &= \frac{d_{\phi\psi}^{hkl} - d_0^{hkl}}{d_0^{hkl}} \\ &= \frac{1+\nu^{hkl}}{E^{hkl}}\sigma_\chi \sin^2\chi - \frac{2\nu^{hkl}}{E^{hkl}}\sigma_\chi \\ &= \frac{a_{\phi\chi}^{hkl} - a_0^{hkl}}{a_0^{hkl}} \qquad (3.7)\end{aligned}$$

The second part of equation 3.7 holds only for a cubic material with a equilibrium lattice parameter $a_0$. If the bulk elastic constants and the equilibrium lattice parameter are known the stress can be determined by plotting the lattice parameter $a^{hkl}$ versus $sin^2\chi$. This should result in a straight line with the slope $m$ provided no shear stress is present. In that case $\sigma_\chi$ is given by equation 3.8 assuming isotropic

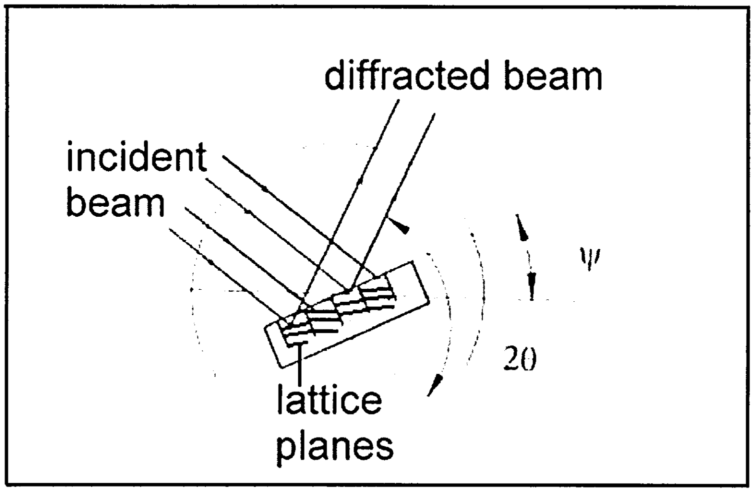

**Figure 3.6:** Schematic of stress determination using Bragg Brentano geometry in an Ω goniometer(from [69]).

elastic constants

$$\sigma_\chi = \frac{m}{a_0}\frac{E}{1+\nu}. \tag{3.8}$$

## 3.7 Determination of practical adhesion

### 3.7.1 Scratch test

For scratch testing a CSEM REVETEST instrument was used. The load was progressively increased choosing $\frac{dL}{dx} = 10\,\mathrm{N/mm}$ as advised in reference [70]. The tip radius of the *Rockwell C* diamond was 200 $\mu$m. All samples were scratched with the same diamond tip. Before performing a scratch test the diamond tip was cleaned with *IMS* and a soft tissue. The load at which the first adhesive failure was visible by reflected light microscopy was defined as critical load $L_c$. TiAlN/TiAlYN coatings (thickness 3.5 $\mu$m) on tungsten carbide and high-speed steel substrates were tested.

### 3.7.2 Rockwell C indentation

A mechanically stable crack is introduced into the coating-substrate interface by a Rockwell C indention. A Rockwell C indentation is produced when a cone shaped

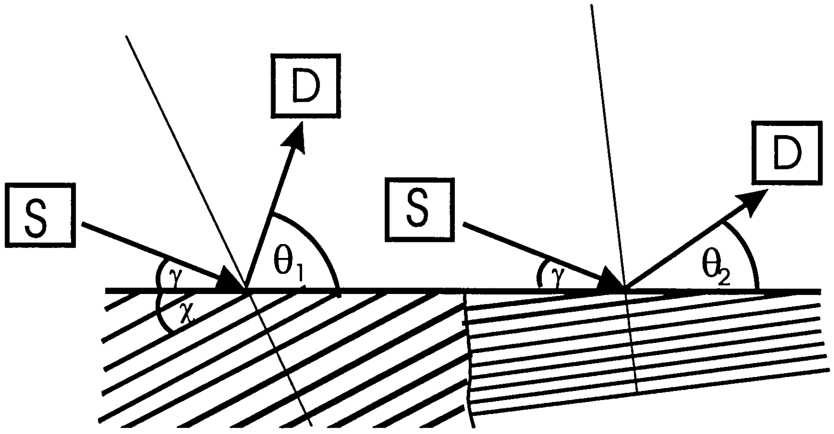

**Figure 3.7:** Glancing angle geometry: the incidence angle is fixed and the detector is moved. Therefore planes with small d-spacing give peaks at small angles $\theta$ (on the right).Large lattice spacings gives rise to peaks at large $\theta$ (on the left).

diamond tip (tip angle 120°) is first pressed into the test piece with a force of 98.07 N. The load is then increased to 1373 N before it is released. The resistance to crack propagation is used to assess the practical adhesion. Crack propagation at the interface and delamination of the coating will only occur if the interface toughness is lower than that of the coating or substrate. A *DIN guide line* [83] suggests that the practical adhesion can be assessed by comparing crack propagation and the delaminated area around the Rockwell indentation (reflected light microscopy, magnification x100) with six given reference images. In that way a classification ranging from excellent adhesion to total failure is obtained.

## 3.8 Determination of tool life

A MAZAK FJV-25 high-speed machining centre was available to measure tool performance in hardened A2 steel (58 HRC) with the following parameters: cutting speed: 385 m/min (corresponds to a spindle speed of 15000 rpm), axial feed: 4 mm, radial feed: 0.1 mm, linear feed: 0.1 mm per revolution in dry conditions (see Figure 3.8). Eight millimetre diameter ball nosed solid carbide (*Hydra-Marwin*) milling cutters coated with 3.5 $\mu m$ TiAlN/TiAlYN were tested. Machining trials were stopped

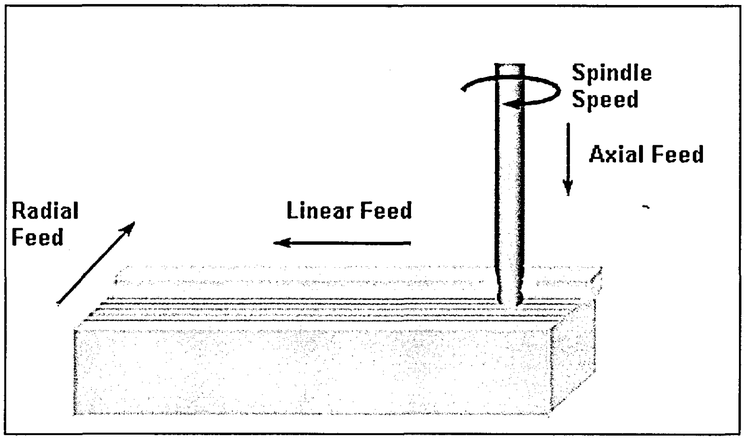

**Figure 3.8:** Schematic drawing of cutting test (from [105]).

when the power on the spindle exceeded a 10% increase since a higher power led to tool breakage. The time at which this condition was reached defines the tool life.

# Chapter 4

# Substrate surface modification by ion bombardment

## 4.1 Introduction

To understand substrate surface modifications caused by ion bombardment the condition of the initial substrate surface should be known. Therefore it is characterised first in Section 4.2.1. In the following Sections the effect of various process parameters of the ion bombardment procedure like ion species, ion energy, exposure time and working gas pressure on substrate surface topography, microstructure and microchemistry are shown and discussed.

## 4.2 Results

### 4.2.1 Initial substrate surface

Figures 4.1 and 4.2 illustrate the topography of a polished low carbon steel surface as observed by AFM imaging and reflected light microscopy, respectively. Clearly visible are polishing marks that lead to a roughness of $\mathrm{R_a} = 5\,\mathrm{nm}$. The optical micrograph (Figure 4.2) also manifests the presence of some non-metallic inclusions in the steel. In the as polished condition the metallurgical microstructure could not

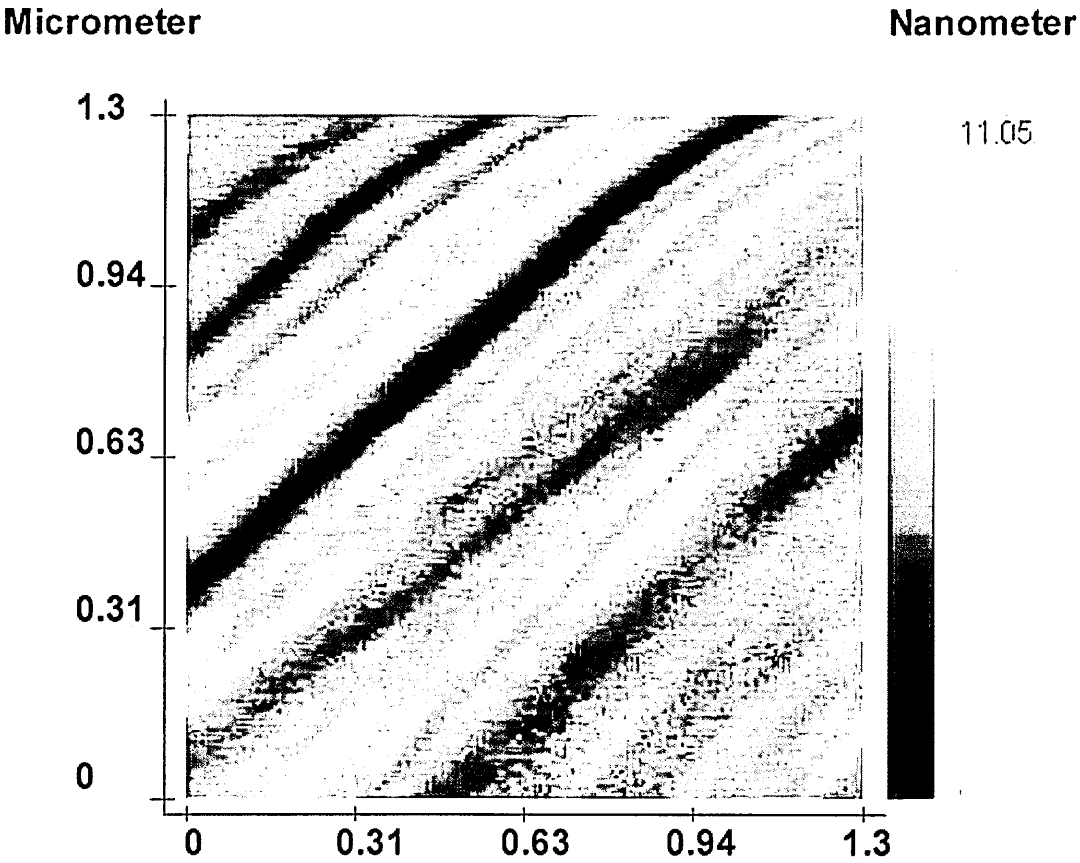

**Figure 4.1:** AFM image of polished low carbon steel surface ( 1$\mu$m finish).

be observed by optical microscopy.

XTEM imaging (Figure 4.3) reveals that the surface of the low carbon steel sheet material used for this experiments is characterised by a several micrometer thick surface region (Figure 4.3b). It consists of much smaller grains compared to the grain size of the bulk material (Figure 4.3a). In addition, the DF image of the surface region shown in Figure 4.3c demonstrates that the grains are elongated parallel to the substrate surface.

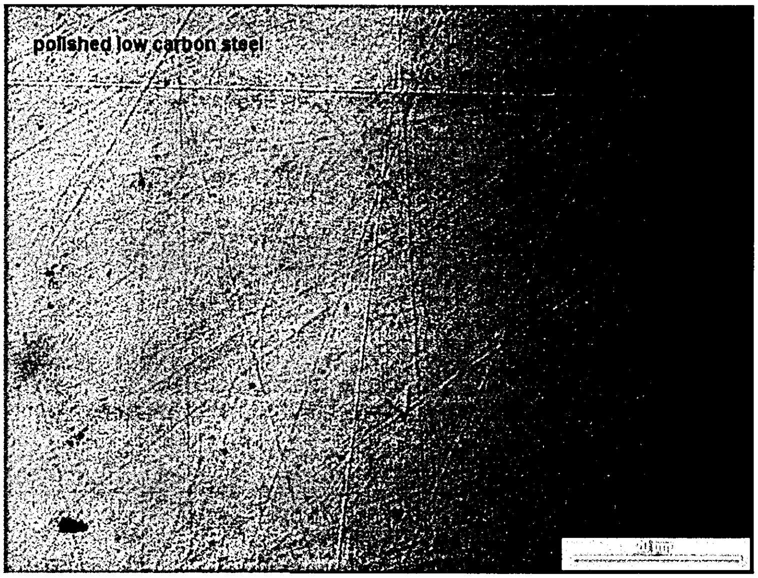

**Figure 4.2:** Optical micrograph of polished low carbon steel surface.

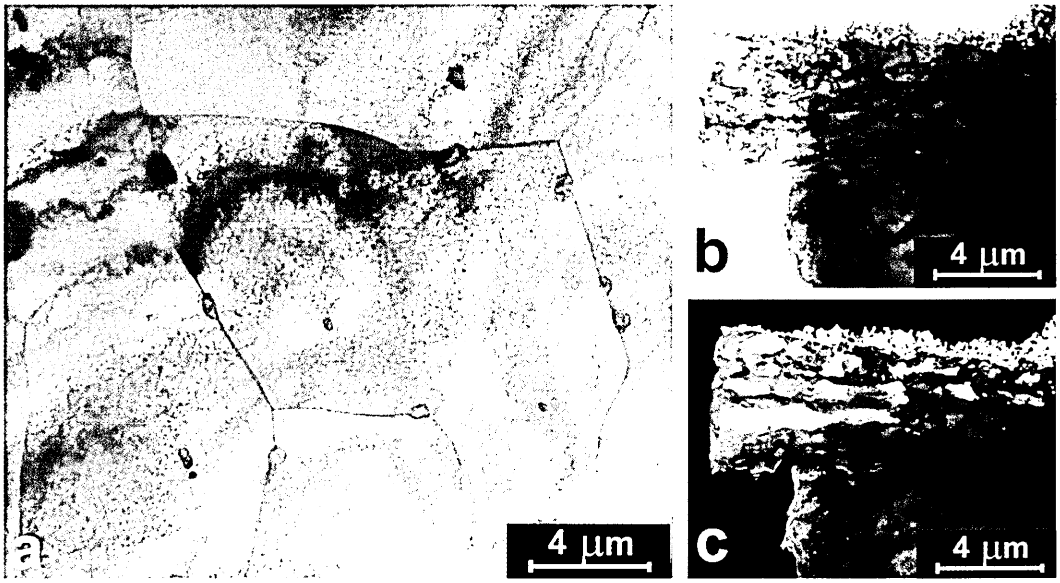

**Figure 4.3:** XTEM images of 1 $\mu$m polished low carbon steel: (a) BF image of bulk material, (b) BF image of surface region with small grain size, and (c) DF of surface region showing elongation of grains near the surface.

### 4.2.2 Influence of ion species

#### Ion bombardment induced topography changes on various substrate materials

Substrate surface topography modification on a micron scale was observed by reflected light microscopy. A carbon steel surface, which was exposed to Cr ion bombardment at a $U_s$= 1200 V for twenty minutes (arc current 100 A) is presented in Figure 4.4(a) [1]. Several grain boundaries are visible due to differential etching. Roughness development within some grains is also observed, whereas other grains remain smooth. The same features are observed in a sample which was etched under the same conditions and subsequently coated with 100nm TiAlN (see Figure 4.4b). Thus, the surface topography of samples subjected to different ion bombardment

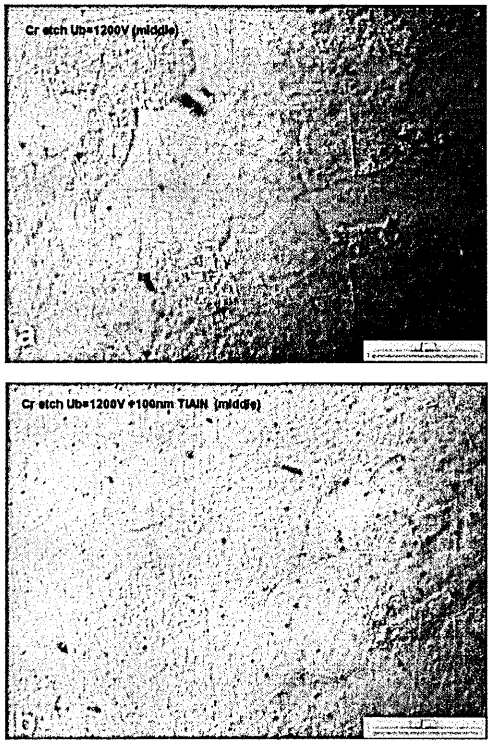

**Figure 4.4:** Optical micrographs of low carbon steel etched with Cr ions at $U_s$= 1200 V for 20 minutes: (a) surface after Cr etch and (b) surface after etching, subsequently coated with 100nm TiAlN.

---

[1] If not stated differently images were taken from the centre of the sample.

conditions can be compared in the only ion bombarded or ion bombarded and coated condition.

A comparison of surface topographies obtained by Ar-, V-, Ti- and Nb-ion bombardment, respectively ($U_s$= 1200V, 20 minutes exposure) of low carbon steel is given in Figure 4.5. These images can be compared to Figure 4.4b, where Cr ions were used. Although some contrast change related to different grains is present on a Ar-ion bombarded surface in Figure 4.5a the grain boundaries are hardly recognisable. In contrast, on all metal ion bombarded surfaces different substrate grains can be clearly distinguished (Figures 4.5b-d and 4.4b). This suggests that material removal (or etching effect) is achieved in all cases. However, a more pronounced etching effect is obtained by metal ion bombardment.

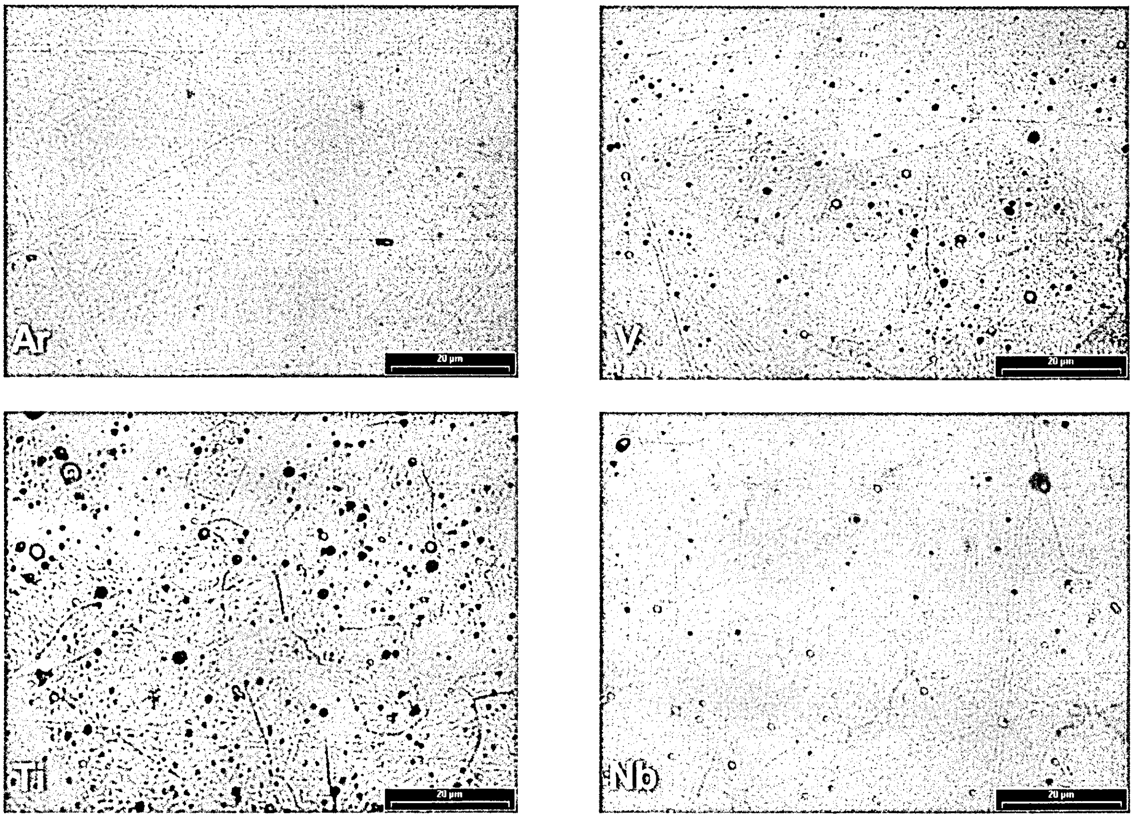

**Figure 4.5:** Optical micrographs of low carbon steel ion bombarded at $U_s$= 1200V for 20 minutes using: (a) Ar ions, (b) V ions, (c) Ti ions, and (d) Nb ions.

Despite this similarity, various metal ion etch treatments lead to different characteristic features. Typically for both Cr-ion (Figure 4.4) and V-ion (Figure 4.5b) etched low carbon steel surfaces is the roughness variation, which can be correlated to grain boundaries. Grains with either smooth or rough surfaces are observed. In contrast, Ti-ion etch surfaces (Figure 4.5c) exhibit less pronounced variations in roughness between individual grains. Instead the grain boundaries appear to be etched at a different rate compared to the grains. Nb-ion bombardment (Figure 4.5d) results in a surface characterised by a less developed grain structure exhibiting much smaller grains compared to all other metal ion etches.

Comparing Figures 4.4a and 4.5 reveals the presence of growth defects generated in the UBM coating stage on top of droplets deposited during metal ion bombardment. No droplet related growth defects are visible after exposure to Ar ions (Figure 4.5a). Only a small number of growth defects is observed for Nb- and Cr-ion pretreatment (Figures 4.5d and 4.4b, respectively). V-ion bombardment results in an increased number and average size of growth defects (Figure 4.5b). In case of Ti-ion bombardment both number and size are further increased (Figure 4.5c).

AFM imaging supported the reflected light microscopy results but gave additional information about the depth scale. Figure 4.6 shows the surface of a low carbon steel exposed to Cr-ion bombardment at $U_s$= 1200 V for 20 minutes. The height variation within an area of 25 $\mu$m × 25 $\mu$m is about 65 nm. This is mainly due to the presence of growth defects that are recognised as bright spots. Furthermore, several grain boundaries are visible as bright lines. They indicate less material removal at grain boundaries. At the same time it is evident that the height variation is correlated to different grains (drop shaped grain in Figure 4.6 is bright when compared to its neighbourhood). Figure 4.7 shows a droplet free 1.25 $\mu$m × 1.25 $\mu$m region of the low carbon steel sample displayed in Figure 4.6. A grain boundary that separates a rather smooth grain (right side of the image) from a grain with a more pronounced roughness is visible. The peak to peak height is in the order of a few nanometres. Figure 4.8 represents austenitic stainless steel surfaces, which were exposed to Cr-, V-, Ti- or Nb-ion bombardment, respectively. Cr- and V-ion bombarded stainless steel surfaces show evidence of material removal (grains can be

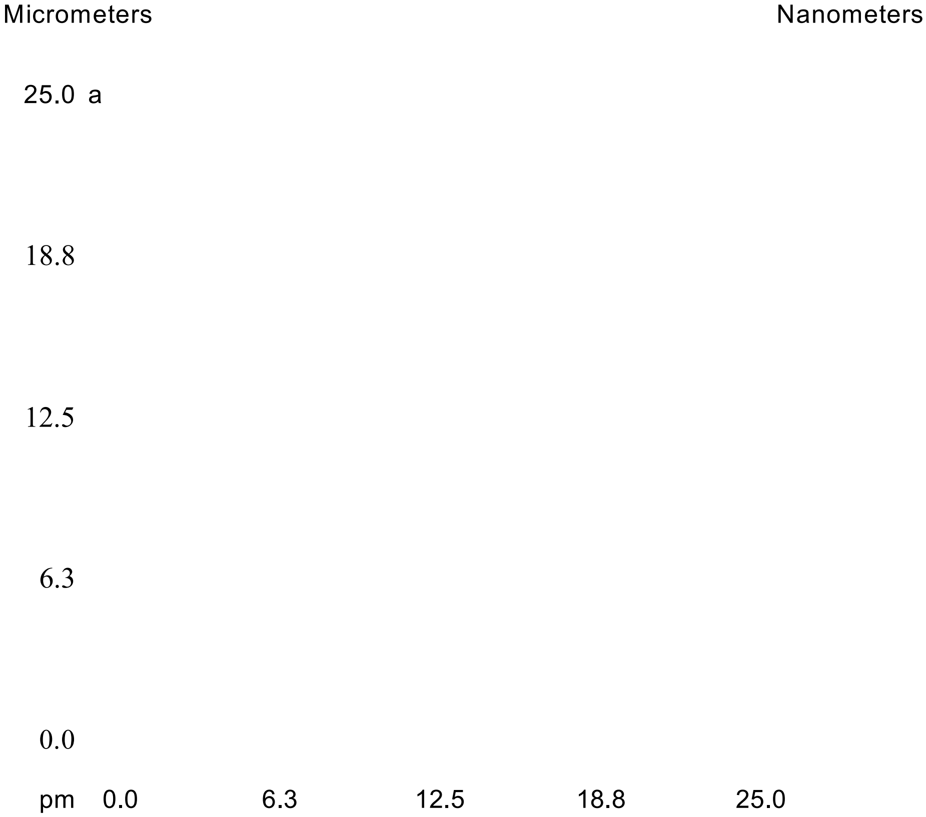

Figure 4.6: AFM image of low carbon steel exposed to Cr-ion bombardment at *Us* = 1200 V for 20 minutes.

distinguished). The appearance of the surface after Ti- and Nb-ion bombardment is similar to that of the as polished surface. Droplets deposited on the substrate surface are the only sign of metal ion bombardment. Droplet number and size are comparable for Cr- and Nb-ion bombardment and increases for V-ion and Ti-ion bombarded surfaces.

The same experiments were carried out for HSS substrates. The topography observed after being subject to Cr-, V-, Ti-, Nb- and Ar-ion bombardment, respectively is shown in Figure 4.9. Again, as in the case of stainless steel a roughening of the surface is observed for both Cr- and V-ion etching. In contrast Ti-, Nb- and

**Figure 4.7:** AFM image of low carbon steel exposed to Cr-ion bombardment at $U_S$ = 1200 V for 20 minutes. A grain boundary separating a smooth and a rough grain is visible. It is also evident that the grain boundary is etched at a lower rate than the grains.

Ar-ion bombarded surfaces show no clear indication of material removal.

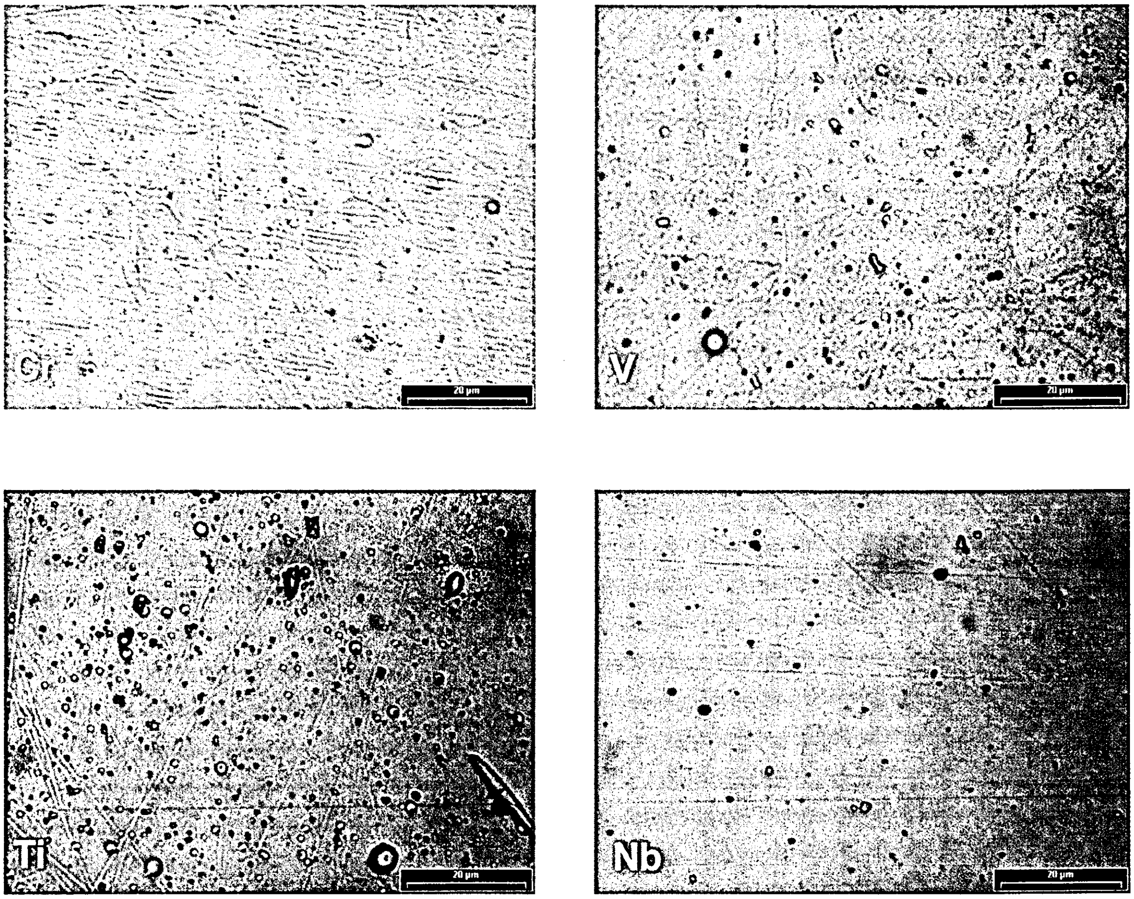

**Figure 4.8:** Optical micrographs of stainless steel, ion bombarded at $U_s = 1200\,\mathrm{V}$ for 20 minutes using: (a) Ar ions, (b) V ions, (c) Ti ions, and (d) Nb ions.

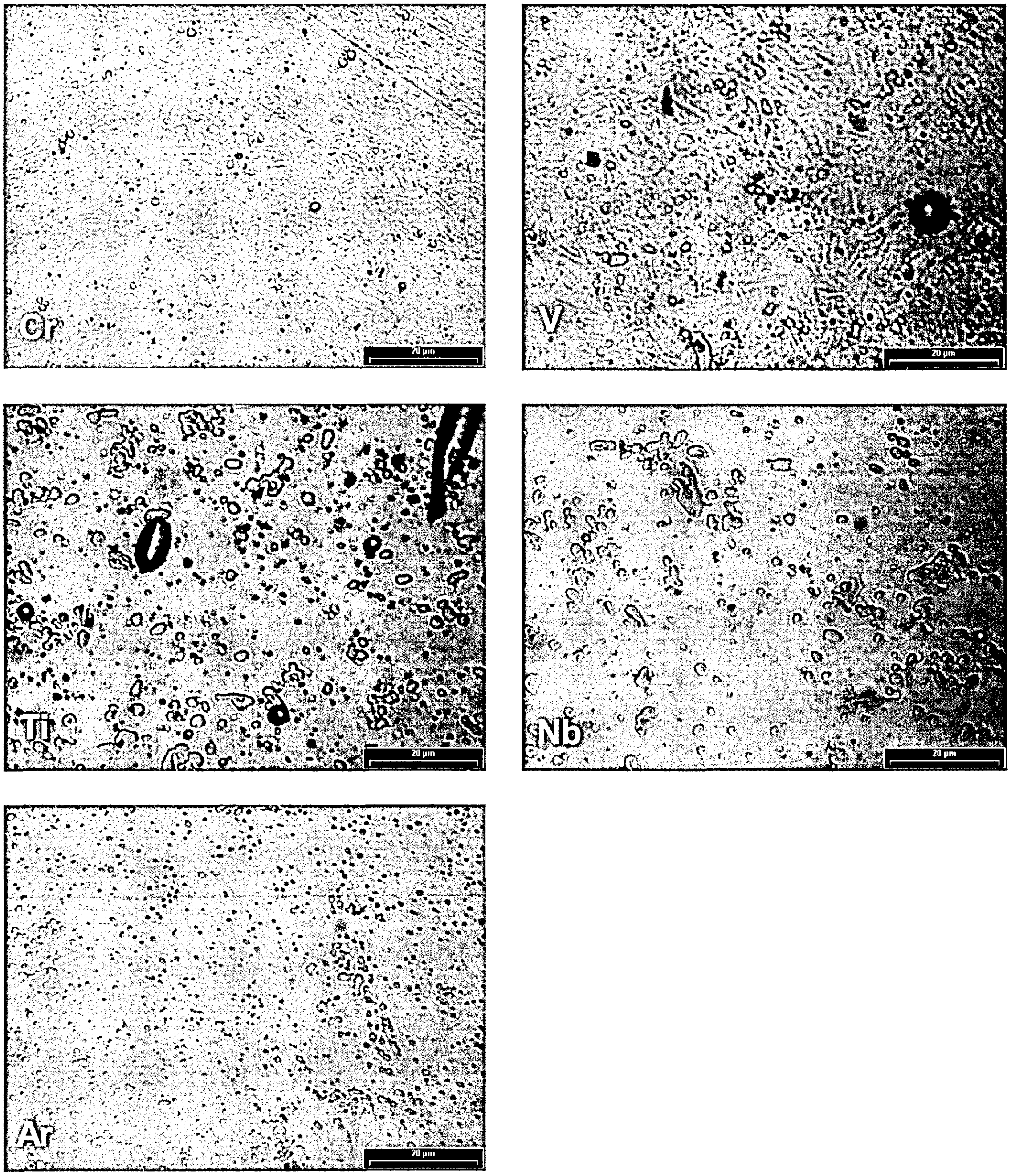

**Figure 4.9:** Optical micrographs of HSS, ion bombarded at $U_s$= 1200 V for 20 minutes using: (a) Cr ions, (b) V ions, (c) Ti ions, (d) Nb ions, and (e) Ar ions.

## Ion bombardment induced changes in microstructure

All metal ion bombarded low carbon steel specimens show a 5 to 8 nm thick modified layer as can be seen from Figures 4.10a-d. The BF images do not exhibit significant differences in the microstructure of the substrate surface regions, for samples subjected to either Cr-, Nb- or V-ion bombardment ($U_s$= 1200 V, 20 minutes exposure time). In contrast, after Ti-ion bombardment the substrate surface region looks denser and exhibits a sharper boundary compared to all other cases. The same experiments were carried out for stainless steel substrates. These interfaces are shown in Figure 4.11. A comparison between low carbon steel (Figure 4.10) and stainless steel substrates (Figure 4.11) shows no significant differences between the two substrate materials when they were V-, Ti- or Cr-ion bombarded. In contrast, the modified layer in the low carbon steel subjected to Nb-ion bombardment is more diffuse than the one observed on the stainless steel substrate. In addition, in the latter case the structure of the modified layer appears to be much finer, comparable to that observed for Ti bombarded low carbon or stainless steel. Evidence of a very fine grained, nearly amorphous microstructure in a similar layer obtained by Nb-ion bombardment at $U_s$= 800 V of a stainless steel substrate is shown in the *micro-diffraction pattern* in Figure 4.12. Figure 4.12a is a micro-diffraction pattern taken from the very fine grained layer on the thinnest region of the cross-sectional TEM specimen. Despite the small probe size of 1 nm a ring pattern is obtained, where the single spots can be distinguished. Figure 4.12b shows the pattern obtained from a slightly thicker region of the TEM specimen. All spots are merged to form a closed circle. In contrast, it can be seen that the modified layer in the low carbon steel obtained by Cr-ion bombardment remains crystalline as evident from Figure 4.13. Here, a BF image was overlaid with the corresponding DF image. The images were aligned using a grain boundary as a marker. The modified steel expressed by the dark ribbon in the BF image appears, like the rest of the substrate grain, bright in the DF image. It does not remain bright when the sample is tilted. Thus, the modified layer is crystalline and has the same crystallographic orientation as the unmodified substrate grain.

TiAlN

TiAlN

TiAlN

TiAlN

**Figure 4.10:** Cross-sectional TEM images taken from ion bombarded low carbon steel (*Us* = 1200 V for 20 minutes) using: (a) Cr ions, (b) Nb ions, (c) Ti ions, and (d) V ions.

TiAlN

20nm

TiAlN

20nm

**Figure 4.11:** Cross-sectional TEM images taken from ion bombarded stainless steel (*Us* = 1200 V for 20 minutes) using: (a) Cr ions, (b) Nb ions, (c) Ti ions, and (d) V ions.

**Figure 4.12:** Micro-diffraction pattern (lnm probe size) of interface layer found at stainless steel bombarded with Nb ions at *Us* = 800V for 12 minutes: (a) taken of thinnest region of XTEM specimen (b) taken of thicker region of XTEM specimen.

**Figure 4.13:** Cross-sectional TEM images taken from Cr-ion etched low carbon steel bright and DF images are partially overlaid.

## Ion bombardment induced changes in microchemistry

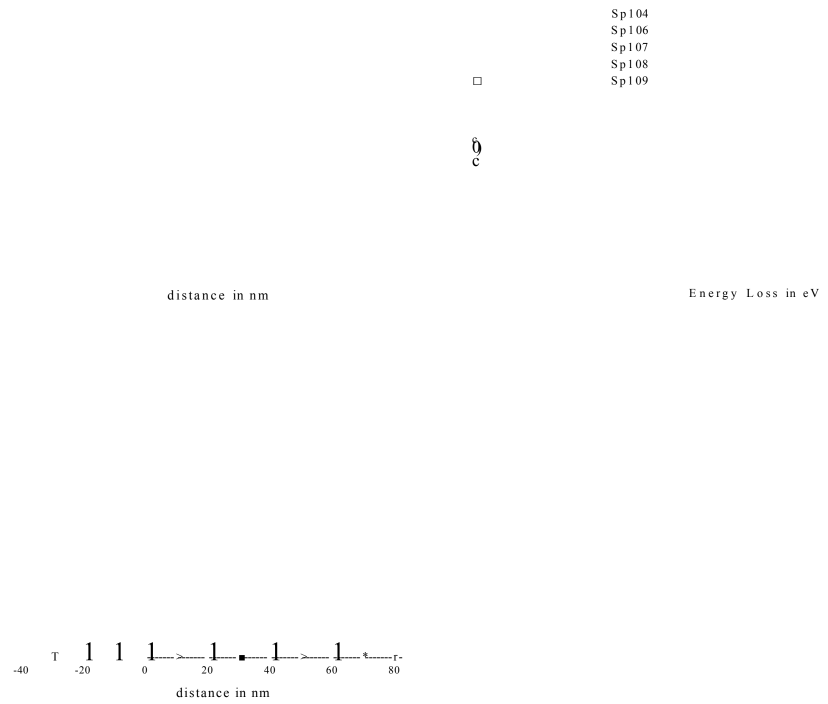

**Figure 4.14:** Ar-ion bombarded low carbon steel [$U_s$= 1200 V, 20 minutes exposure): (a) STEM-EDX profile, (b) EELS profile, (c) oxygen edge of EELS spectra used for quantification, and (d) STEM BF image correlating spectra and locations at the specimen.

Figure 4.14 summarises the elemental composition of a low carbon steel/TiAIN interface obtained by Ar-ion bombardment. A STEM-EDX profile across this interface is presented in Figure 4.14a. Ar accumulation with a maximum concentration of 5at% is observed at the interface. Figure 4.14b shows an EELS-profile that was taken in order to investigate the oxygen distribution. A significant increase of the oxygen level was found at the interface. The oxygen edge of the EELS spectra used for quantification are given in Figure 4.14c. Here, the increased oxygen concentration is expressed by a significantly larger peak area in spectrum 107 compared to the peak area in spectrum 104. Spectrum 107 was taken directly from the interface as can be seen from Figure 4.14d. Spectrum 104 gives a reference value for the oxygen edge obtained from the TiAlN coating. Furthermore, a change in peak shape is observed. A reference spectrum for $Fe_2O_3$ is represented by the grey trace in Figure 4.14c. It exhibits a double peak with maxima at 532 eV and 541 eV. The double peak is also present in EELS spectra 108 and 109 both taken from the steel. In contrast spectra taken from the coating show typically only a maximum at 541 eV. Spectrum 107 exhibits only a pronounced shoulder at the position of 533 eV in addition to the peak at 541 eV.

Ar accumulation at the interface with a comparable maximum concentration is also found in case of metal ion bombardment as can be seen from Figures 4.15 and 4.16. Figure 4.15 summarises the STEM-EDX profiles across hard coating-low carbon steel interfaces obtained by Cr-, V-, Ti- and Nb-ion bombardment, respectively. Corresponding profiles for hard coating-stainless steel interfaces are presented in Figure 4.16. Typical for all STEM-EDX profiles is an enrichment of the bombarding species in the iron rich region with maximum concentrations between 30 at% and 40 at% extending about 8 nm to 13 nm into the steel. In addition, in case of the Nb-ion bombarded low carbon steel the accumulation of the bombarding species extends beyond the iron rich region towards the coating. The same effect but more pronounced is observed on the stainless steel surface. Here, the maximum Nb concentration is found on top of the steel surface. Ti-ion bombardment of stainless steel results in a similar element distribution. However, the situation is less clear since Ti is also present in the coating. To separate the Ti accumulated during Ti-ion bombardment and Ti present in the coating it was assumed that the Al and Ti ratio was constant with Al having a slightly higher concentration of 54 at% compared to Ti with 46 at%. Therefore, the difference $c_{Ti} - c_{Al}$ plotted in Figures 4.15 and 4.16 should represent the amount of Ti caused by Ti-ion bombardment.

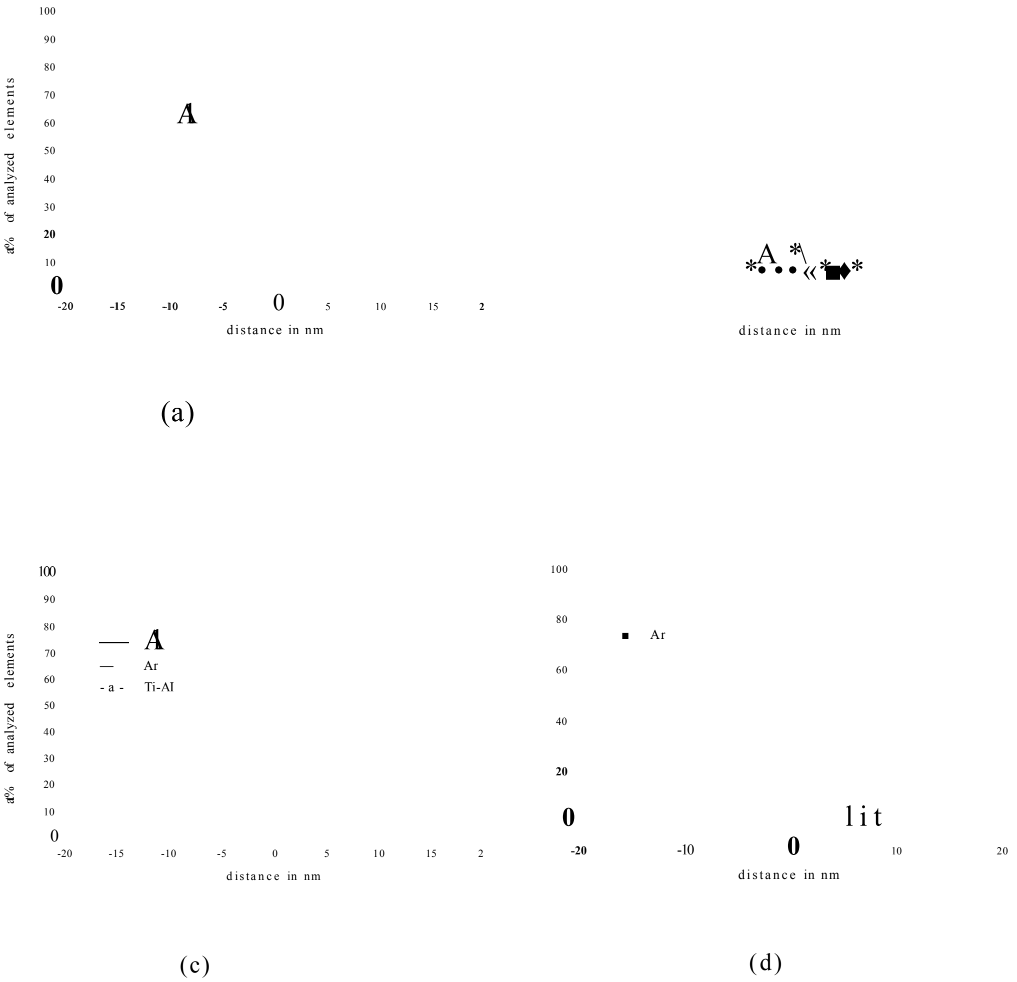

(a)

(c)

(d)

**Figure 4.15:** STEM-EDX Profiles of hard coating-low carbon steel interfaces generated by metal ion bombardment at *Us* = 1200 V, 20 minutes exposure using: (a) Cr ions, (b) V ions, (c) Ti ions, and (d) Nb ions.

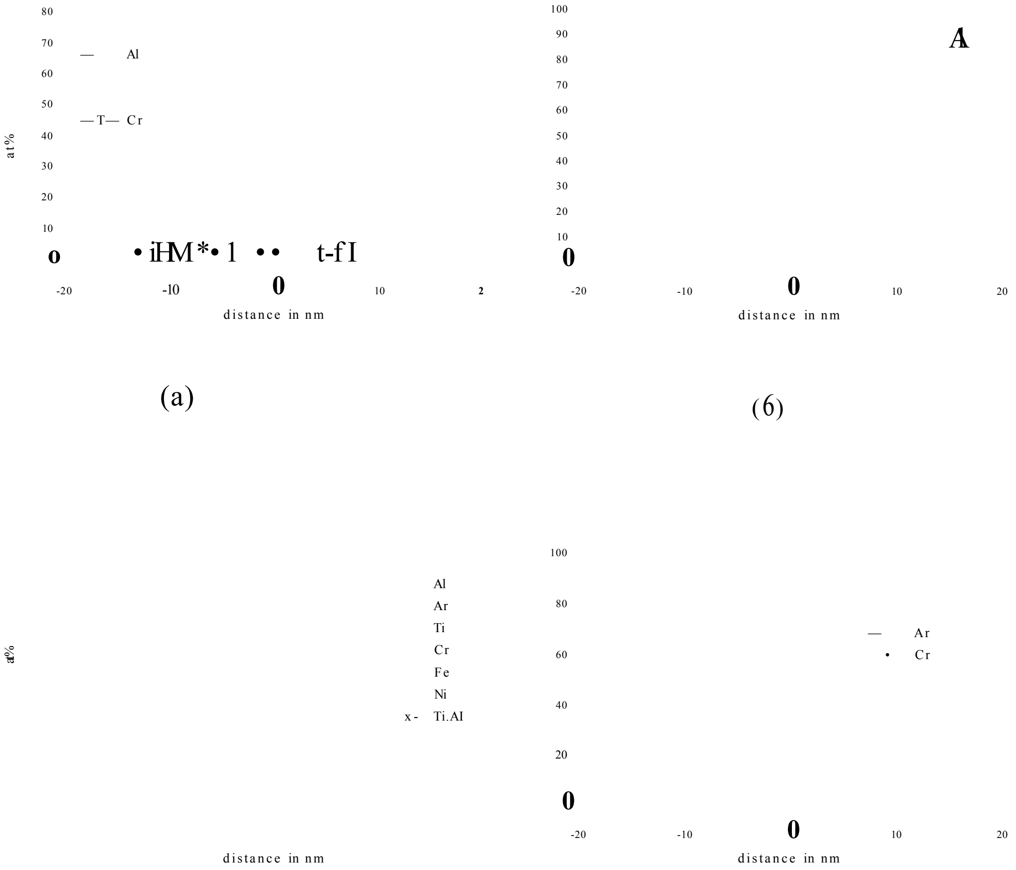

(a)

(6)

(c)

(d)

**Figure 4.16:** STEM-EDX Profiles of hard coating-stainless steel interfaces generated by metal ion bombardment *Us* = 1200 V, 20 minutes exposure using: (a) Cr ions, (b) V ions, (c) Ti ions, and (d) Nb ions.

### 4.2.3 Influence of Cr-ion energy

#### Ion bombardment induced topography changes

Figure 4.17 shows low carbon steel surfaces, which were exposed to Cr-ion bombardment at different bias voltages but at a constant exposure time of twenty minutes. Figure 4.17(a) taken from the centre of a low carbon steel sample after Cr-ion bombardment at $U_s$= 1000 V, shows no feature that could be related to grain boundaries or structure within the grains. An image taken from the same sample but close to the edge of the specimen is presented in Figure 4.17(b). Here, grain boundaries are clearly visible as it was the case for the higher bias voltage $U_s$= 1200 V (see Figure 4.4). In general, a reduction of the bias voltage during Cr-ion bombardment to

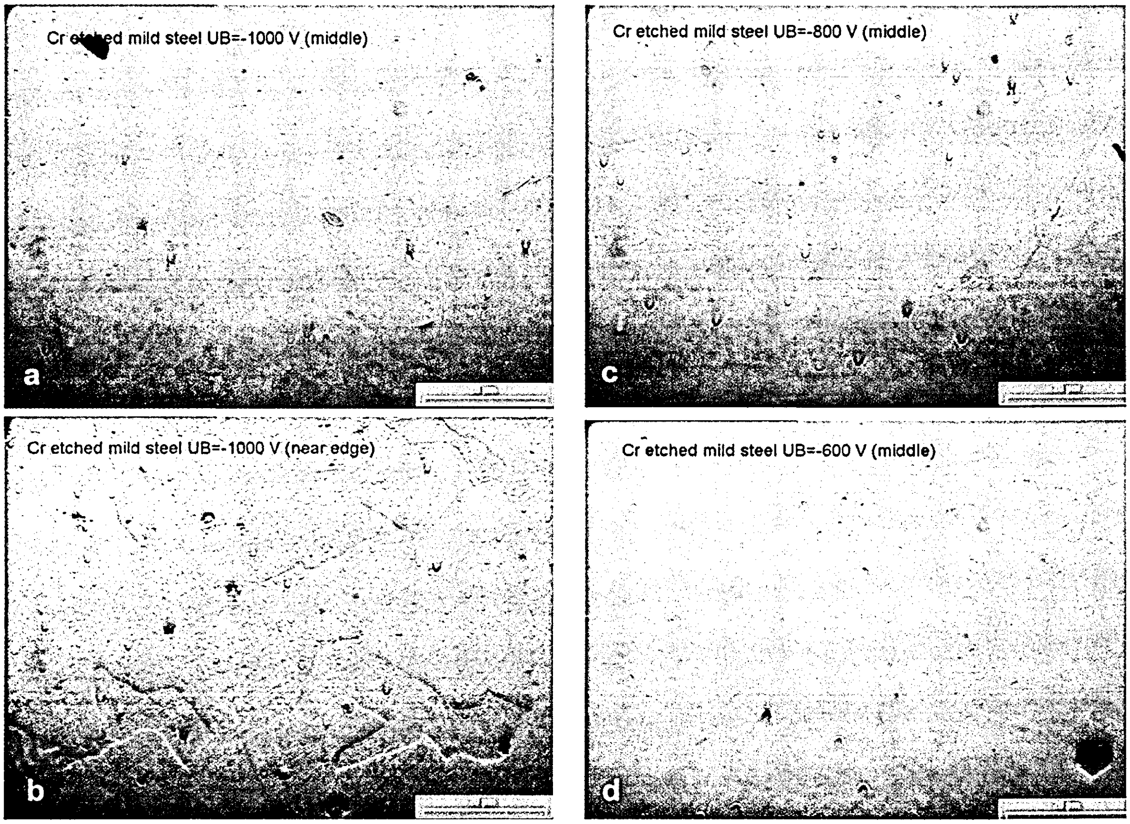

**Figure 4.17:** Optical micrographs of low carbon steel exposed to Cr ions for 20 minutes: (a) $U_s$= 1000 V, image taken from centre of sample (b) $U_s$= 1000 V, image taken near edge of sample, (c) $U_s$= 800 V (centre), and (d) $U_s$= 600 V (centre).

$U_s \leq 1200$ V does not give rise to apparent etch effects in the centre region of the treated samples as evident from Figures 4.17(c) and (d) which represent surfaces after Cr-ion bombardment at $U_s = 800$ V and $U_s = 600$ V, respectively. Only one grain in Figure 4.17(c) is distinctive and exhibits a lamellar structure.

### Substrate material removal rate

To quantify the observations made by light microscopy the efficiency of material removal was judged by step height measurements. The results are shown in Figure 4.18a. Two sets of data are presented both giving evidence for a reduced removal rate at lower bias voltages and no measurable etching effect at $U_s = 400$ V. However, the estimated etch rate differs when the step height was measured by two different techniques showing the limitations of the method. An additional data point was included to demonstrate the time independence of the etch rate in case of $U_s = 1200$ V. XTEM imaging (Figure 4.18b) corroborates the results given in Figure 4.18a for $U_s = 1200$ V. A droplet was deposited during the 20 minutes Cr-ion bombardment, presumably at an early stage so that a pronounced step was generated between the area protected by the droplet from further ion bombardment and the region exposed to ion bombardment during the entire process. Since the arrival time of the droplet is unknown the estimated etch rate of 5 nm/min is a minimum value. Interesting to note is that the region protected by the droplet includes a grain boundary in the substrate. At the same time the step heights on the left and right hand side differ.

### Ion bombardment induced changes in microstructure and microchemistry

The dense microstructure of the interface obtained by Cr-ion bombardment at $U_s = 1200$ V was shown in Figure 4.10a. The interface region visible in this Figure corresponds to a Cr enriched steel (Cr implantation) as it was already evident from Figure 4.15a. Frequently observed however, is a re-crystallisation zone on the surface of the low carbon steel with the smallest grains at the surface and an increased grain size towards the bulk substrate material (Figure 4.19).

When the bias voltage is decreased by only 200 V to $U_s = 1000$ V indications

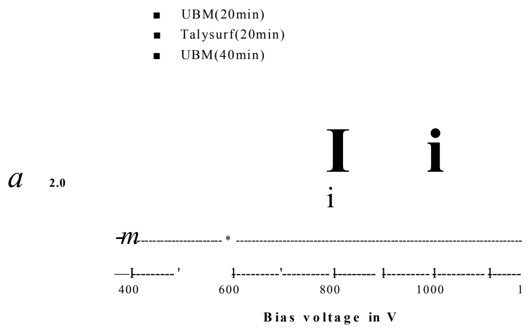

Figure 4.18: Etch rate determination for Cr-ion bombarded steel surfaces: (a) Influence of bias voltage on etch rate estimated from step height measurements and (b) evidence for removal of « 100 nm of low carbon steel corresponding to an etch rate 5 nm/min by XTEM imaging.

for the formation of a deposition layer are found. This is expressed by the high maximum concentration approaching nearly 70 at% of Cr located between substrate and coating (Figure 4.20). An indication for the presence of two separate regions contributing to the Cr profile is given by the shoulder visible in the Cr profile. The region reaching its maximum concentration within the Fe rich region is consistent with an implantation profile. In contrast to the dense interface found for *Us*= 1200 V, Cr-ion pre-treatment at *Us*= 600 V leads, at least locally, to the formation of a low density interface layer as can be seen in Figure 4.21a. The thickness of the interface layer varies as can be seen by comparison of the layer thickness in the regions labelled with 1 and 2, respectively in Figure 4.21b. It is interesting to note the correlation between thickness variation and grain boundaries in the underlying low carbon steel substrate in Figure 4.21b. STEM-EDX profiles across the interface region taken from two different areas of the same sample Cr ion bombarded at *Us*= 600 V exhibit significant differences in the Cr distribution as demonstrated for two selected cases.

**0.90 pm**

**Figure 4.19:** Low magnification XTEM showing a re-crystallization zone in the low carbon steel substrate surface found after 20 minutes exposure to *Us* = 1200 V ion bombardment.

The profile in Figure 4.22a, taken from region 1 in Figure 4.21b, shows a pronounced Cr deposition layer with a thickness of about 10 nm. The width of the Cr/Fe interface is approximately two times broader than the Cr/coating interface. The Cr film is deposited with concurrent energetic ion irradiation, thus the Cr profile gives evidence of a limited mixing and implantation in the substrate. A relatively high Ar level with a maximum concentration of 6 at% within the deposited Cr layer was detected. It is reasonable to assume that the Ar resides predominantly in the less dense regions, evident in Figure 4.21a. A STEM-EDX profile taken from region 2 in Figure 4.21b is presented in Figure 4.22b. The Cr distribution, in agreement with the BF image, shows that the modified layer thickness is « 5nm, i.e. a factor of two smaller than in region 1.

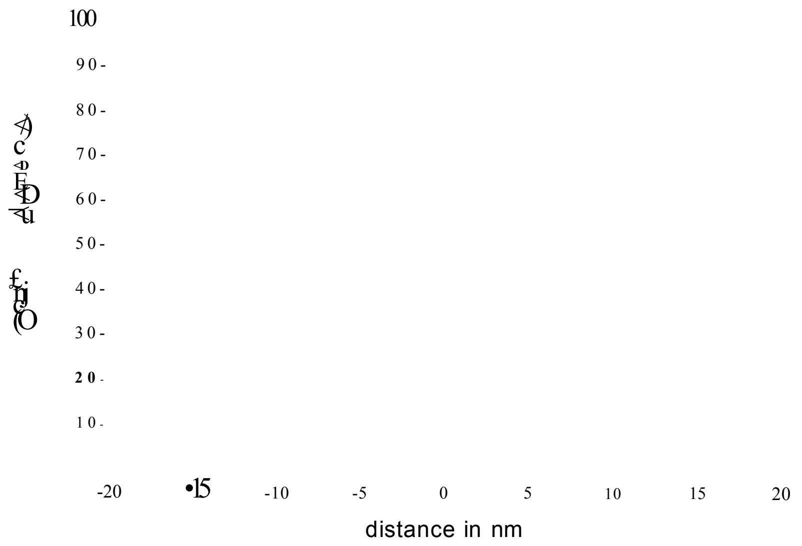

**Figure 4.20:** STEM-EDX profile of Cr-ion bombarded low carbon steel *Us*= 1000 V, 20 minutes exposure.

**Figure 4.21:** XTEM images of interfaces obtained by Cr-ion bombardment at *Us*= 600 V (a) under focused low magnification image exhibiting low density regions (bright spots in dark ribbon) within interface layer and (b) higher magnification showing the thickness variation of the interface layer, which is correlated to substrate grain boundaries.

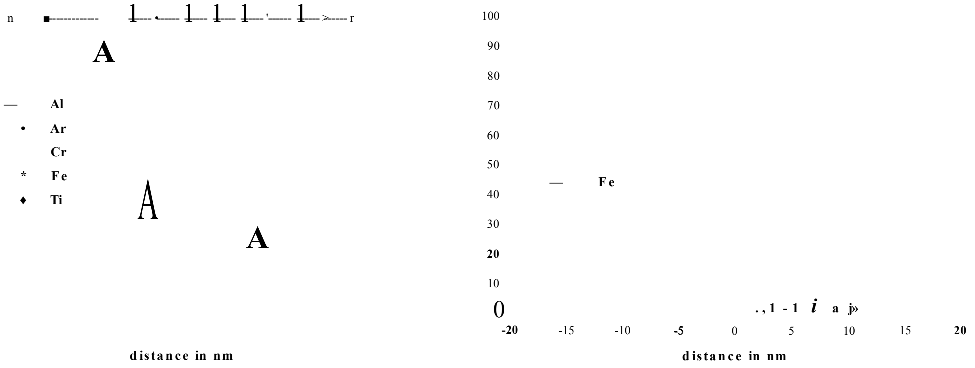

(a) *(b)*

**Figure 4.22:** STEM-EDX Profiles of TiAlN-low carbon steel interfaces generated by Cr-ion bombardment at £/s=600F, 20 minutes exposure: (a) taken from region 1 in Figure 4.21b and (b) taken from region 2 in Figure 4.21b.

Cr accumulation at the interface in form of a deposition layer in case of Cr-ion bombardment at *Us*< 1000 V is also evident from XRD traces in Figure 4.23 collected from Cr-ion bombarded stainless steel surfaces in a glancing angle geometry. Figure 4.23a shows the (111) stainless steel peak at 20 = 43.8°. This is the only visible peak in case of the stainless steel substrate subjected to Cr-ion bombardment at *U*s=1200 V. By reducing *Us* to 1000 V a shoulder becomes visible. With further reduction in *Us* to *Us*=600 V a second peak at 20 = 44.5° corresponding to the (110) Cr reflection can be clearly distinguished. The intensity of that peak increases with a decrease in *Us* to 400V such that it overlaps with the stainless steel (111) peak. In the latter case two additional intense peaks are found in the XRD trace at 20 = 64.6° and 20 = 81.8°. Figure 4.23b shows the latter peak.

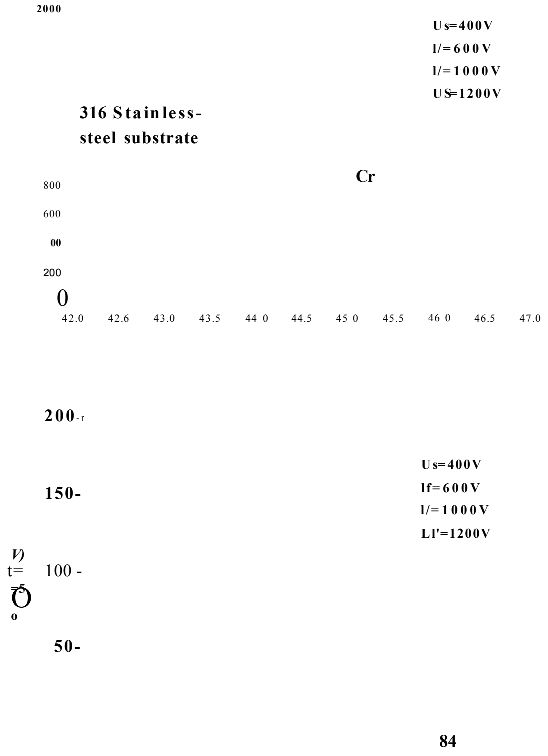

**Figure 4.23:** Glancing angle XRD traces of Cr-ion bombarded stainless steel (400 V <*US*< 1200 V): (a) 42° < 20 < 47° showing the (111) stainless steel peak and an additional peak at lower *Us,* (b) 80° < 20 < 85°: a peak at 20 = 81.8° is only found for £/s=400 *V.*

## 4.2.4 Influence of exposure time to Cr-ion bombardment

### Ion bombardment induced topography changes

Figure 4.24 demonstrates how the structure modification varies with exposure time on the example of Cr-ion bombarded low carbon steel (f/s=1200 *V).* In spite of the fact that grain boundaries are visible after only 10 minutes exposure (Figure 4.24b) the surface of all grains remains smooth in contrast to the rough surface observed in some grains after Cr-ion bombardment for 20 minutes in Figure 4.24a. For the shortest exposure time of 5minutes atypical surface is presented in Figure 4.24c. In thatcase grain boundaries ofthe steel canbe hardly recognised. Figure 4.24 also demonstrates the reduced amount of droplets at the substrate surface for shorter exposure times[2].

---

[2] Dark spots in Figure 4.24 correspond to non-metallic inclusions (compare Figure 4.2) and should be not mistaken as droplet related growth defects.

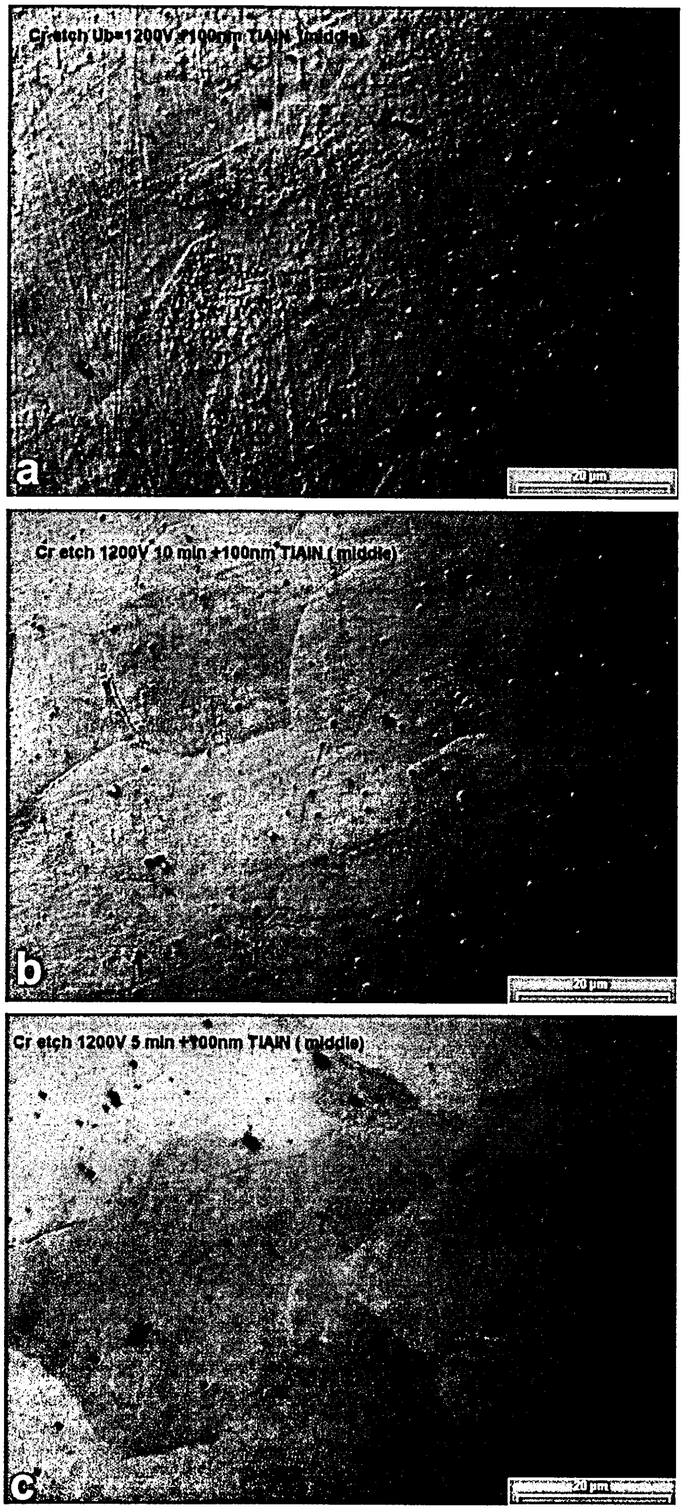

**Figure 4.24:** Optical micrographs of low carbon steel exposed to Cr ions at $U_s$=1200 $V$ for: (a) 20 minutes, (b) 10 minutes, and (c) 5 minutes.

### Ion bombardment induced changes in microchemistry

Figure 4.25 a and b show the elemental profiles for low carbon steel samples exposed to Cr-ion bombardment at *U*s= 1200 C for ten and five minutes, respectively to be compared with Figure 4.10a for a twenty minutes exposure. In all three cases pure implantation profiles are observed where Cr can be detected in a depth of up to 13 nm. An apparent maximum Cr concentration (deviation from true concentration due to limited lateral resolution) between 27 at% and 37 at% is observed in all three cases. Although the dose was varied about a factor four the integrated Cr profiles (5 minutes: 250±41at%nm, 10 minutes: 216±34at%nm, 20 minutes: 264±4at%nm) do not show any significant changes in Cr content.

0) 60 -

distance in nm

distance in nm

(a)

(&)

**Figure 4.25:** STEM-EDX profiles of TiAlN-low carbon steel interfaces generated by Cr-ion bombardment at £/s=1200 *V* for (a) 10 minutes and (b) 5 minutes.

## 4.2.5 Influence of Ar pressure during Cr-ion bombardment

### Material removal rate

Although mainly metal ions are used for sputter cleaning Ar ions can be present due to ionisation in the cathode spot and charge exchange events in the plasma (Ar is required for a stable arc discharge [3] ). The influence of Ar pressure on the etch rate is shown in Figure 4.26. The material removal rate is doubled when an Ar pressure of $p_{Ar} = 9 \times 10^{-2}$ Pa is used compared to the pure Cr arc discharge at base pressure.

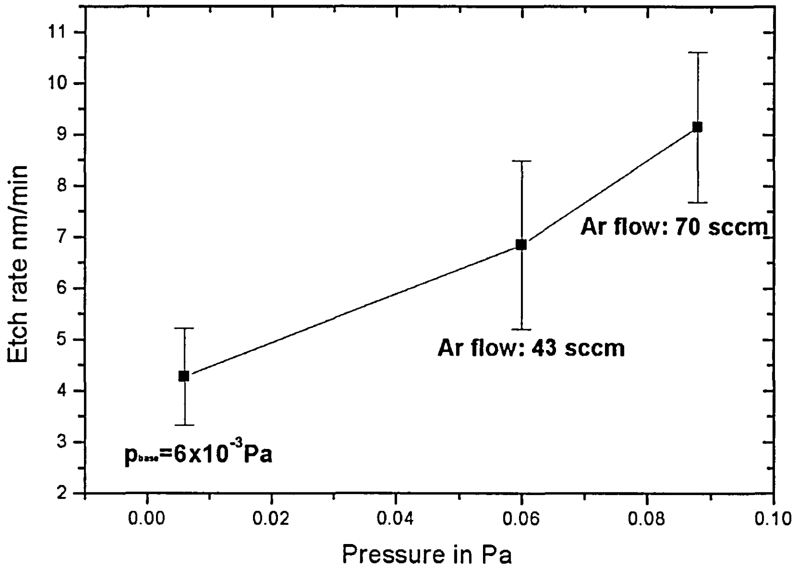

**Figure 4.26:** Influence of Ar pressure on etch rate.

### Ion bombardment induced changes in microchemistry

STEM-EDX profiles are not available for pure Cr-ion bombardment or sputter cleaning at $p_{Ar} = 0.09$ Pa. Instead interfaces generated by mixed Cr/Ar-ion bombardment at $p_{Ar} = 6 \times 10^{-2}$ Pa and mixed Cr/Ar-ion bombardment at $p_{Ar} = 9 \times 10^{-2}$ Pa followed by pure Cr-ion bombardment are compared. STEM-EDX profiles of these two interfaces are shown in Figure 4.27a and b, respectively. An apparent maximum Cr concentration of about 37 at% is observed for both interfaces. However, the shape of the implantation profiles exhibit significant differences. A sharp maximum is observed in Figure 4.27a, which represents a profile taken from the interface generated by a ten minute mixed Cr/Ar-ion bombardment. In contrast, the Cr profile

---

[3] This is due to the large sized, rectangular cathodes (60 cm x 19 cm). After a running in phase for most cathode materials the discharge is stable without additional gas support.

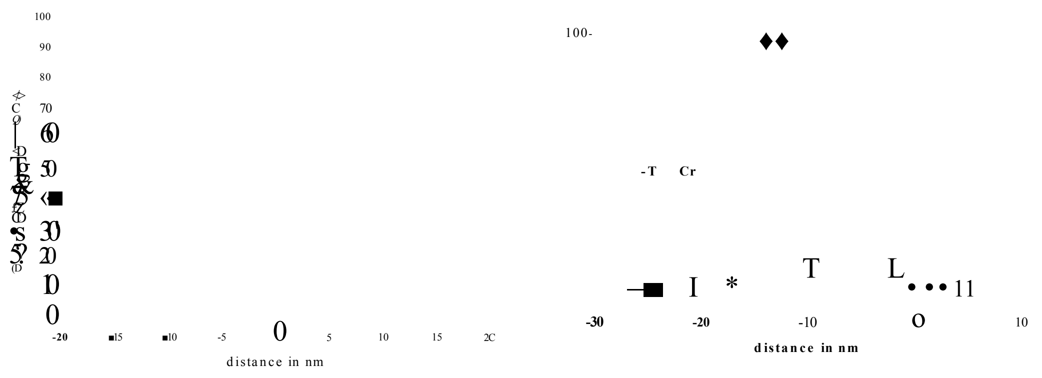

(a) (6)

Figure 4.27: STEM-EDX profiles of TiAlN-low carbon steel interfaces generated (a) by mixed Cr/Ar-ion bombardment at *PAT* = 6 x 10-2 Pa for 10 minutes, *U*s= 1200 *V* and (b) by mixed Cr/Ar-ion bombardment at ***PAr*** = 9 x 10-2 Pa for 8 minutes followed by a pure Cr-ion bombardment for 2 minutes.

corresponding to the two stage process comprising a pure Cr bombardment as final step exhibits a Cr plateau extending over 4.5 nm into the steel at this maximum concentration (Figure 4.27b). In addition, a deeper penetration of Cr into the steel was observed in the latter case. A significant Cr peak was detected as deep as 20 nm in the steel substrate whereas in Figure 4.27a Cr could only be found up to a depth of 13 nm. Both indicates a more efficient implantation effect when a pure Cr-ion bombardment is involved. This is also reflected by the integrated peak areas of 368 ± 27 at%nm of which 95 % corresponds to Cr found to a depth up to 13 nm for the two step process compared to 216 ± 34at%nm for a ten minute Cr-ion bombardment at *PAT*— 6 x 10~2 Pa.

### 4.2.6 Influence of arc current used for Cr-ion bombardment

Figure 4.28a shows the elemental composition across the interface when the arc current *IA* was decreased to 80 A in comparison to Figure 4.15a where it was 100 A.

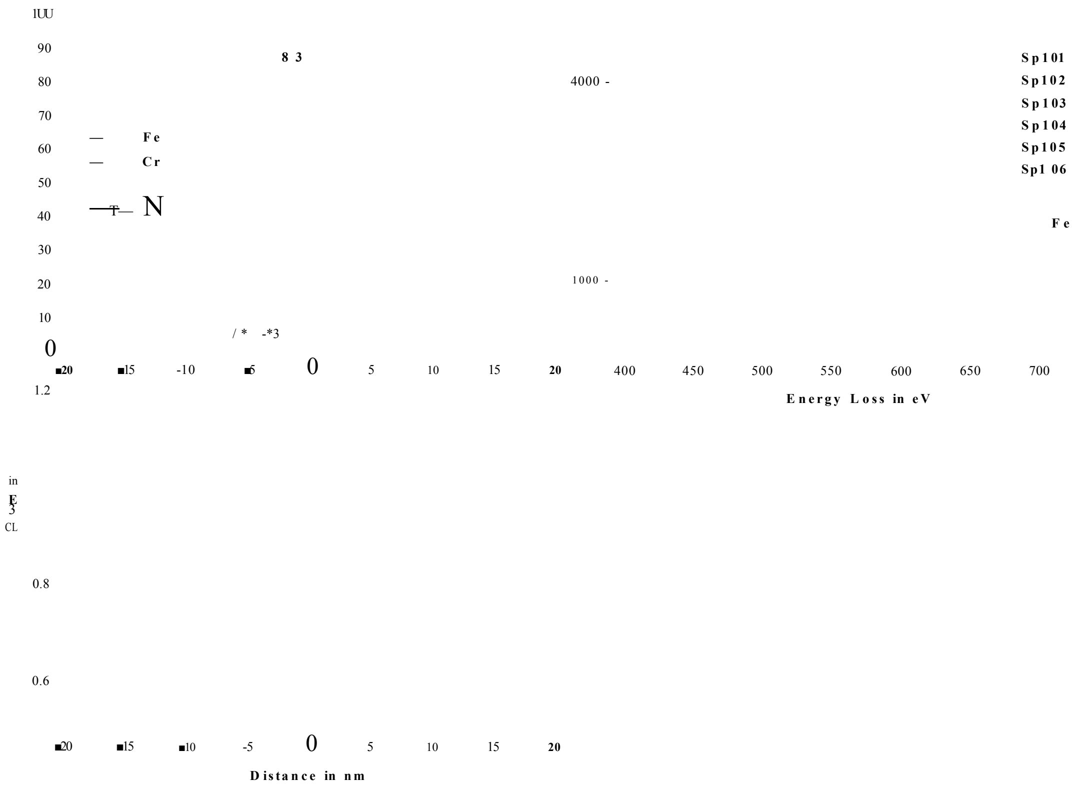

**Figure 4.28:** Cr-ion bombarded low carbon steel *IA* = 80 A, [A=1200 *V,* 20 minutes exposure time: (a) STEM-EELS profile across interface, (b) EELS spectra used for quantification, and (c) sample thickness in mean free path units as estimated form zero loss peak and low loss region of EELS spectra.

For both processes the same bias voltage *Us* = 1200 V, exposure time (20minutes) and gas pressure *pAr*= 0.06 Pa were used. Both profiles have similar shapes within the iron rich region. However, in case of the *I^*= 80 A sample some Cr deposition is also found on top of the substrate surface (data points 102 and 103 in Figure 4.28a) however, in a much lower concentration than for example in Figure 4.20. In the latter case the arc current was 100 A but using *Us*= 1000 V lead to the formation of a much more pronounced deposition layer. Figure 4.28b shows some of the EELS spectra, which were quantified in order to plot the elemental profiles in Figure 4.28a. Spectra 102 and 103 in Figure 4.28b correspond to the region with high Cr concentration on top of the substrate surface. It is interesting to note that these two spectra exhibit pronounced oxygen peaks in contrast to all other spectra. This could be caused by oxides being present on both surfaces of the TEM cross-section in conjunction with large thickness variations of the cross-section. Consequently, the thickness of the TEM cross-section in units of mean free path is given in Figure 4.28c. Within the error the thickness in the analysed area is uniform.

## 4.3 Discussion

### 4.3.1 Influence of ion species

#### Ion bombardment induced topography changes

When the ion flux approaches $10^{19}\,\mathrm{ion/cm^2}$ the development of surface structures on crystalline solids is observed. In polycrystalline targets (as it is the case here) the stochastic orientation of the grains causes discontinuities in erosion speed at the grain boundaries. These discontinuities are likely to induce surface structures such as ridges [106]. Since the flux in the experiments described in Section 4.2.2 was of the order of $10^{19}\,\mathrm{ion/cm^2}$ or higher the presence of ridges at the grain boundaries as found in Figures 4.6 and 4.7 is expected. In addition to that, the development of characteristic structures within the individual single-crystalline grains is typical [106] as it was shown on the nanometre scale by AFM imaging in Figure 4.7 and on the micron scale by optical micrographs such as Figures 4.5, 4.8a,b and 4.9a,b. That there are no such features found for Nb and Ti-ion bombardment of stainless steel and high-speed steel surfaces (Figures 4.8c,d and 4.8c,d ) could be explained either by less material removal or by the presence of an amorphised surface layer. Although ion bombardment of non directionally bonded materials such as a metal substrates usually causes self annealing with no residual damage or can retain point defects or dislocations [38] amorphisation of metals due to ion implantation was observed elsewhere. For example Ti implantation into copper was reported to lead to amorphisation in the alloyed surface layer [107]. An amorphous FeTi component was also detected by Mössbauer spectroscopy on Ti-ion bombarded low carbon steel surfaces. In addition to the amorphous component (1.7 % of relative spectral area) a crystalline TiFe component (0.8 % of relative spectral area) was observed [108]. In that context it seems to be worth noting that an amorphous $FeTi_{1-x}$ phase was also found by conversion electron Mössbauer spectroscopy when deposited Ti was intermixed with a previously argon ion etched iron substrate [109]. The proportion of this phase is reported to increase with increased bias voltage employed during deposition [110].

The differential etching of grain boundaries might be due to a different chemical composition due to segregation of contaminants or solute atoms at the grain boundaries as can be seen in Figure 4.3a.

The featureless surface observed after Nb-ion bombardment of stainless steel and high-speed steel substrates can be explained either by a lower sputtering yield for those substrate materials and/or as result of an amorphised surface layer. For example it was previously shown [97] that $Ti_{0.85}Nb_{0.15}$ ion bombardment of stainless steel lead to the formation of an amorphised layer and was also found in the this study as described in Section 4.2.2.

### Ion bombardment induced changes in microstructure

The modified surface layer visible in the TEM cross-sections in Figures 4.10a,c and d is not likely to arise from atomic mass related electron absorption effects because of the small differences in atomic masses for Fe (56amu), Cr (52amu), Ti (48amu) and V (51amu). It is assumed that the contrast is partially due to local strain fields caused by dislocation cores or defect clusters generated by highly energetic ion impact in case of V and Cr-ion bombardment for which it was shown on the example of Cr-ion bombardment that the layer remains crystalline (Figure 4.13). The layer observed at the Ti-ion bombarded low carbon steel (Figure 4.10c) appears to be much denser than all the other layers formed by Cr-, Nb- and V-ion bombardment. This could be due to the amorphous nature of that layer in agreement with the Mössbauer spectroscopic results where the amorphous TiFe spectral component had double the value of the relative spectral area of the crystalline TiFe component [108]. In addition a similar dense layer is observed when stainless steel was subject to Nb-ion bombardment (Figure 4.11b), for which it was shown to exhibit a very fine crystalline, nearly amorphous microstructure (Figure 4.12). Usually amorphisation of metals is only observed when certain elemental compositions are reached, which would explain why this effect depends on the substrate composition (compare Figure 4.11b and 4.10b). It was shown by Zhang [111] that even very small compositional changes or the presence of a third element can hinder or promote the formation of an amorphous phase.

### Gas incorporation at the interface

Residual and working gas (Ar) present during ion bombardment was incorporated at the interface. As described in Section 4.2.2 high levels of oxygen were found at the interface when Ar ions were used for substrate sputter cleaning. Similar observations were published previously. For example it was reported in [93] that oxygen was not completely removed by Ar-ion etching for ten minutes when the base pressure of the deposition system was $5 \times 10^{-5}$ Pa. Similarly, it is described in [112] that various oxides are still present at the interface despite substrate cleaning in an Ar plasma at 500°C at a base pressure below $10^{-3}$ Pa. In contrast, the oxide scale was removed by Ar sputter cleaning for thirty minutes (independent of the bias voltage in the range $400\,\mathrm{V} \leq U_s \leq 1000\,\mathrm{V}$) in a system with a base pressure of $10^{-6}$ Pa. Oxygen could not be removed within thirty minutes even at $U_s$= 1000 V in the same system when oxygen was introduced with $p_{O_2}$= $6 \times 10^{-2}$ Pa [113]. Thus, the cleaning effect depends not only on ion flux and sputtering yield but also strongly on the base pressure of the deposition chamber which determines the residual oxygen pressure. Even at a pressure of $10^{-3}$ Pa re-contamination of one mono-layer per second occurs [43]. Therefore, the presence of oxygen at the interface is not surprising since experiments were carried out in this pressure range ($p_{base}$ = $6 \mathrm{x} 10^{-3}$ Pa). The shape of the oxygen peak in the EELS spectrum of the Ar etched low carbon steel in Figure 4.14c, which corresponds to the highest oxygen level corroborates that explanation. The shoulder found at 533 eV in the EELS spectrum 107 indicates the presence of iron oxides but at the same time oxygen incorporated in the coating contributes to the spectrum and the high oxygen level (peak at 541 eV). This in conjunction with the observed evidence for material removal (see Section 4.2.2, Figure 4.5a) suggests a re-contamination of the steel surface. The high oxygen partial pressure is then reduced during the coating step due to a gettering effect by incorporation of oxygen in the coating close to the interface.

This gettering effect can already take place during the substrate sputter cleaning step when instead of inert gas ions highly reactive metal ions are employed and no reactive gas (e.g. $N_2$) is present. In both cases the ions might be implanted at the surface of the negatively biased substrates. However, when metal ions are used those ions, which hit surfaces other than the highly negative biased substrates will condense. Because of the high reactivity of those metals they can react with the residual oxygen thus, lowering the residual oxygen partial pressure. This reduces the risk of re-contamination. In addition to the ions the CA emits metal atoms and macroparticles, which can also serve as getter pump. Although we were not able to demonstrate this effect by masspectrometry performed during the different sputter cleaning procedures, the observation that the pressure in the chamber drops substantially (1 order of magnitude) after metal ion etching for twenty minutes as well as STEM-EELS analysis seem to corroborate this explanation. However, Cr metal ion bombardment at the lower arc current of $I_A$= 80 A, compared to $I_A$= 100 A used in all other experiments, leads even at $U_s$= 1200 V to an increased oxygen concentration at the interface. This can be seen in Figure 4.28b, where the EELS spectra 102 and 103 exhibit pronounced oxygen peaks. In spectrum 102, which has the highest oxygen level the iron peak is hardly discernible whereas the Cr peak is clearly visible. The iron peak is more pronounced in spectrum 103 where less oxygen is found. Thus, oxygen seems to be incorporated into the thin Cr deposition layer. That this is an sample thickness related artifact due to native oxides on the surfaces of the TEM cross-section is rather unlikely because the sample thickness in the investigated area is uniform as described in Section 4.2.6). The incorporation of oxygen in the metal deposition layer demonstrates the getter effect of the highly reactive metal particles. A gettering effect was also reported when a Ti interlayer was deposited prior to the growth of TiN [114], which was shown by secondary-ion mass spectrometry depth profiling. This technique excludes artifacts due to surface oxides, which are possible in the case of cross-sectional analysis [4]. A similar approach (deposition of a metallic interlayer) is frequently reported for example by Gunzman *et al.* [115]. They found Zn film were poorly adherent to the steel substrate, which they attributed to insufficient substrate cleaning by Ar-ion bombardment ($p_{base}< 10^{-4}$ Pa, $Ar^+$ ions from a duoplasmatron-type source, dose $3x10^{16}$ ions/cm$^{-2}$, suitable to erode about 20nm of the (oxide+carbon) contaminated surface layer). They solved the adhesion problem by subsequent deposition of a thin Cr interlayer after Ar-ion etching. Although the interlayer approach can be successful it has limitations compared to metal ion bombardment as further discussed in Section 6.3.1.

Working gas ions (Ar ions) were incorporated at the interface region in all cases when Ar was involved either as bombarding species or as support gas. This was established by STEM-EDX analysis. Since inert gas atoms are only weakly physisorbed on solid surfaces, incorporation of significant concentrations can only occur by trapping of incident energetic species, where the threshold energy for trapping ranges from some ten eV to a few hundred eV depending on the atomic masses of projectile and target [116]. Since the ion energy for pure Ar-ion bombardment with 1.2 keV is well above that threshold energy the presence of Ar at the interface region is not surprising. That trapped Ar is also found in case of metal ion bombardment, where Ar serves as support gas for the arc discharge suggests that Ar atoms are ionised in the plasma. Indeed, this seems to be the case as further discussed in Section 4.3.4. Ar trapping in form of Ar bubbles was previously observed at even lower ion energies ($U_s$= 400 V) during reactive magnetron deposition of TiN in a mixed Ar/$N_2$ atmosphere ([116] and [117]). Ar trapping at the TiN/steel interface was also reported in [96] when Ar ions at $U_s$= 1000 V were used for substrate sputter cleaning for thirty minutes prior to TiN deposition.

---

[4] Although we did find an increased oxygen content at the interface by secondary-neutral mass spectrometry depth profiling the depth resolution of this technique for our samples is, due to the inherent interface roughness, not sufficient to locate the increased oxygen content on a nm scale.

| Cathode material | $\frac{M_{ion}}{M_{Fe}}$ | Mean charge [30] $I_A = 100A$ | Neutrals in % of heavy particles [120] | Sputtering yield(TRIM [121]) Substrate Fe |
|---|---|---|---|---|
| Cr | 0.93 | 2.1 | 0.037 | 2.8 |
| V | 0.91 | 2.1 | 0.37 | 2.8 |
| Ti | 0.86 | 2.1 | 0.042 | 2.8 |
| Nb | 1.64 | 3.0 | 0.0019 | 2.2 |

**Table 4.1:** Cathode material related parameters that influence metal distribution at interface.

### Metal distribution at the interface

The metal distribution found at the interface is a result of four competing effects taking place at the substrate surface. These are: (i) condensation (ii) re-sputtering (iii) implantation and (iv) sputtering of the substrate atoms. Which of those effects dominates depends on the species that are present in the plasma and their energy because these determine condensation rate and sputtering yield, respectively. The degree of ionisation depends on the cathode material. For example the fractional ionisation for Cr is approximately 100% [118] whereas for Ti it is only 80% [118] or as reported elsewhere 68% [119]. In addition, the sputtering yield depends on the mass ratio of impinging ion to target atoms [17]. Furthermore, in spite of the constant bias voltage ($U_s$= 1200V) the energy of the ion is determined by the product of $U_s$ and the charge state of the ions. The charge state distribution for a given arc current (here 100 A) depends on the cathode material. All these effects can contribute to differences in metal distribution at the interface when the substrate was subject to bombardment with different metal ions. Table 4.1 summarises the above mentioned properties for various cathode materials. Considering the sputtering yields given in Table 4.1 it is obvious that no major differences are expected for Cr-, V- and Ti-ion bombardment due to the similarity of atomic mass, which results in the same sputtering yield. For the much heavier Nb ions the calculated sputtering yield is about 20 % lower than for the before mentioned ions. Indeed both, Cr and Ti-ion bombardment of low carbon steel result in pure implantation profiles Figure 4.15a and c, whereas Nb-ion bombardment tends to form a Nb deposition layer (Figure 4.15d). The same tendency but less pronounced is observed for V-ion bombarded low carbon steel (Figure 4.15c) despite similar sputtering yields for Cr and Ti ions. A major difference for V as cathode material lies in the much higher fraction of neutrals considering the heavy particle density (heavy particle: atoms and ions) [120].

When stainless steel was used instead of low carbon steel in all cases except V-ion bombardment the tendency for the formation of a deposition layer was observed. This can not be explained by the different target mass in case of stainless steel in comparison to low carbon steel. However, the different chemical composition may well lead to phase transformations which can results in a change of sputtering yield [122].

### 4.3.2 Influence of ion energy during Cr-ion bombardment

#### Ion bombardment induced topography changes and substrate removal rate

As mentioned previously the absence of structural features within different substrate grains as it was the case for Cr-ion bombardment at $U_s \leq 1000\,\mathrm{V}$ (Figures 4.17a,c and d) either indicates that no material is removed or an amorphous surface layer is formed. The latter situation does not seem to be the case as it becomes evident from Figure 4.17b. It shows again a low carbon steel surface obtained by Cr-ion bombardment at $U_s = 1000\mathrm{V}$. However, here the image was taken very close to the edge of the sample in contrast to Figure 4.17a taken from the centre region of the specimen. In the near edge region the clear visibility of grain boundaries even at $U_s = 1000\,\mathrm{V}$ can be explained by a higher etch rate close to the edge of the specimen due to a stronger electric field caused by the edge geometry. This results in a higher ion to neutral ratio and hence, higher substrate removal rate. Indeed, it was shown by comparing saturation currents measured with cylindrical and flat probe geometry that edges are exposed to a much higher ion flux compared to flat regions of the same specimen [123]. The substrate material removal rate as measured at steps (Figure 4.18a) reflects the trend of a decrease in etch rate with lower bias voltage. It also demonstrates that exposure to Cr-ion bombardment at $U_s \leq 600\,\mathrm{V}$ did not lead to any substrate surface cleaning effects. This is in agreement with the transition from deposition to sputtering in film deposition using a Ti cathodic arc source and applying a substrate bias of $U_s = 600\,\mathrm{V}$ or a Zr cathode and $U_s = 400\,\mathrm{V}$ [124].

In case of Cr-ion bombardment at $U_s = 1200\,\mathrm{V}$ a minimum etch rate on flat surfaces of about 5 nm/min was established by XTEM imaging where a droplet acted as a mask. At the same time the dependence of etch rate on crystal orientation was observed as shown by the variation in step heights measured on two different substrate grains in Figure 4.18a. The dependence of the sputter yield on crystal orientation is due to channelling effects and the difference in binding energy for low and high index planes at the surface [125]. For $\alpha$-Fe, which was exposed to Ar-ion bombardment at $U_s = 600\,\mathrm{V}$ a $10 - 15\,\%$ higher sputtering yield was found for grains with the zone-axes close to [001] compared to regions with the zone-axes close to [111]( see [126]). The dependence of sputtering yield on crystal orientation can also be observed by optical microscopy. An example for that is Figure 4.17c in which only on grain exhibits a lamellar structure whereas the surrounding surface does not show any features indicating material removal.

A further aspect in the choice of cathode material for metal ion etching employing a cathodic arc source is the number of droplets, which are deposited during metal ion bombardment. Those can generate growth defect surrounded by low density regions during UBM deposition [127]. These defects are detrimental when coatings with high oxidation [128] or corrosion resistance [129] are required. From that point of view Ar-ion bombardment seems to be the best choice because it does not causes any growth defects. However, Ar ion bombardment has other limitations as already discussed in Section 4.3.1. All together its results in a worse tool performance than observed for metal ion bombardment, where growth defects can not be completely avoided (see Chapter 6). The micrographs in Figure 4.5 confirm the influence of melting point and vapour pressure on number and size of deposited droplets as reported previously ([4] and [5]).

### Ion bombardment induced changes in microstructure and microchemistry

Substrate material removal rate and chemical composition at the interface are closely related because both are a result of the four competing processes taking place at the substrate surface. As mentioned previously these are (i) condensation (ii) resputtering (iii) implantation and (iv) sputtering of the substrate atoms. The situation is schematically shown in Figure 4.29. Assuming a constant flux of particles (Cr ions, Ar ions and Cr atoms) arriving at the substrate surface the energy of the particle determines if it condenses, becomes implanted or can initiate a collision cascade which either leads to sputtering of condensed atoms or substrate atoms. The sputtering yield $Y_{Cr/Fe}$ for Cr ions impinging on a amorphous Fe surface with an energy of 800 eV (mean charge: $2^+$ and $U_s$= 400 V) was estimated by TRIM [121] to be $Y_{Cr/Fe}$= 1.6 whereas $U_s$ = 1200 V results in $Y_{Cr/Fe}$= 2.8. Furthermore, in the

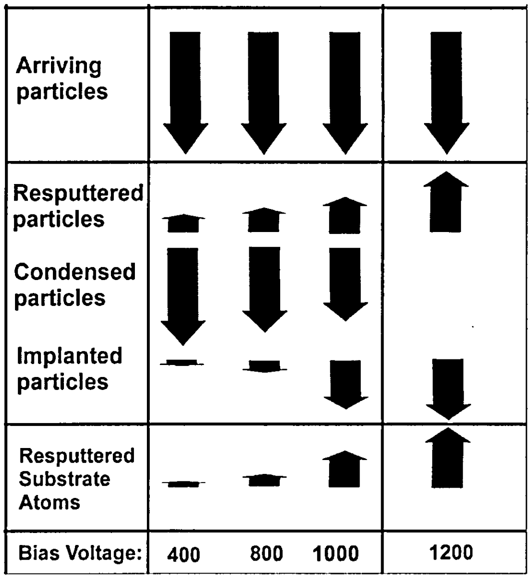

**Figure 4.29:** Schematic drawing of processes involved in surface modification by metal ion bombardment.

| Reflection | 110 | 200 | 211 |
|---|---|---|---|
| $2\Theta in^\circ$ JCPDS [91] for Cr | 44.4 | 64.6 | 81.7 |
| $2\Theta in^\circ$ measured | 44.5 | 64.6 | 81.8 |

**Table 4.2:** Identification of peaks found in glancing angle XRD trace taken from Cr-ion bombarded stainless steel surfaces.

experiments described here Ar was used as support gas. As explained in more detail in Section 4.3.4 Ar is ionised in the plasma such that Ar ions can also contribute to sputtering with $Y_{Ar/Fe}= 1$ for $U_s= 400\,\mathrm{V}$ and at $U_s= 1200\,\mathrm{V}$ $Y_{Ar/Fe}$ reaches 2.5 atoms per ion. The sputtering yields obtained when $U_s= 1200\,\mathrm{V}$ is employed, is sufficient to remove all condensed particles and to cause substantial sputtering of the substrate and therefore, cleaning of the steel surface as described in the previous Section. The Cr enrichment at the interface is mainly in the form of Cr implantation in the steel as seen from the STEM-EDX profile. However, STEM-EDX analysis gives only very localised information and as described before for example crystal orientation effects can be important. That Cr is implanted and no deposition takes place on a larger lateral scale is confirmed by glancing angle XRD. In the XRD trace of the stainless steel, which was exposed to Cr-ion bombardment at $U_s= 1200\,\mathrm{V}$ no other peaks than that of an untreated stainless steel substrate were found. At $U_s= 1000\,\mathrm{V}$ a shoulder at the (111) stainless steel peak was observed, which develops into a separate peak when $U_s\leq 600\,\mathrm{V}$. The position of that peak and the additional peaks found for $U_s= 400\,\mathrm{V}$ matches the values given in the JCPDS [91] data base for Cr as can be seen from Table 4.2. This indicates that in the latter case a pronounced Cr deposition layer is formed whereas at $U_s= 1000\,\mathrm{V}$ the effect is much less pronounced and the deposition layer might be localised. In contrast, the clear Cr peak in the XRD spectrum at $U_s= 600\,\mathrm{V}$ indicates the presence of a higher Cr volume that can be attributed either to a larger covered area or a thicker layer. TEM imaging in combination with STEM-EDX has shown the presence of a continuous Cr layer although the thickness of this layer was not constant as it was shown in Figures 4.21 and 4.22. The thickness variation is again explained by the influence of crystal orientation on sputtering yield and sticking coefficient. The thickness should be correlated to the cleanliness of the metal deposit. When the re-sputtering yield is sufficiently high to remove impurities and contaminants before being buried by newly condensing atoms only a very thin and clean metal deposit is formed.

That the Cr deposition layer is detected by XRD indicates that the Cr deposit has a crystalline character. It should be noted that if the substrate is clean a Cr film (b.c.c) could grow epitaxially on a low carbon steel (b.c.c) substrate. Both materials have the same bravais lattice, where the lattice mismatch is $\approx 0.5\,\%$.

### 4.3.3 Influence of exposure time to Cr-ion bombardment

A short exposure time is desirable for several reasons. The metal removal rate varies with tool geometry with higher rates at sharp edges and therefore, a shorter time will ensure less variation. A reduction in exposure time also leads to fewer droplet related growth defects in the coating (Figure 4.24). In addition one should bear in mind that the rather localised deep erosion track caused by the cathodic arc does not allow a very effective use of the cathode material. However, the cathode/target life in terms of the number of ion etching processes (or cathode/target life per coated tool) could be prolonged by shortening of this process step. Thus, the shortest exposure time which still ensures (i) the removal of all native oxides, (ii) the reduction of oxygen partial pressure to such a level that re-contamination does not occur and (iii) sufficient ion implantation is achieved (as will be discussed in Chapter 6), should be used. The last requirement is fulfilled even by an exposure time as short as five minutes as can be seen by comparing Figures 4.25b (5 minutes) and 4.15a (20 minutes). Both Cr profiles have a similar shape. In both cases the maximum Cr concentration is found at the substrate surface and within the experimental error the same integrated Cr content was measured. This means that the saturation dose is reached, even at an exposure time as short as five minutes [5] . However, in order to meet requirements (i) and (ii) a five minutes exposure is insufficient as will be

---

[5] Saturation dose refers to a steady state of the number of arriving ions and sputtered atoms.

discussed in Section 5.3.3.

### 4.3.4 Influence of Ar pressure during Cr-ion bombardment

#### Material removal rate

It was found that the etching rates of negatively biased ($U_s$= 1200 V) steel substrates more than doubled with the introduction of argon gas to pressures of $\approx$ 0.1 Pa at a constant arc current ($I_A = 100$ A) during a steered Cr arc (see Figure 4.26). Plasma probe measurements indicate that the ion current density at the negatively biased substrates increases significantly with increasing argon pressure, which is attributed to a more efficient volume ionisation processes in the presence of a gas atmosphere and to the ignition of an auxiliary glow discharge at the substrate surface [123].

#### Ion bombardment induced changes in microchemistry

The enhanced Cr implantation effect when a pure arc discharge (no Ar) is used can be explained by a higher number of Cr ions available under this conditions compared to an arc discharge with Ar as support gas. This is due to charge exchange events. When the metal vapour coming from the spot enters the anodic region of the arc discharge, the Cr ions collide with Ar atoms. These collisions are the main reason for Cr re-neutralisation since the process of direct recombination of electrons with metal ions in two-body collisions does not conserve energy and momentum and is therefore unlikely [119]. The ion-atom collisions lead to a charge exchange process of the type: $Cr^{(n)+} + Ar \rightarrow Cr^{(n-1)+} + Ar^{+}$whereby the mean charge state can alter ([130],[131] and [132]). It was shown by optical emission spectroscopy that when the Ar pressure is increased the concentration of $Cr^{1+}$ and $Cr^{2+}$ ions decreases continuously. At the same time the overall ion current densities increase (*Langmuir probe* measurements), however, which indicates that this increase is largely due to Ar ions [123]. This means that the number of Ar ions is increased at the expense of metal ions. This, and the fact that Ar ions will increase the sputtering rate without contributing to metal ion implantation reduce the metal implantation effect when Ar is used as support gas. In addition, the presence of ionised Ar can lead to incorporation of Ar ions in form of gas bubbles in the interface region (see Section 4.3.1). It can be assumed that a subsequent pure metal ion bombardment can reduce the amount of Ar bubbles by sputtering the Ar containing surface layer [6] .

### 4.3.5 Influence of arc current used for Cr-ion bombardment

The arc current was lowered in order to reduce the size and concentration of droplets emitted from the arc source [24]. On the other hand the charge distribution is also a function of the arc current. A reduction of the number of ions with higher charge states was observed for lower arc currents [133]. A consequence of this is a lower material removal rate due to the lower sputtering yield of less energetic particles. Thus, to find first indications for the beginning formation of a Cr deposition layer even at a bias voltage of $U_s$= 1200 V was not unexpected. The high oxygen concentration found in that region is thought to be an indication that metal ion etching provides a clean substrate surface by avoiding re-contamination of sputter cleaned surfaces due to a gettering effect. This was already discussed in Section 4.3.1.

## 4.4 Summary

The influence of various ion bombardment procedures on the microstructure and microchemistry of steel surfaces was investigated. The observed surface conditions after ion bombardment can be classified as follows:

- Surface with surface oxides obtained by Ar-ion bombardment,
- Surface with only locally removed oxides and/ or (localised) metal deposit observed after Cr-ion bombardment at $U_s$< 1200 V or at $U_s$= 1200 V, 5 minutes exposure,

---

[6] For some crystallographic orientation channelling may occur, which leads to deeper penetration than the calculated projected range (TRIM) of about 1.5nm of Ar in Fe and hence could cause incomplete removal of Ar for short pure metal ion bombardment (removal rate 4nm/min).

- Amorphised surface layer found after Ti or Nb-ion bombardment and,
- Clean metal surface with preserved crystalline order achieved by Cr-ion bombardment at $U_s$= 1200 V for 20 minutes at $p_{Ar}$= $6 \times 10^{-2}$ Pa or in two steps with overall duration of 10 minutes: 8 minutes $p_{Ar}$= $9 \times 10^{-2}$ Pa followed by 2 minutes $p_{base}$.

Metal ion bombardment provides a clean surface by avoiding re-contamination of freshly sputtered surfaces in contrast to Ar-ion bombardment. This is thought to be due to a gettering effect achieved during metal ion bombardment. Furthermore, it was found that metal ion bombardment in an Ar atmosphere leads in fact to a mixed Ar/metal ion bombardment and an enhanced material removal (sputter cleaning) effect. However, when Ar is used during metal ion bombardment less metal ions are implanted at the substrate surface. To combine effective substrate surface cleaning (for short process times) and to maximise metal ion implantation a two stage process was developed.

# Chapter 5

# Microstructure of UBM deposited transition metal nitrides

## 5.1 Introduction

The previous Chapter describes how different substrate sputter cleaning procedures alter the substrate surface. The substrate surface strongly influences the ad-atom nucleation mode, nucleation density and interface formation. Surface roughness causes the film to grow in a less than fully dense manner due to geometrical effects. The surface chemistry affects nucleation, diffusion and reaction at the substrate surface [134]. Consequently, the microstructure of TiAlN deposited on different surfaces may also depend on the sputter cleaning procedure. It should be emphasised again that the process parameters for coating deposition were kept constant.

## 5.2 Results

### 5.2.1 Microstructure of TiAlN grown on amorphised metal surfaces

TiAlN grown on an amorphised stainless steel surfaces as obtained by Nb-ion bombardment exhibits small columns. The column size varies from a few nanometres close to the interface to several tens of nanometre on top of the 300 nm thick coating as can be seen in Figure 5.1. No evidence for pronounced inter columnar porosity

Figure 5.1: Dark field XTEM image of TiAIN grown on Nb-ion bombarded *(Us*= 1200 V) stainless steel.

was found. Similarly, small grain sizes compared to the grain size of the substrate are found when TiAIN was grown on a previously Ti-ion bombarded low carbon steel where amorphous and crystalline TiFe phases are present at the surface. Figure 5.2a is an in-plane BF image of the TiAIN coating deposited on Ti-ion bombarded low carbon steel. At this low magnification the coating grains can not be resolved. The higher magnification image in Figure 5.2b exemplifies typical grain sizes of tens of nanometres. In addition, it demonstrates the presence of larger grains (« 100 nm, centre region of the image). The arcs in the SADP taken from a region of 1 /im diameter in Figure 5.2c support the presence of small grains and indicates a limited degree of texture. The SADP in 5.2d was taken from a grain extending over several 100 nm and shows a [001] zone axis pattern. Figure 5.2e is a cross-sectional view, which represents again an area of small grains (tens of nanometres).

### 5.2.2 Microstructure of TiAIN grown on oxidised surfaces

In case of Ar-ion bombardment, where oxygen is present at the interface, the nucleation of randomly oriented grains is promoted leading to competitive column growth

$\-;v .

':.'K'r
tf£->5,$$£ :V:

t IQOnrrr

Figure 5.2: TiAIN grown on Ti-ion bombarded low carbon steel: (a) plan view TEM, (b) plan view TEM at higher magnification showing typical column sizes of few tens of nm but also one larger grain (centre of image), (c) Selected area diffraction pattern of a 1/mi area, (d) Selected area diffraction pattern of 300 nm area, and (e) XTEM image.

with small column size (few tens of nm) and open boundaries. This can be seen from the in-plane BF TEM image in Figure 5.3a, which was taken in under-focused conditions such that the open grain boundaries appear bright. The small column size is also reflected by the ring pattern of the SADP in Figure 5.3(b) taken from an area of « 1 gm in diameter. Figure 5.3c shows the cross-section of the TiAIN coating deposited after Ar-ion bombardment. Again open grain boundaries and small grains are visible, which is in agreement with the TEM plan view image (Figure 5.3a). In addition, it reveals the presence of an amorphous TiAIN layer with a thickness of several nanometres before columnar growth of the TiAIN film develops.

**Figure 5.3:** TiAIN deposited on Ar-ion bombarded surface *Us*= 1200 V for 20 minutes: (a) BF in-plane TEM (under focus), (b) SADP of 1/im area of the specimen shown in (a), and (c) BF XTEM image (under focused).

### 5.2.3 Microstructure of TiAIN grown on clean metal surfaces with preserved crystalline order

Figure 5.4a is an in plane BF image of TiAIN grown on low carbon steel after Cr-ion bombardment for 20 minutes at *Us*= 1200V, which was shown to provide a clean Cr implanted ferritic steel surface with well preserved crystalline order. A TiAIN grain extending over several microns is visible. It exhibits sharp grain boundaries. In 5.4b the corresponding DF image is presented. It was taken using the (220) reflection of the SADP in Figure 5.4c. An area of 5 gm contributed to form this spot pattern. This kind of spot pattern is characteristic for specimens that exhibit the same crystallographic orientation within the sampled volume. Figure 5.4d is an EDX spectrum, which confirms that the images in Figures 5.4a,b and d were indeed

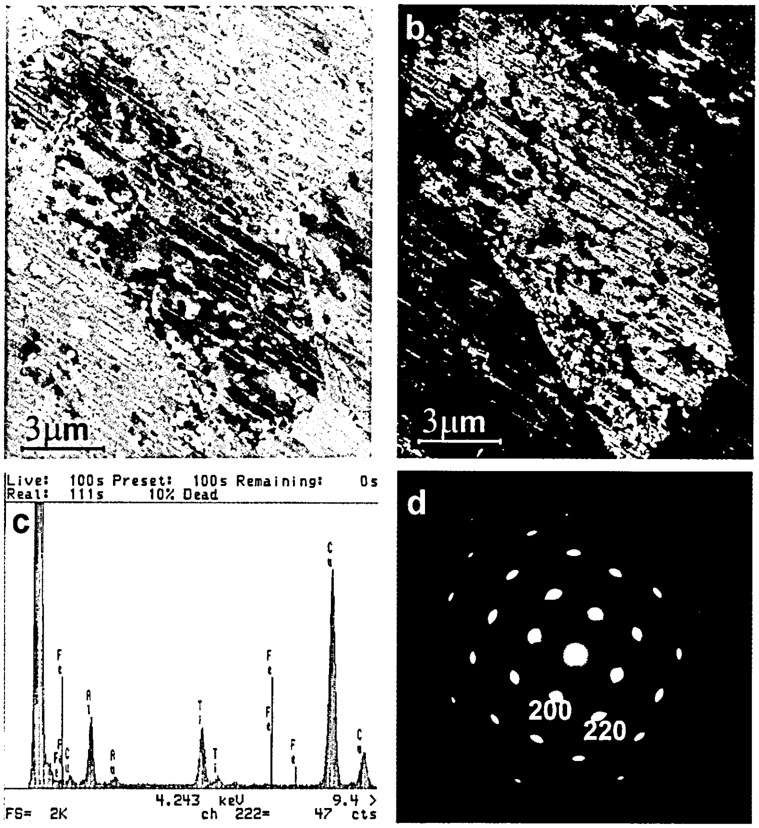

**Figure 5.4:** TiAlN grown on Cr etched low carbon steel $U_s = 1200\,\mathrm{V}$ or 20 minutes: (a) plan view BF, (b) plan view DF using (220) reflection, (c) EDX spectrum showing only Ti,Al peaks (coating) and Au,Cu (sample support), and (d) SADP of a $5\,\mu\mathrm{m}$ area.

taken from the coating rather than the steel substrate. No peaks were detected that correspond to Fe$K_\alpha$. Only Ti, Al, Cu, and Au are found. The last two elements are detected because the 100nm thick, free standing TiAlN film was sandwiched between a Au and a Cu mesh.

It can be seen from Figure 5.4 that the TiAlN grain is highly distorted. This can be seen in more detail in Figure 5.5. It shows selected area diffraction patterns taken of 300 nm areas at locations indicated by the letters in the BF image (Figure 5.5a). In this way it is evident that the large grain consist of subgrains that have misorientation angles of 2° to 6°. Figures 5.6a-f illustrates the orientation relationship between TiAlN and low carbon steel substrate in cross-sectional view. Figure 5.6a and b show convergent beam electron diffraction patterns (CBED) from film and

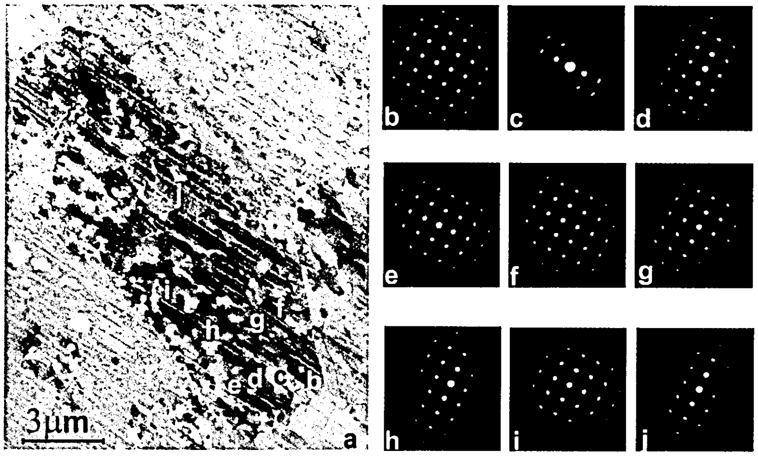

**Figure 5.5:** Plan view of TiAlN grown on Cr etched low carbon steel $U_s$= 1200 V for 20 minutes: (a) BF image and (b)-(j) SADP (300nm area) taken at the position of the letters in the BF image.

substrate areas shown in Figure 5.6c. The CBED patterns are indexed in Figures 5.6(d) and (e) and show that [$\bar{2}$00]TiAlN $\|$[101]$\alpha$-Fe. At the same time the [011] zone axis of the film is within several degrees away from the [$\bar{1}$11] zone axis pattern of the b.c.c substrate. Figure 5.6g clearly shows that the diffraction contrast in the grains of the film changes at a substrate grain boundary and is therefore related to the crystal orientation of the substrate. The DF image in Figure 5.6f is taken from the same region as the BF in Figure 5.6c using the (220) reflection and exhibits homogeneous contrast due to the same crystal orientation.

Large grain sizes and structural matching of the TiAlN film and substrate are also observed when tungsten carbide was exposed to Cr-ion bombardment for 20 minutes at $U_s$= 1200 V prior to TiAlN deposition (see Figure 5.7). Both, BF (Figure 5.7a) and DF images (Figure 5.7c) exhibit homogeneous contrast indicating that the same crystallographic orientation in the TiAlN film extends over the entire region shown in Figure 5.7. The SADP of the TiAlN film (f.c.c.) is shown in Figure 5.7b and Figure 5.7e represents the SADP of the underlying tungsten carbide grain. Figure 5.7d is a superimposition of the TiAlN SADP with the SADP of the simple hexagonal lattice of a tungsten carbide grain obtained by placing the selected area aperture at the interface.

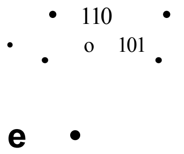

**Figure 5.6:** XTEM image of TiAIN grown on Cr-ion bombarded low carbon steel *Us*= 1200 V, 20 minutes: (a) CBED of TiAIN, (b) CBED of steel substrate, (c) BF image, (d) schematic DP of TiAIN, (e) schematic diffraction pattern of steel, (f) DF from (220) reflection, (g) BF image that shows grain boundary in TiAIN at same location as grain boundary in steel substrate.

### 5.2.4 Microstructure of TiAIN grown on locally clean surfaces

As discussed in Chapter 4 locally clean surfaces are obtained when the process conditions just begin to provide sufficient cleaning so that the dependence of sputtering yield on crystal orientation plays a major role. Grains with a lower sputtering yield will be either still contaminated or covered by a metal deposit of varying cleanliness and thickness. Two examples are given here. Cr-ion etching at a *Us*= 1200 V for only five minutes is an example for the presence of contamination, whereas Cr-ion bombardment at *Us*= 1000 V for 20 minutes leads, at least locally, to a Cr deposit.

Figure 5.8 is an in plane DF image of a TiAIN coating, which was deposited after Cr-ion bombardment for five minutes at *Us*= 1200 V. Two different microstructures are observed: (i) grains extending over several hundred nanometres up to micron size and (ii) very small grains (few tens of nanometres) as it was already observed after Ar-ion etching. For comparison a DF image of TiAIN deposited after Ar-ion etching was inserted in the left upper corner Figure 5.8.

Figure 5.9 shows in plane TEM images and selected area diffraction patterns

*I*

Figure 5.7: XTEM of TiAIN grown on Cr-ion bombarded tungsten carbide *Us*= 1200 V, 20 minutes: (a) BF, (b) SADP of TiAIN grain, (c) DF, (d) SADP with SA placed at interface so that the pattern is a superimposition of the TiAIN pattern and tungsten carbide pattern, and (e) SADP of tungsten carbide grain.

(area of 1 gm) of TiAIN grown on low carbon steel substrates after exposure to Cr-ion bombardment at *Us*= 600 V (Figure 5.9a,b) and *Us*= 1000 V (5.9c,d), respectively. The average grain size in the latter case is larger compared to that obtained after Cr-ion bombardment at *Us*= 600 V. Both SADP show rings, which are not completely uniform and reveal some in plane preferred orientation, indicative of a limited degree of texture. The latter effect is much more pronounced in case of Cr-ion bombardment at higher bias voltage. To further investigate the texture XRD was employed. However, glancing angle XRD is not suitable for that purpose since the diffraction vector of each diffraction plane can not be related to a common axis. Therefore, Bragg Brentano geometry should be used. However, the reflected intensities in this geometry for 100 nm TiAIN coatings are very low. Consequently,

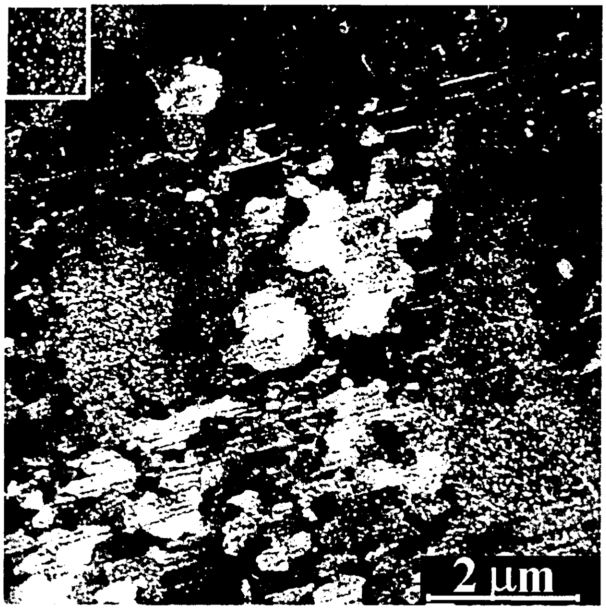

**Figure 5.8:** In plane DF image of TiAlN grown on low carbon steel after Cr-ion bombardment for 5 minutes at $U_s$= 1200 V, left upper corner: DF image of TiAlN deposited after Ar-ion bombardment.

CrN coatings, which exhibit a similar structure to TiAlN with a very similar lattice parameter of 0.414 nm [91] and have at the same time much higher reflected intensities [1] were used to obtain texture information by the Bragg Brentano method. Figure 5.10 shows a comparison of the XRD traces in Bragg Brentano (Figure 5.10a) and glancing angle (Figure 5.10b) geometry obtained from 100 nm CrN coatings deposited on Nb-ion bombarded ($U_s$= 1200 V) stainless steel. Expected CrN peak positions are given by the red lines in Figure 5.10a (The green lines denote peak positions of the austenitic stainless steel substrate.). Out of all possible peak positions only a very intense (200) peak is observed, whereas the most intense peak in the glancing angle geometry for the same specimen is at the (422) position. Similarly, the most intense coating peak (TiAlN coating) for a Ti bombarded stainless steel specimen ($U_s$= 1200 V) in glancing angle geometry arises from the (422) planes as seen in Figure 5.10c.

---

[1] The proportion of the intensity reflected by the coating increases for strong absorbing coatings. The absorption coefficient for CrN is approximately 3.5 times larger than for TiAlN for $CuK_\alpha$ radiation (8.05keV) as can be estimated using the values given in [135].

**Figure 5.9:** In plane BF image and SADP of TiAlN grown on low carbon steel after Cr-ion bombardment for 20 minutes at *Us* = 600 V (a) and (b), and after Cr-ion bombardment for 20 minutes at *Us* = 1000 V (c) and (d).

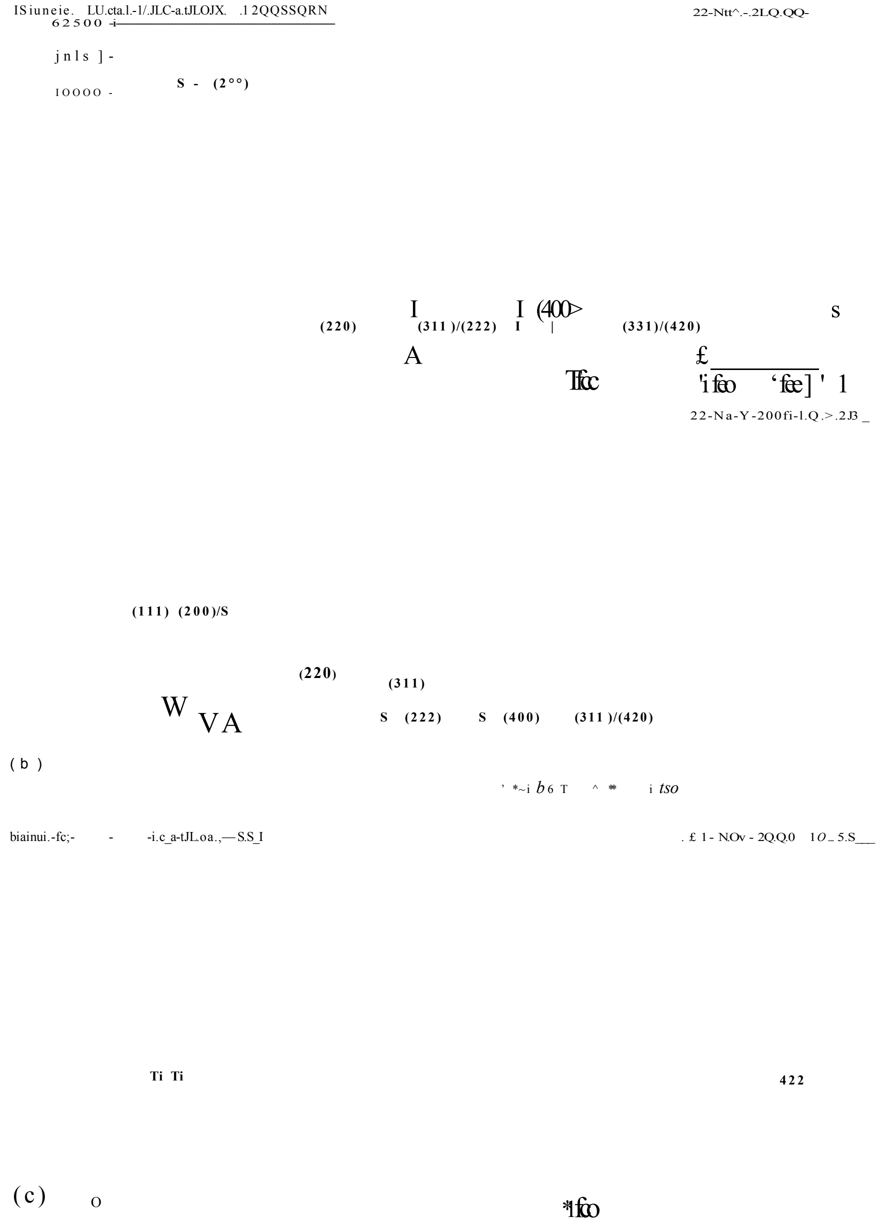

**Figure 5.10:** XRD traces taken of 100 nm films: (a) in Bragg-Brentano geometry, sample: CrN deposited on Nb bombarded stainless steel, (b) the same specimen as in (a) but glancing angle geometry, and (c) TiAlN deposited on Ti-ion bombarded stainless steel XRD in glancing angle geometry. The Ti reflections are thought to arise from Ti-droplets.

## 5.3 Discussion

### 5.3.1 Microstructure of TiAlN grown on amorphised surfaces

On an amorphous substrate random nucleation should occur and coarsening effects due to minimisation of epitaxial strain energy are not expected [85]. From that point of view one would expect a completely random orientation of the grains and a grain size determined by the nucleation rate. Indications for an amorphised substrate surface were found for Nb-ion bombarded stainless steel, and Ti-ion bombarded low carbon steel and stainless steel. Indeed, all three samples show the expected small grain size as can be seen in Figures 5.1 and 5.2. Although for an amorphous substrate no energy minimisation processes based on the decrease of strain energy or interfacial energy are expected, the driving force for energy minimisation would be the reduction of surface energy which can lead to texture development. A surface energy minimising texture for TiN (f.c.c) would be a (100) texture for small film thickness ([136] and [137]) [2] . Thus, the presence of such a texture in the 100 nm thick films would give further evidence for the amorphisation of the substrate material [3] . The Bragg-Brentano XRD [4] trace taken from a CrN coated Nb-ion bombarded stainless steel is shown in Figure 5.10a. Indeed, it reveals a very strong (100) texture since no other peaks than (200) and (400) are visible. The corresponding XRD trace taken in glancing angle geometry is presented in Figure 5.10b. The most intense peak is the (422) peak at $2\theta = 131^{\circ}$. This corresponds again to a (100) in plane texture because the angle between (422) and (100) planes in a cubic system is 65.54°. The Ti-ion bombarded stainless steel specimen was coated by TiAlN which did not give rise to sufficient coating peak intensities in Bragg-Brentano geometry. However, using the same argument as before the dominance of the (422) peak in

---

[2] This means that the (100) planes are parallel to the coating surface.

[3] A third minimisation mechanism would be strain reduction for thicker films [137] and texture development due to congruent ion bombardment during film growth could lead to a mixed texture. However, in cases were film thickness, stress and ion bombardment were the same, changes in texture should be related to the nature of the substrate surface.

[4] In Bragg-Brentano geometry only crystal planes which are parallel to the coating surface are recorded.

Figure 5.10c points again towards a (100) in plane texture. The presence of the (100) in plane texture, which is expected when the coating evolves on an amorphous substrate emphasises again that Nb and Ti-ion bombardment of stainless steel lead to amorphisation of the substrate surface. Such a clear indication for a strong (100) texture is not observed for the Ti-ion bombarded low carbon steel, which is reasonable considering that Mössbauer spectroscopy shows evidence for the presence of an amorphous and a crystalline phase at the substrate surface. For a crystalline phase, however interface energy minimisation effects will play a role in addition to surface energy minimisation resulting in a different texture. It is assumed that the larger grains (evident from Figure 5.2b and d) correspond to an underlying crystalline phase in the low carbon steel substrate.

### 5.3.2 Microstructure of TiAlN grown on oxidised surfaces

Due to the amorphous interlayer which was observed in XTEM imagining in Figure 5.3c it is not surprising to find a similar microstructure (columnar growth) as for TiAlN deposited on an amorphised steel surface. However, in contrast to the latter case, here the grain boundaries exhibit a very open structure. It can be speculated that the observed change in microstructure from amorphous to columnar growth is related to the variation in chemical composition of TiAlN close to the interface. As described in Section 4.2.2 a high oxygen concentration in the coating close to the interface was found by EELS analysis. A similar observation of the formation of an amorphous interfacial layer due to the presence of impurities like oxygen and hydrogen was reported when TiN was sputter deposited using a cylindrical titanium hollow cathode in an $\mathrm{Ar}-\mathrm{H}_2-\mathrm{N}_2$ plasma at a pressure of 10 Pa and substrate temperatures below 620 K [138]. On the assumption that water vapour is the main source of contamination, optical emission spectroscopy was used as an impurity indicator of the sputter atmosphere using the hydrogen Balmer series. It was proven that operations prior to the coating phase were performed in a polluted environment. A drop in the impurity partial pressures was observed at the beginning of the deposition phase that is related to the amorphous layer formation [138].

### 5.3.3 Microstructure of TiAlN grown on clean crystalline surfaces

As seen in the previous Section and also found by other workers the grain size of transition metal nitrides close to the interface is in the range of several nanometres. For example Andrievski *et al.* report gain sizes for TiN in the range of five to ten nanometres [139]. Therefore the large areas of similar crystal orientation as observed in Figure 5.4 are unexpected. That this is not an artifact due to remaining substrate material is evident from the SADP and the EDX spectrum presented in Figure 5.4c. The latter suggests that all substrate material was removed since no iron was found within the detection limit. However, a remaining substrate layer could have been present which was too thin to be detected by EDX. In that case an overlapping pattern from coating and substrate would be present in Figure 5.4d. Since this is not the case the spot pattern taken from an area as large as 5 $\mu$m arises from the TiAlN film and the bright area extending over several micrometer in Figure 5.4b has the same crystallographic orientation and represents therefore one TiAlN grain. Similar large grain sizes of 1 $\mu$m for TiN were found when TiN was sputter deposited onto Al [140] [5] . The size of the grains was also measured using in plane TEM DF imaging. Higher magnification in plane TEM images taken with a very large over focus reveal however a clear contrast between subgrains within a given grain. The subgrains exhibit boundary regions with a much reduced density such as chains of voids. These subgrains exhibit an orientation variation of 5° to 10° as obtained by measuring the orientation variation of lattice planes in high resolution microscopy, from tilting experiments and the length of the arc of a given reflection in the SADP. The evolution of the subgrain structure was attributed to roughening instability by shadowing. Here, a small perturbation at the surface leads to a reduction in the flux seen in the shadow region of the perturbation. This leads to a stabilisation of the initial roughness and results from a low ad-atom mobility in a columnar growth mode. A columnar appearance was also found in XTEM imaging.

---

[5] Interesting to note that this was achieved for deposition temperatures in the range of 200°C to 400°C.

Similarly, a subgrain structure was observed for the TiAlN films investigated here. The orientation variation was also in the range of several degrees as established from tilting experiments and from the shape of the diffraction spots in Figure 5.4d. It was also shown by the rotation of the individual patters in Figure 5.5. However, low density regions at the boundaries of these subgrains were not found and the appearance in XTEM is not columnar as can be seen in Figure 5.6c and f. This is thought to be a result of the high mobility due to effective ion bombardment of the substrate when a closed field unbalanced magnetron deposition arrangement is used. The evolution of this subgrain structure might be a result of the roughening of the substrate during metal ion bombardment, which produces local changes in surface orientation within a single substrate grain as shown in Figure 4.7.

De Schepper *et al.* [141] observed the same phenomena for PVD deposited TiN with austenitic stainless steel as substrate material but they describe it in a different way. The initial TiN layer (thickness less than 1000nm) is built up of small grains (mean size 20 nm). These grains do not form a simple polycrystalline layer but are grouped together in larger micrometer-size entities of grains, called 'supergrains', with the same preferential crystal orientation. The orientation of such a supergrain is characterised by a f.c.c. crystal direction vector $B$ perpendicular to the substrate surface. Supergrains in TiN directly deposited on austenite have a $B$ vector identical to that of the underlying austenite grain, i.e. full epitaxy occurs between the austenite grain and the supergrain.

Evidence for local epitaxial growth in our experiments is shown by XTEM imaging and electron diffraction as presented in Figures 5.6 and 5.7. The attempt was made to establish an orientation relationship between TiAlN and steel substrate by convergent beam diffraction. The pattern of the $\alpha - \mathrm{Fe}$ identified as $[\bar{1}11]$ zone axis pattern and the pattern of the TiAlN film as [011] zone axis pattern such that $[\bar{2}00]$TiAlN$||$[101]$\alpha$-Fe. At the same time it can be seen from Figure 5.6b that the pattern from the substrate is not exactly on the $[\bar{1}11]$ zone axis but is several degrees away from this axis. The observed relationship is therefore consistent with one established in [97], where the film lattice is rotated 45° around the [001] substrate grain so that the lattice mismatch is decreased from ≈ 31 % compression to ≈ 3% compression.

Local epitaxial growth was also observed for TiAlN deposited on tungsten carbide as can be seen by the matching of the SADP in Figure 5.7d. However, in Figure 5.7a,c indications for a subgrain structure were found even in the cross-section. This can be seen by the pyramid shape tips of columns within regions of same crystallographic orientation. It should be mentioned here that the TiAlN film thickness is approximately 3 times that deposited on the low carbon steel substrate where the surface of the film remained flat. If the roughness is a result of shadowing then it would be expected to increase with increasing thickness.

### 5.3.4 Microstructure of TiAlN grown on locally clean surfaces

The microstructure found on such surfaces can be explained as a mixture of the microstructure on a clean crystalline surface where local epitaxial growth is observed and the columnar growth on contaminated regions (either thick metal deposit or not all oxide removed). Thus, regions with completely different microstructures are present within the same specimen. This is illustrated by the SADP (1 $\mu$m selected area) of the Cr-ion bombarded sample ($U_s$= 1000 V) in Figure 5.9d. A ring pattern is overlaid with a spot pattern. The latter representing a larger crystal being present in addition to small columnar grains that cause the ring pattern. The crystal size of the epitaxial region is, however, much smaller than in the case of Cr-ion bombardment prior to TiAlN deposition at $U_s$= 1200 V for 20 minutes. Re-crystallisation occurring in the deformed substrate layer during metal ion bombardment can explain this observation. A higher bias voltage during metal ion bombardment provides a higher energy input that can result in larger substrate grain sizes when re-crystallisation occurs. When the grains at the substrate surface are smaller the grain size of local epitaxial grown TiAlN would decrease. Although both STEM-EDX and XRD showed indications for a Cr deposit for Cr-ion bombardment at $U_s$= 1000 V this is expected to be only localised and/or at least locally very thin and clean. Such conditions could again provide a clean surface with crystalline order via epitaxial growth of Cr on the low carbon steel so that local epitaxy of TiAlN can still occur. Regions with thick Cr deposits will lead to columnar growth as demonstrated for example in Figure 5.9a for a thicker deposit formed during Cr-ion bombardment at $U_s = 600\,\mathrm{V}$. It was shown by XTEM and convergent beam diffraction that in case of the thinner Cr layers local epitaxy still occurs [142]. Similarly local epitaxially grown TiAlN and columnar grown TiAlN are coexisting at the specimen Cr-ion bombarded at $U_s = 1200\,\mathrm{V}$ but for only five minutes.

## 5.4 Summary

For clean tungsten carbide and low carbon steel surfaces which were not amorphised during metal ion bombardment local epitaxial growth of TiAlN expressed by large grain sizes of several micrometers was found. However, these grains consist of subsgrains with orientations rotated about several degrees.

A high oxygen incorporation in the TiAlN film (TiAlON) lead to an amorphus microstructure. When the oxygen content is reduced, columnar growth with grain sizes in the range of tens of nanometres develops. Columnar grown TiAlN was also found to occur on amorphised substrate surfaces. Columnar growth and local epitaxial growth are coexistent in the case of only locally clean substrate surfaces.

# Chapter 6

# Mechanical properties of coated systems

## 6.1 Introduction

The previous Chapters have shown how the sputter cleaning procedure prior to coating deposition affects interface microstructure and microchemistry. This Chapter is focused on the influence of those properties on the behaviour in mechanical testing. Finally, the consequences for dry high speed machining applications were investigated.

## 6.2 Results

### 6.2.1 Stress

The stress values presented in Table 6.1 were all determined from the slope of the lattice parameter versus $\sin^2\psi$ plot. An example is given in Figure 6.1 for a 100 nm TiAlN film grown on a low carbon steel substrate exposed to Cr-ion bombardment at $U_s$= 1200 V for 20 minutes.

| Ion | $U_s$ in V | Time in min | Pressure in Pa | Substrate | Stress in GPa | Microstr. |
|---|---|---|---|---|---|---|
| Ar | 1200 | 20 | 0.06 | low carbon | -3.6 | c |
| Cr | 600 | 20 | 0.06 | stainless | -5.2 | |
| Cr | 600 | 20 | 0.06 | low carbon | -7.2 | c+e |
| Cr | 1200 | 20 | 0.06 | low carbon | -8.0 | e |
| Cr | 1200 | 20 | 0.06 | stainless | -7.9 | |
| Cr | 1200 | 10 | 0.06 | stainless | -8.3 | |
| Cr | 1200 | 8 + 2 | 0.09+6x10$^{-3}$ | low carbon | -6.4 | e |
| Cr | 1200 | 8 + 2 | 0.09+6x10$^{-3}$ | stainless | -6.7 | |
| Ti | 1200 | 20 | 0.06 | stainless | -5.1 | c |

**Table 6.1:** Stress of 100 nm TiAlN films grown after various substrate sputter cleaning procedures, **c** stands for columnar and **e** for epitaxial growth. If there is no entry XTEM analysis was not carried out. The stress values were determined using Equation 3.8 with $E = 400\,\text{GPa}$ and $\nu = 0.3$.

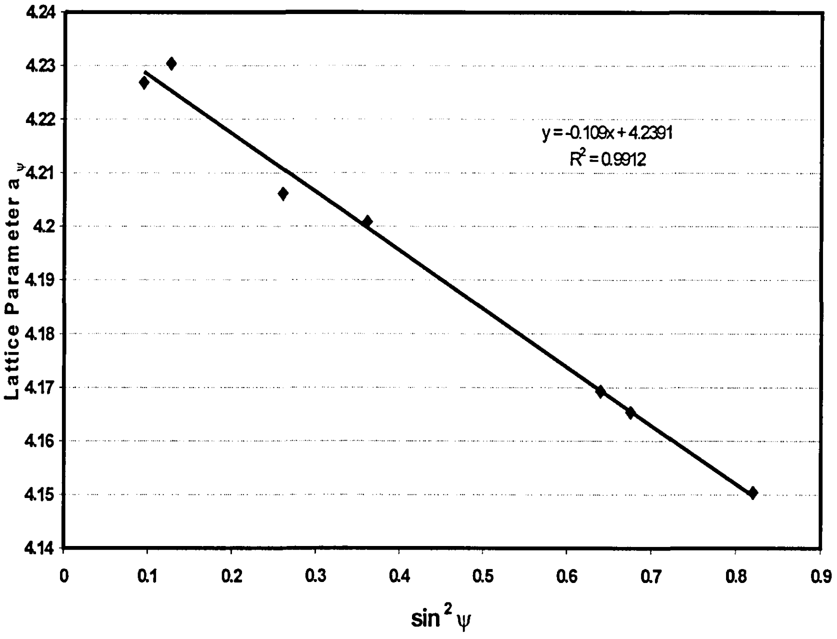

**Figure 6.1:** Lattice parameter versus $\psi^2$ for stress determination. This plot was obtained from the XRD traces of a TiAlN film grown on a low carbon steel substrate, which was exposed to Cr-ion bombardment at $U_s$= 1200 V for 20 minutes.

### 6.2.2 Practical adhesion

A first impression of the practical adhesion was obtained by Rockwell indentation tests. Examples for 3.5 $\mu$m thick TiAlN based coatings on tungsten carbide substrates are shown in Figure 6.2. Delamination of the coating along the entire circumference is observed in case of coating deposition after Ar-ion bombardment in Figure 6.2a. The area where the coating delaminates is reduced when Cr-ion bombardment at $U_s$= 600 V was employed for substrate sputter cleaning (Figure 6.2b). Exposure to Cr-ion bombardment at $U_s$= 1200 V prior to coating deposition prevents delamination in Rockwell indentation tests (Figure 6.2c).

A quantitative measure was obtained from scratch adhesion testing. The scratch tracks for the same three samples presented in Figure 6.2 are shown in Figure 6.3. The first sign of adhesive failure for the sample where Ar-ion bombardment was used for sputter cleaning was observed at 34 N. This is shown in Figure 6.3a and

Figure 6.2: Rockwell indentations in TiAIN deposited on tungsten carbide after: (a) Ar-ion bombardment *Us* = 1200 V, (b) Cr-ion bombardment *Us* = 600 V, and (c) Cr-ion bombardment *Us* = 1200 V.

is consistent with large areas of delamination surrounding the Rockwell indentation (Figure 6.2a). Cr-ion bombardment at *Us* = 600 V results in a higher critical load value of 68N. Cr-ion bombardment at the higher bias voltage of *Us* = 1200 V leads to a further increase in the critical load. The first adhesive failure is a small spallation on the side of the scratch track at 141 N (6.3c). The critical load values measured for

A Va--

: ; 'J-;,

Figure 6.3: Scratch tracks in TiAIN deposited on tungsten carbide after: (a) Ar-ion bombardment *Us* = 1200 V, (b) Cr-ion bombardment *Us* = 600 V, and (c) Cr-ion bombardment *Us* = 1200 V.

all samples suitable for scratch testing (3.5 gm thick TiAIN coating) are summarised in Table 6.2.

| Ion | $U_s$ in V | Time in min | Pressure in Pa | $L_c$[HSS] in N | $L_c$[cc] in N | Microstr. |
|---|---|---|---|---|---|---|
| Ar | 1200 | 20 | 0.06 | 27 ± 4 | 35 ± 2 | c |
| Cr | 1200 | 5 | 0.06 | 36 ± 4 | 67 ± 3 | e+c |
| Cr | 600 | 20 | 0.06 | 37 ± 3 | 58 ± 3 | c+e |
| Cr | 600 | 20 | 0.06 | 47 ± 5 | 68 ± 3 | c+e |
| Nb | 1200 | 20 | 0.06 | 50 ± 4 | 92 ± 4 | c |
| V | 1200 | 20 | 0.06 | 62 ± 3 | 113 ± 4 | e |
| Cr | 1200 | 20 | 0.06 | 59 ± 4 | 97 ± 5 | e |
| Cr | 1200 | 20 | 0.06 | 63 ± 3 | 141 ± 3 | e |
| Cr | 1200 | 8 + 2 | $0.09+6\text{x}10^{-3}$ | 85 ± 3 | – | e |

**Table 6.2:** Critical load values (first adhesive failure) measured on 3.5 $\mu$m thick TiAlN based coatings deposited on HSS and tungsten carbide (cc), respectively for various sputter cleaning pre-treatment procedures, **c** stands for columnar and **e** for epitaxial growth.

| Ion | $U_s$ in V | Time in min | Pressure in Pa | Life time in min |
|---|---|---|---|---|
| Ar | 1200 | 20 | 0.06 | 21 |
| Cr | 1200 | 5 | 0.06 | 27 |
| Cr | 600 | 20 | 0.06 | 25 |
| Cr | 600 | 20 | 0.06 | 28 |
| Nb | 1200 | 20 | 0.06 | 30 |
| V | 1200 | 20 | 0.06 | 36 |
| Cr | 1200 | 20 | 0.06 | 38 |
| Cr | 1200 | 20 | 0.06 | 40 |
| Cr | 1200 | $8 + 2$ | $0.09+6x10^{-3}$ | $37 \pm 4$ |

**Table 6.3:** Life time in dry high-speed machining experiments of 3.5 $\mu$m thick TiAlN based coatings deposited on tungsten carbide ball nosed end mills using various sputter cleaning pre-treatment procedures.

### 6.2.3 Life time of coated tools in dry high-speed machining tests

Life times in dry high-speed machining of hardened A2 (58HRC) for ball nosed tungsten carbide end mills, coated with a 3.5 $\mu$m TiAlN based coatings deposited after various substrate sputter cleaning procedures are given in Table 6.3.

## 6.3 Discussion

### 6.3.1 Practical adhesion and its relation to interface properties

In this Section we omit the influence of stress on the measured practical adhesion and focus only on the relation between microstructure and elemental composition of TiAlN close to the interface and the practical adhesion. On examining the critical load values for HSS substrates in Table 6.2 one can define three classes of critical load values: (i) $\leq$ 30 N (ii) 30 N $\leq L_c \leq$ 50 N and (iii) values in the range of 60 N and higher. This classification is also reflected by the different levels of coating delamination found in Rockwell indentation tests and can be directly correlated to the microstructure of TiAlN. All coatings, exhibiting columnar growth only or locally, fall into the first two groups with the lower critical load values. In contrast coatings were only epitaxial growth is involved show all critical load values in the range of 60 N and higher. This means that local epitaxy seems to have an beneficial influence on practical adhesion as can be expected from the interfacial energy considerations discussed in Section 2.2.3. However, the doubling in the scratch value compared to group (i) can not only be attributed to local epitaxial growth. As described in Chapter 5, columnar growth can occur on a clean but amorphised surface or when a high oxygen content is involved. In this context the significantly higher critical load value of 50 N observed after Nb-ion bombardment where columnar growth evolved due to an amorphised substrate should be mentioned. In contrast, the critical load value was only 27 N for columnar growth on the Ar-ion bombarded substrate surface where an amorphous interlayer caused by a high oxygen incorporation was present. In the latter case the low adhesion is most likely a result of the interface brittleness [138], which is related to the amorphous interlayer. A high oxygen concentration at the TiN/ HSS interface in conjunction with relatively poor adhesion (40 N) was also reported in [143] and [144] for arc deposited TiN at 550K. When the oxygen concentration was reduced by using a higher deposition temperature of 730K the critical load was increased to 60 N. Thus, the presence of oxygen at the interface led to a difference in critical load of 20 N as it was the case in our experiments where both coatings exhibit columnar growth but only one has a high oxygen concentration (Ar etch: 27 N, Nb etch:50 N) [1] . This result emphasises the importance of an impurity free environment in order to grow well adhered transition metal nitride coatings. To achieve this, two approaches can be used. Firstly, one can use a highly energetic metal ion bombardment prior to coating deposition. The second approach is the deposition of a metallic interlayer, which takes over the getter function, that

---

[1] Absolute scratch values can not be compared directly because parameters like coating thickness, toughness, roughness diamond crystal orientation etc. influence the absolute value.

is automatically involved in metal ion etching using a cathodic arc source. The work presented here is an example for the first approach. It was used successfully by others. For example it was found that etching of the surface by Ti-ion bombardment with a high bias voltage was very effective in improving the adhesion of a TiN film on Co-WC [145] as found by Rockwell C indentation tests. The metallic interlayer approach is frequently used for example for deposition on oxidised surfaces. In [146] the influence of Ti interlayers on the adhesion of PVD TiN coatings on oxidised stainless steel substrates was investigated using a pull-off test for adhesion measurements and scanning tunnelling microscopy and secondary ion mass spectrometry for analysis of the fractured surfaces. It was shown that the thickness of the Ti layer must be chosen according to the thickness of the oxide layer. An excess of Ti leads to lower adhesion values due to failure in the Ti layer, while a deficiency of Ti leads to unreacted oxide and minimum adhesion due to brittle fracture in the oxide layer, which was shown to be amorphous. Similarly, critical loads in adhesion tests with values of $\approx 35\,\mathrm{N}$ where no metallic interlayer was present and up to $60\,\mathrm{N}$ in the presence of a $200\,\text{Å}$ thick Ti interlayer were measured by Kim *et al.* [147]. They investigated the interfacial composition profile by Auger depth profiling. The experimental results indicated that a thin Ti intermediate layer ($\leq 600\,\text{Å}$) could increase the adhesion and the critical normal force in the scratch adhesion test was up to $60\,\mathrm{N}$. In the case of Ti interlayer formation, the oxygen in the interfacial region plays an important role on the adhesion of TiN coating by the formation of a Ti(ON) type phase [2] . As can be seen from these two examples the metallic interlayer approach introduces an additional crucial variable, which is the metal layer thickness. This has to be adjusted to the amount of oxygen that can react with the metal during deposition. However, this amount can vary widely in an industrial process depending on the chamber load. Therefore the risk of process instability and the dependence of adhesion on the chamber load is inherent to the interlayer approach. Although the duration of high energetic ion bombardment has to be adjusted in our case in order to avoid oxygen incorporation at the interface an overestimated

---

[2] There is a risk that mechanical failure may occur in the partially oxidised Ti-layer, in particular when tools are used for interrupted cutting or punching.

residual oxygen concentration does not reduce the stability of the process provided that the energy of the metal ions is high enough such that no deposition layer is formed (in our experiments $U_s$= 1200 V).

### 6.3.2 Relation between film stress and microstructure

There are three mechanisms that contribute to stress formation in thin films. Those are related to the different stages of coating formation. These are:

(I) Epitactic stresses during nucleation

(II) Generation of defects during layer growth

(III) Cooling stresses due to different thermal expansion of film and substrate [148].

The last two contributions should be constant for all experiments due to the use of identical deposition parameters. Hence, the variation of stress levels should be correlated to the observed microstructure. Due to the smaller thermal expansion coefficients of the coating material ($\alpha_{\mathrm{Fe}} = 12 \times 10^{-6}\,\mathrm{K}^{-1}$, $\alpha_{\mathrm{AlN}} = 5.7 \times 10^{-6}\,\mathrm{K}^{-1}$ and $\alpha_{\mathrm{TiN}} = 9.4 \times 10^{-6}\,\mathrm{K}^{-1}$ [40]) it is expected to find the coating under compressive stress. Another contribution to the compressive stress is the incorporation of working gas atoms and nitrogen atoms at interstitial sites [148]. Therefore it is not surprising that compressive stresses are found in all samples.

The lowest compressive stress level with −3.6 GPa was found on coatings deposited on Ar-ion bombarded surfaces. Here a very open structure due to oxygen incorporation was found by TEM investigations. For such an open structure low stress values are expected.

A compressive stress level of −5.1 GPa was found for a TiAlN film deposited on a Ti-ion bombarded stainless steel surface in which case due to amorphisation of the substrate columnar growth occurred. This can be anticipated since in this case no stress contribution arising from lattice mismatch accommodation is expected. A similar low stress level is found for TiAlN grown on stainless steel after low bias ($U_s$= 600 V) Cr-ion bombardment. Although no XTEM investigation was carried out for that specimen columnar growth is expected due to the formation of a deposition layer of Cr. This deposition layer also exists at least locally on the low carbon steel sample treated under the same conditions but here besides columnar growth local epitaxial growth was found by XTEM imaging (see Section 5.3.4). This explains the higher stress of $-7.2\,\mathrm{GPa}$ compared to coatings exhibiting mainly columnar growth. A still higher compressive stress ($-7.9\,\mathrm{GPa}$ to $-8.2\,\mathrm{GPa}$) was found for all specimens that were Cr-ion bombarded in an Ar atmosphere and exhibit exclusively local epitaxial growth. In contrast the samples Cr-ion bombarded without Ar as support gas in the final step (2 step procedure) exhibit lower compressive stress values ($-6.4\,\mathrm{GPa}$ and $-6.7\,\mathrm{GPa}$), despite the fact that no columnar but only local epitaxial growth was observed. It is assumed that the higher Cr content found at the steel surface resulting from the two stage sputter cleaning procedure could be responsible for an increase of the lattice parameter of the substrate, which should reduce the mismatch between steel and TiAlN coating, therefore leading to a lower epitaxial stress component and a flatter stress gradient at the interface. Similar observations have been made for plasma nitriding the surfaces [149] and [150].

### 6.3.3 Stress distribution at the interface and its relation to practical adhesion

In Section 6.3.1 only the influence of chemical composition and microstructure was related to practical adhesion. Although this could explain most of the experimental results it could not answer the question why interfaces, which are similar in microstructure and oxygen content, exhibit significant differences in practical adhesion. A possible explanation could be the difference in stress distribution. The stress levels measured directly at the interface of the etched, but uncoated austenitic stainless steel substrates are too low to be quantified. However, high compressive stresses were found in the 100 nm thin coatings grown after most sputter-cleaning processes as described before. The interface with lower Cr incorporation exhibits a higher compressive residual stress in the coating ($-8.3\,\mathrm{GPa}$) in comparison to the case when pure Cr-ion bombardment was involved ($-6.7\,\mathrm{GPa}$). The lower stress gradient found for the two stage etching process might explain the significant differences in the critical load values $L_c$ obtained for both interfaces. As described in Section 2.2.4 for coatings under compressive stress the critical load is decreased since the effective stress is the sum of the residual compressive stress and the stress generated by the moving indenter in scratch testing [84]. Indeed, the critical load values for samples processed in the two step etching mode (−6.7 GPa) showing the enhanced Cr incorporation ranged at $L_c = 85 \pm 5\,\mathrm{N}$ compared to samples prepared after the one step etching procedure $L_c = 63 \pm 3\,\mathrm{N}$ (−8.3 GPa).

An enhanced practical adhesion due to stress reduction at the interface was reported for example in [151]. An investigation was carried out to study the effect of substrate-bias voltage, and of the interface layer on the mechanical and tribological properties of Ta-C films. The films were prepared by a two-step process. A relatively thick, hard layer of Ta-C film is deposited on top of a relatively thin soft adhesive (interface) layer, which is deposited on a silicon substrate. An improved adhesion was observed for the Ta-C film prepared at $U_s = 3500\,\mathrm{V}$. The authors attribute that partially to the lower internal stress of the interface as measured by the radius of curvature method. Bull *et al.* [114] also partially contribute an improved adhesion of TiN when deposited on relatively soft Ti interlayer to the reduction of shear stress across the coating/ substrate interface.

However, the relatively low stress level found when coatings were deposited after Ar-ion bombardment (−3.6 GPa) demonstrates that low interfacial stresses do not guarantee good practical adhesion.

### 6.3.4 Relationship between practical adhesion and tool life in dry high-speed machining

By plotting the life time in dry high-speed milling versus the practical adhesion of $3.5\,\mu\mathrm{m}$ thick TiAlN based coatings deposited on HSS and cemented carbide substrates, respectively a direct correlation between life time and practical adhesion is revealed in Figure 6.4. Scratch values obtained on HSS substrates were included. Again a correlation between these values and the life time of the coated tungsten carbide milling cutters was found[3]. It holds for all tested coatings expect the one with the highest value in scratch testing obtained when the two step Cr etching procedure was employed.

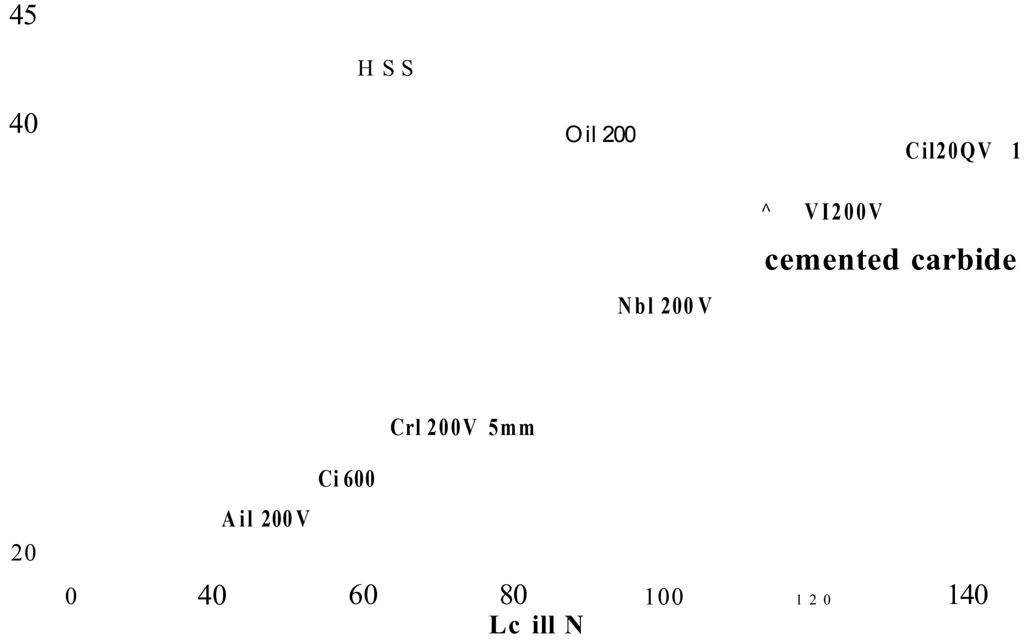

**Figure 6.4:** Correlation between life time of TiAIN based coated tungsten carbide end mills in dry high-speed machining of hardened A2 and critical load in scratch adhesion testing.

To the author's knowledge no such correlation has been published before although it was mentioned by Helmersson *et al.* [48] that Billgren *et al* have found a correlation between critical load values and life time in milling operations. However we did not find such results published by the above named author.

That the highest critical load of 85 N measured on HSS does not prolong the life as could be expected from the linear relationship between critical load and life time in all other experiments might indicate that a different failure mechanism begins to

---

[3] This implies that scratch tests performed on HSS substrates could be used for the quality control of tungsten carbide coated tools. This is desirable because HSS disks are more readily available than tungsten carbide disks and the lower critical loads obtained on HSS substrates lead to less diamond wear per scratch.

determine the life time that could be related to the high temperature involved in dry high-speed machining. The scratch test was performed at room temperature and reflects the practical adhesion under those conditions. It was found in heat treatment experiments of TiAlN that exposure to an reactive atmosphere (air) at a temperature of 900° for 1 hour leads to severe diffusion of substrate elements into the coating thus reducing the stability of the interface. Large localised low density zones are observed which are related to areas where grain boundaries meet the substrate surface [152]. These areas a likely to be responsible for a loss of adhesion.

## 6.4 Summary

A correlation between the microstructure of TiAlN and practical adhesion was revealed. Coatings where columnar growth is involved exhibit at least 10 N lower critical loads than those where only local epitaxial growth is observed. This is remarkable because the higher stress levels often found in case of local epitaxial grown coatings are expected to have a negative influence on the practical adhesion. It was shown that coatings that exhibit local epitaxial growth but a lower compressive stress show better practical adhesion as measured by scratch testing. It is proposed that the epitaxial stress component can be controlled by metal ion implantation taking place during metal ion bombardment prior to coating deposition. Higher implanted doses can increase the lattice parameter of the substrate thus, reducing the lattice mismatch between coating and substrate. It was also found that the chemical composition (impurity concentration) can drastically reduce the practical adhesion due to the formation of a brittle phase.

A direct correlation between practical adhesion and life time in dry high-speed machining was found for critical load values on cemented carbide up to 140 N (corresponds to 60 N on HSS and to a life time of 40 minutes). A further increase in practical adhesion did not result in a longer life time. It is assumed that this is due to a change in failure mechanism occurring after about 40 minutes of tool operation.

# Chapter 7

# Conclusions

It has been shown that sophisticated analysis techniques like transmission electron microscopy in combination with energy dispersive x-ray analysis and electron energy loss spectroscopy are powerful tools to relate the properties of transition metal nitride /steel interfaces to the performance of the coated systems. An understanding of the relation between ion bombardment induced topography changes and interface properties was developed. Using that knowledge, results of optical microscopy can be interpreted much more comprehensively. In particular, the efficiency of substrate etching can be judged.

This study also proves that critical loads determined by scratch testing provide reproducible results and indeed reflect interface properties, provided the coatings of the tested systems were deposited under the same conditions and exhibit an identical thickness. Under those conditions a direct correlation between critical load, referring to the observation of the first adhesive failure and tool life in dry high-speed milling of hard materials, was established.

An attempt was made to extract key parameters, which are most important in order to employ the sputter cleaning step of interface engineering for certain applications as it was shown here for dry high-speed machining of hard materials. Those key parameters are:

- Ion species

  - Cr to achieve enhanced adhesion through local epitaxial growth, with Cr providing smoother surfaces because of less droplet related growth defects
  - Nb for an amorphised Nb deposition layer on stainless steel (e.g. to protect stainless steel against corrosive attack in Cl ion containing solutions)

- Ion energy (bias voltage)
  - $U_s$= 1200 V for effective sputter cleaning to promote nucleation conditions which can lead local epitaxial growth
  - 600 V $\leq U_s \leq$ 800 V for the formation of amorphised Nb deposition layer to protect stainless steel against corrosive attack in Cl-ion containing solutions

- Exposure time

  It was shown that the getter effect of highly reactive metal ion bombardment for $O_2$ seems to be a key factor to achieve clean surfaces by lowering the residual oxygen partial pressure so that re-contamination is delayed. A ten minute treatment seems to be sufficient for that purpose.

- Working gas pressure
  - Cleaning efficiency

    The Ar pressure should be high but not exceed 0.1 Pa for maximum material removal and minimized differences in material removal as a result of sample geometry and a minimum Ar concentration trapped in gas bubbles.
  - Metal ion implantation

    To achieve maximum metal implantation effects no Ar should be used. First results indicate that metal implantation can be employed to control the stress gradient at the interface.

This suggests the use of a two stage process in order to combine high cleaning efficiency with mainly Ar-ions (shorter process) and excellent adhesion achieved by Cr-ion implantation.

It was further shown that solely interface engineering can double the life time of tools used for dry high-speed milling by providing a clean surface with well preserved crystalline structure. This results in local epitaxial growth of the transition metal nitride on the substrate when Cr ion bombardment at $U_s = 1200\,\mathrm{V}$ is employed prior to coating deposition. This enhances the adhesion compared to the case of columnar growth with inter columnar porosity. A porous coating is obtained when deposition is carried out on a surface where oxides are present, as in the case of Ar-ion bombardment. It was also found that the stress gradient at the interface has a strong influence on the practical adhesion of transition metal nitride coatings on steel substrates.

# Bibliography

[1] D.S. Rickerby and A. Matthews. *Advanced Surface Coatings: A Handbook of Surface Engineering.* Blackie and Son Ltd, Glasgow, 1991.

[2] S. J. Bull. Failure modes in scratch adhesion testing. *Surface and Coatings Technology*, 50:25–32, 1991.

[3] J. Musil, J. Vyskocil, and S. Kadlec. Hard coatings prepared by sputtering and arc evaporation. *Physics of Thin films*, pages 79–144, 1993.

[4] S. Creasey, D.B. Lewis, I.J. Smith, and W.-D. Münz. SEM analysis of droplet formation during metal ion etching by a steered arc discharge. *Surface & Coatings Technology*, 97(163):175, 1997.

[5] W.-D. Münz, I.J. Smith, D.B. Lewis, and S. Creasey. Droplet formation on steel substrates during cathodic steered arc metal ion etching. *Vacuum*, 48(5):473–481, 1997.

[6] B. Bhushan and B. K. Gupta. Coating deposition from vapor phase. In *Handbook of Tribology*, chapter 9. McGraw-Hill, Inc., 1991.

[7] D.M. Mattox. The historical development of controlled ion-assisted and plasma-assisted PVD processes. *Society of Vaccum Coaters,40th Annual Technical Conference Proceedings*, pages 109–118, 1997.

[8] R. F. Bunshah. *Deposition Technologies for Films and Coatings.* Noyes, New Jersey, 1982.

[9] D.M. Mattox. Fundamentals of ion plating. *Journal of Vacuum Science & Technology*, 10(1):47–52, 1973.

[10] D.M. Mattox. Ion plating. *Journal of the Electrochemical Society*, 121(3):110, 1974.

[11] D.M. Mattox. Recent advances in ion plating. *Japanese Journal of Applied Physics*, suppl.2(pt.1):443–450, 1974.

[12] D.M. Mattox. Surface effects in reactive ion plating. *Applied Surface Science*, 48-49:540–547, 1991.

[13] D.M. Mattox. Particle bombardment effects on thin-film deposition: a review. *Journal of Vacuum Science & Technology A*, 7(3):1105–1114, 1989.

[14] B. A. Movchan and A.V. Demchishin. Investigation of the structure and properties of thick vacuum- deposited films of nickel, titanium, tungsten, alumina and zirconium dioxide. *Fizika Metallov i Metallovedenie*, 28(4):653–660, 1969.

[15] P.J. Kelly and R.D. Arnell. Development of a novel structure zone model relating to the closed field unbalanced magnetron sputter system. *Journal of Vacuum Science and Technology A*, 16(5):2859–2869, 1998.

[16] R. Messier, A.P. Giri, and R.A. Roy. Revised structure zone model for thin physical structure. *Journal of Vacuum Science and Technology A*, 2(2):500–503, 1984.

[17] R. Behrisch. *Sputtering by Particle Bombardment I*, volume 47 of *Topics in Applied Physics.* Sringer-Verlag, Berlin Heidelberg New York, 1981.

[18] Weissmantel. Deposition of metastable films by ion beam and plasma techniques. *Proc. 9th. Int. Vacuum Congress and 5th. Conference on solid surfaces (Madrid)*, pages 229–308, September/October 1983.

[19] Mitsuharu Konuma. *Film Deposition by Plasma Techniques*, chapter 6. Physical Vapor Deposition Under Plasma Conditions, page 132. Atoms and Plasmas. Springer-Verlag Berlin Heidelberg, 1992.

[20] W.-D. Münz. The unbalanced magnetron: current status of development. *Surface & Caotings Technology*, 48:81–94, 1991.

[21] B. Window, F. Sharples, and N. Savvides. Magnetically confined sputter source with high ion-flux. *Journal of Vacuum Science and Technology A*, 3(6):2368–2372, 1985.

[22] J.Musil, S. Kadlec, and W.-D. Münz. Sputtering systems with magnetically enhanced ionization for ion plating of TiN films. *Journal of Vacuum Science & Technology A*, 8(3):1318–1324, 1990.

[23] J.Musil, S. Kadlec, and W.-D. Münz. Unbalanced magnetrons and new sputtering systems with enhanced plasma ionization. *Journal of Vacuum Science & Technology A*, 9(3):1171–1177, 1991.

[24] P.C. Johnson. The cathodic arc plasma deposition of thin films. *Physics of Thin Films*, 14:162, 1989.

[25] W.-D. Münz, D.B. Lewis, S. Creasey, T. Hurkmans, T. Trinh, and W. v Ijzendorn. Defects in TiN and TiAlN coatings grown by combined cathodic arc/unbalanced magnetron technology. *Vaccum*, 46(4):323, 330 1994.

[26] P. J. Martin. Coatings from the vacuum ARC. In R. L. Boxman, P. J. Martin, and D. M. Sanders, editors, *Handbook of Vacuum ARC Science and Technology*, page 393. Noyes Publications, 1995.

[27] P. J. Martin. Coatings from the vacuum ARC. In R. L. Boxman, P. J. Martin, and D. M. Sanders, editors, *Handbook of Vacuum ARC Science and Technology*, page 412 et seq. Noyes Publications, 1995.

[28] H.-J. Scheibe, B. Schultrich, R. Wilberg, and M. Falz. Laser-arc technology for industrial hard coating deposition. *Surface & Coatings Technology*, 97(1-3):410–413, 1997.

[29] B. Jüttner, V. F. Puchkarev, E. Hantzsche, and I. Beilis. Cathode spots. In R. L. Boxman, P. J. Martin, and D. M. Sanders, editors, *Handbook of Vacuum ARC Science and Technology*, page 260. Noyes Publications, 1995.

[30] I.G. Brown and X. Godechot. Vacuum-arc ion charge-state distributions. *IEEE Trans. Plasma Sci.*, 19:713–717, 1991.

[31] W.-D. Münz, D. Schulze, and F.J.M Hauzer. A new method for hard coatings: ABS (Arc bond Sputtering). *Surface and Coatings Technology*, 50(2):169–178, 1992.

[32] I.J. Smith, D. Gillibrand, J.S. Brooks, W.D. Münz, S. Harvey, and R. Goodwin. Dry cutting performance of HSS twist drills coated with improved TiAlN. *Surface and Coatings Technology*, 90:164–171, 1997.

[33] K.L. Mittal. Adhesion measurement of films and coatings: a commentary. In K.L. Mittal, editor, *Adhesion Measurement of Films and Coatings*, pages 1–13. VSP Utrecht, The Netherlands, 1995.

[34] R.C. Addison, M. Somekh, J.M. Rowe, and G.A.D. Briggs. Characterization of thin-film adhesion with the scanning acoustic microscope. In *SPIE International Symposium on Pattern Recognition and Acoustical Imaging*, volume 786, pages 275–284, 1987.

[35] H. Weiss. Adhesion of advanced overlay coatings: mechanisms and quantitative assessment. *Surface & Coating Technology*, 71:201–207, 1995.

[36] C. Bischof. *Adhäsion*, chapter 3, page 24. Akademie-Verlag Berlin, 1982.

[37] J. M. Howe. *Interfaces in Materials, Atomic Structure, Thermodynamics and Kinetics of Solid-Vapor,Solid-Liquid and Solid-Solid Interfaces.* John Wiley & Sons. Inc., 1997.

[38] J.K. Hirvonen and B.D. Sartwell. Ion implantation. In *ASM Handbook*, page 606. ASM International, 1994.

[39] G.K. Wolf, P. Engel, D. Heyden, E. Vera, and F. Stippich. Maßgeschneiderte Schicht-Interfacesysteme mittels ionenstrahlgetützter Beschichtung. *Mat.wiss. u. Werkstofftech.*, 29:518–524, 1998.

[40] H. Holleck. Material selection for hard coatings. *Journal of Vacuuum Science & Technology A*, 4(6):2661–2669, 1986.

[41] C. Tsai, J.C. Nehan, W.W. Gerberich, J. Heberlein, and E. Pfender. Diamond-metal composite coatings on cemented-carbide tools. *Diamond and related Materials*, 2:617–620, 1993.

[42] M. Cailler, G.H. Lee, P.J. Schultz, P.J. Simpson, and P. Perquin. The role of ion-induced damage in thin film adhesion strenght. *Journal of Adhesion Science and Technology*, 5(11):973–985, 1991.

[43] K. Koski, J. Hölsä, J. Ernoult, and A. Rouzaud. The connection between sputter cleaning and adhesion of thin solid films. *Surface and Coatings Tehnology*, 80, 195-199 1996.

[44] C. Liu, A. Leyland, S. Lyon, and A. Matthews. An a.c. impedance study on PVD CrN-coated mild steel with different surface roughnesses. *Surface & Coating technology*, 76-77:623–631, 1995.

[45] N.J.M. Carvalho, A.J. Huis int Veld, and J.Th. De Hosson. Interfacial fatigue stress in PVD TiN coated tool steels under rolling contact fatigue conditions. *Surface & Coatings Technology*, 105:109–116, 1998.

[46] Pan W.L., G.P. Yu, and J.H Huang. Mechanical properties of ion-plated TiN films on AISI D2 steel. *Surfcae and Coatings Technology*, 110(1-2):111–119, 1998.

[47] A.K.M.S. Chowdhury, D.C Cameron, and M.S.J. Hashmi. Adhesion of carbon nitride thin films on tool steel. *Surface & Coatings Technology*, 116-119:46–53, 1999.

[48] U. Helmerss on, B.O. Johanson, J.-E. Sundgren, H.T.G. Hentzell, and P. Billgren. Adhesion of titanium nitride coatings on high speed steel. *J. Vac. Sci. Technol. A*, 3(2):308–315, 1985.

[49] T. Bell, M.H., Sohi, J.R. Betz, and A. Bloyce. Energy beams in second generation surface engineering of aluminium and titanium alloys. *Scandinavian Journal of Metallurgy*, 19(5):218–26, 1990.

[50] A. Matthews, A. Leyland, B. Dorn, PR. Stevenson, M. Bin-Sudin, C. Rebholz, A. Voevodin, and J. Schneider. Plasma-based surface engineering processes for wear and corrosion protection. *Journal of Vacuum Science & Technology A*, 13(3):1202–1207, 1995.

[51] J. Walkowicz, J. Smolik, and K. Miernik. Investigation of the influence of ion etching parameters on the structure of nitrided case in hot working steel. *Surface & Coatings Technology*, 116-119:361–366, 1999.

[52] Y. Sun and T. Bell. The role of oxidation in the wear of plasma nitrided and PVD TiN coated steel. *Wear*, 166(1):119–125, 1993.

[53] B. Bücken, G. Leonhardt, R. Wilberg, K. Höck, and H.J. Spies. Direct combination of plasma nitriding and PVD hardcoating by a continuous process. *Surface and Coatings Technology*, 68:244–248, 1994.

[54] K. Hoeck, H.J. Spies, B. Larisch, G. Leonhardt, and B. Buecken. Wear resistance of prenitrided hard coated steels for tools and machine components. *Surface & Coatings Technology*, 88(1-3):44–49, 1997.

[55] H.-J., Spies, B. Larisch, and K. Hoeck. Optimisation of TiN hard coatings on prenitrided low alloy steels. *Surface Engineering*, 11(4):319–323, 1995.

[56] W.-D. Münz, G. Nayal, and I. J. Smith. PVD coatings designed for cold forging processes. *VDI Berichte*, (155):228–242, 2000.

[57] M. Zlatanovic, T. Gredic, A. Kunosic, N. Backovic, and N. Whittle. Substrate-induced changes of TiN and (Ti,Al)N coatings due to plasma nitriding. *Surface & Coatings Technology*, 63(1):35–41, 1994.

[58] Y.Sun and T. Bell. Plasma surface engineering of low alloy steel. *Materials Science & Engineering A*, 140:419–434, 1991.

[59] J. D'Haen, C. Quaeyhaegens, and L.M. Stals. Interface study of physical vapour deposition TiN coatings on plasma-nitrided steels. *Surface & Coating Technology*, 61:194–200, 1993.

[60] Xianting Zeng, Sam Zhang, and Joe Hsieh. Development of graded Cr-Ti-N coatings. *Surface and Coatings Technology*, 102:108–112, 1998.

[61] P. Gröning, S. Nowak, and L. Schlapbach. Surface modifications of nitrogen-plasma-treated stainless steels. *Applied Surface Science*, 64:265–273, 1993.

[62] D.A. Porter and K.E. Easterling. *Phase Transformations in Metals and Alloys.* Chapman & Hall, 1992.

[63] R. Becker. *Ann. Phys.*, 32:128, 1938.

[64] J.W. Chan and J.E. Hillard. *J. Chem. Phys.*, 28:258, 1958.

[65] J.H. van der Merwe. Crystal interfaces. part i. semi-ininite crystals. *Journal of Applied Physics*, 63(1):117–122, 1963.

[66] C. Quaeyhaegens, L. M. Stals, M. van Stappen, and L. de Schepper. Interface study of TiN- and Ti-TiN-coated stainless steel AISI 304 with asymmetric glancing angle X-ray diffraction and classical Bragg-Brentano X-ray diffraction. *Thin Solid Films*, 197:37–46, 1991.

[67] M. Van Stappen, B. Malliet, L. de Schepper, L. M. Stals, J. P. Celis, and J. Roos. Influence of a Ti intermediate layer on the properties of TiN coatings. *CEP Consultants*, pages 209–212, 1989.

[68] P. A. Steinmann and H. E. Hintermann. Adhesion testing by the scratch test method - the influence of intrinsic and extrinsic parameters on the critical load. *Thin Solid Films*, 154(1-2):333–349, 1987.

[69] A. J. Perry. Scratch adhesion testing of hard coatings. *Thin Solid Films*, 107:167–180, 1983.

[70] Per Hedenqvist and Sture Hogmark. Experiences from scratch testing of tribological PVD coatings. *Tribology International*, 30(7):507–516, 1997.

[71] S.J. Bull and D.S. Rickerby. Evaluation of coatings. In D.S. Rickerby and A. Mathews, editors, *Advanced Surface Coatings: a Handbook of Surface Engineering*, chapter 12. Blackie and Son Ltd, Glasgow, 1991.

[72] M. D. Drory and J. W. Hutchinson. Measurement of the adhesion of a brittle film on a ductile substrate by indentation. In *Proc. R. Soc. Lond. A*, volume 452, pages 2319–2341, 1996.

[73] E. R. Weppelmann, X.-Z. Hu, and M. V. Swain. Observations and simple fracture mechanics analysis of indentation fracture delamination of TiN films on silicon. In K.L. Mittal, editor, *Adhesion Measurement of Films and Coatings*, pages 217–230. VSP, 1995.

[74] B. Rother and D. A. Dietrich. Evaluation of coating-substrate interface strength by differential load feed analysis of load-indentation measurements. *Thin Solid Films*, 250:181–186, 1994.

[75] P. Weiss and M. W. Sigrist. Measurements of coating adhesion strengths by time-resolved interferometric monitoring of laser-induced spallation. *Nondestr. Test. Eval.*, 13:247–291, 1997.

[76] V. Gupta, J. Yuan, and A. Pronin. Recent developments in the laser spallation technique to measure the interface strength and its relationship to interface toughness with applications to metal/ceramic, ceramic/ceramic and ceramic/polymer interfaces. In K.L. Mittal, editor, *Adhesion Measurement of Films and Coatings*, pages 367–401. VSP, 1995.

[77] S. I. Rokhlin and T. E. Matikas. Ultrasonic characterization of surfaces and interfaces. *MRS Bulletin*, October 1996.

[78] H. Ollendorf, D. Schneider, T. Schwarz, G. Kirchhoff, and A. Mucha. A comparative study of the mechanical properties of TiN coatings using the non-destructive surface acoustic wave method, scratch test and four-point bending test. *Surface and Coating Technology*, 84:458–464, 1996.

[79] J.-W. He, B. C. Hendrix, N.-S. Hu, K.-W. Xu, T. Bell, Y. Sun, and K. Mao. Interfacial fatigue limit as measure of cyclic bonding stength of hard coatings. *Surface Engineering*, 12(1):49–54, 1996.

[80] J. Valli. A review of adhesion test methods for thin hard coatings. *J. Vac. Sci. Technol. A*, 4(6):3007–3014, 1986.

[81] D.S. Rickerby. A review of the methodes for the measurement of coating substrate adhesion. *Surface and Coatings Technology*, 36(1-2):541, 557 1988.

[82] S.J. Bull and D.S. Rickerby. A review of the methods for the evaluation of coating-substrate adhesion. *Materials Science and Engineering A*, 140:583, 592 1991.

[83] Verein Deutscher Ingenieure. Richtlinie 3198, 1992, Düsseldorf, Germany.

[84] H. Oettel and R. Wiedemann. Residual stresses in PVD hard coatings. *Surface and Coating Technology*, 76-77:265–273, 1995.

[85] C.V. Thompson. Structure evolution during processing of polycristalline films. *Annual Review of Materials Science*, 30:159–190, 2000.

[86] L.A. Donohue, I.J. Smith, W.-D. Münz, I.Petrov, and J.E. Greene. Microstructure and oxidation-resistance of $\mathrm{Ti_{1-x-y-z}Al_xCr_yY_zN}$ layers grown by combined steered-arc/ unbalanced-magnetron-sputter deposition. *Surface & Coatings Technology*, 94-95:226–231, 1997.

[87] L. A., Donohue, D. B. Lewis, W.-D. Münz, M. M. Stack, S. B. Lyon, H.-W. Wang, and D. Rafaja. The influence of low concentrations of chromium and yttrium on the oxidation behaviour, residual stress and corrosion performance of TiAlN hard coatings on steel substrates. *Vacuum*, 55(2):109–114, 1999.

[88] W.S. Choi, S.K. Hwang, and C.M. Lee. Microstructure and chemical state of $\mathrm{Ti_{1-x}Y_xN}$ film deposited by reactive magnetron sputtering. *Journal of Vacuum Science & Technology A*, 18(6):2914–21, 2000.

[89] M. Gebhardt. Epitaxy. In P. Hartman, editor, *Crystal growth: An introduction*. North-Holland Pbl. Co., 1973.

[90] J.E. Matthews (Ed.). *Epitaxial grwoth B*. Materials Science and Technology. Academic Press, 1975.

[91] International Centre for Diffraction Data. JCPDS PDF-2 database, version 2.14, 1987-1999.

[92] W. P. Pearson. *A Handbook of lattice spacings and structures of metals and alloys*. Pergamon Press, Oxford, 1958.

[93] U. Helmersson, J.-E. Sundgren, and J.E. Greene. Microstructure evolution in TiN films reactiveley sputter deposited on multiphase substrates. *Journal of Vacuum Science and Technology A*, 4(3):500–503, 1986.

[94] L. Hultman, H.T.G. Hentzell, J.-E. Sundgren, B.-O. Johansson, and U. Helmersson. Initial growth of thin TiN on different phases of High Speed Steel. *Thin Solid Films*, 124:163–170, 1985.

[95] L. Hultman, W.-D. Münz, J. Musil, S. Kadlec, I. Petrov, and J. E. Greene. Low-energy ($\sim 100eV$) ion irradiation during growth of TiN deposited by reactive magnetron sputtering: Effects of ion flux on film microstructure. *Journal of Vacuum Science and Technology A*, 9(3):434–438, 1991.

[96] G. Håkansson, L. Hultman, J.-E. Sundgren, J.E. Greene, and W.-D. Münz. Microstructures of TiN films grown by various physical vapour deposition techniques. *Surface & Coatings Technology*, 48:51–67, 1991.

[97] I. Petrov, P. Losbichler, D. Bergstrom, J.E. Greene, W.-D. Münz, T. Hurkmans, and T. Trinh. Ion assisted grwoth of $Ti_{1-x}Al_xN/Ti_{1-y}Nb_yN$ multilayers by combined cathodic arc/magnetron-sputter depsoition. *Thin Solid Films*, 302:179–192, 1997.

[98] W.-D. Münz, F.J.M Hauzer, and D. Schulze. A new concept for physical vapor-deposition coating combining the methods of arc evaporation and unbalanced-magnetron sputtering. *Surface and Coatings Technology*, 49(1-3):161–167, 1991.

[99] Inc. Burleigh Instruments. Metris2000 operating manual.

[100] M. C. Madden. Transmission electron microscopy for the determination of microstructure of thin films and interfaces. *Thin Solid Films*, 154:43–56, 1987.

[101] D. A. Muller and M.J. Mills. Electron microscopy: probing the atomic structure and chemistry of grain boundaries, interfaces and defects. *Materials Science and Engineering A*, 260:12, 28 1999.

[102] D. B. Williams and C. B Carter. *Transmission Electron Microscopy*, volume 3 Spectrometry. Plenum Press, 1996.

[103] R.F. Egerton. *Electron Energy Loss spectroscopy in the electron microscope.* Plenum Press, 2nd edition, 1996.

[104] A. J. Perry, J.A. Sue, and P. J. Martin. Practical measurements of the residual stress in coatings. *Surface and Coatings Technology*, 81:17, 28 1996.

[105] W.-D. Münz, Q. Luo, G. Robinson, I.J. Smith, and G. Veyssiere. Applications of nanolayers in dry high speed milling of steels. *Intersurface, St. Etienne*, February 2001.

[106] R. Behrisch and K. Wittmaack. *Sputtering by Particle Bombardment III*, volume 64 of *Topics in Applied Physics.* Sringer-Verlag, Berlin Heidelberg New York, 1991.

[107] Yu. P. Sharkeev, E. V. Kozlov, and A. N. Didenko. Defect structures in metals exposed to irradiation of different nature. *Surface & Caotings Technology*, 96:95–102, 1997.

[108] J.S. Brooks, J.L. Davidson, S.D. Forder, W.-D.Münz, and M. Larsson. A Mössbauer spectroscopy study of Ti-Fe interfaces produced by the PVD process. *Thin Solid Films*, 308-309:351–357, 1997.

[109] D. Hanzel, W. Meisel, and P. Gutlich. Study of Fe-Ti and Fe-TiN interfaces by conversion electron moessbauer spectroscopy. *Hyperfine Interfactions*, 69(1-4):807–810, 1991.

[110] D. Hanzel, W. Meisel, P. Griesbach, B. Navinsek, P. Panjan, and P. Gutlich. Conversion electron moessbauer characterization of Fe-Ti and Fe-TiN interfaces in dependence on pretreatments and bias voltage in physical vapor deposition. *Journal of Vacuum Science and Technology A*, 11(6):3034–3039, 1993.

[111] B.W. Zhang. Effect of alloying elements on the amorphous formation and corrosion resistance of electroless Ni-P based alloys. *Materials Science and Engineering A*, 281(1-2):286–291, 2000.

[112] B. Navinsek, S. Novak, and A. Zalar. Interface problem in metallurgical coatings. *Materials Science and Engineering*, A139:249–258, 1991.

[113] N. Eguchi, V.Grajewski, H.H. Uchida, and E. Fromm. Sputter cleaning of iron substrates and contamination of TiN coatings studies by in situ Auger electron

spectroscopy measurements in an ultahigh vacuum physical vapour deposition apparatus. *Materials Science and Engineering*, A139:345–351, 1991.

[114] S. J. Bull, P.R. Chalker, C.F. Ayres, and D.S. Rickerby. The influence of titanium interlayers on the adhesion of titanium nitride coatings obtained by plassma assisted chemical vapor deposition. *Materials Science and Engineering A*, 139:71, 78 1991.

[115] L. Guzman, M. Adamia, W. Gissler, S. Klosel, and S. De Rossi. Vapour deposited Zn-Cr alloy coatings for enhanced manufacturing and corrosion resistance of steel sheets. *Surface and Coatings Technology*, 125(1-3):218–222, 2000.

[116] L. Hultman, B.-O. Johansson, J.-E.Sundgren, Markert L.C., and J.E. Greene. Ar incorporation in epitaxial TiN films deposited by reactive magnetron sputtering in mixed Ar/$N_2$ discharges. *Applied Physics Letters*, 53(13):1175–1177, 1988.

[117] L. Hultman, J.E. Sundgren, L.C. Markert, and J.-E. Greene. Ar and excess N incorporation in epitaxial TiN films grown by reactive bias sputtering in mixed Ar/$N_2$ and pure $N_2$ discharges. *Journal of Vacuum Science and Technology A*, 7(3):1187, 1193 1989.

[118] C.W. Kimblin. Erosion and ionization in the cathode spot regions of vacuum arcs. *J. Appl. Phys.*, 44(7):3074–3081, 1973.

[119] C. Bergman. Ion flux characteristics in arc vapor-deposition of TiN. *Surf. Coat. Technol.*, 36:243, 255 1988.

[120] A. Anderes. Ion charge distributions of vacuum arc plasmas: The origin of species. *Physical Review E*, 55(1):969–981, 1997.

[121] J. Ziegler and J.A. Biersack. The stopping and ranges of ions in matter, 1985.

[122] P.D. Townsend, J.C. Kelly, and N.E. W. Hartley. *Ion implantation, Sputtering and their applications.* Accademic press London, 1976.

[123] C. Schönjahn, A.P. Ehiasarian, D.B. Lewis, R. New, W.-D. Münz, R.D. Twesten, and I. Petrov. Optimization of in-situ substrate surface treatment in a cathodic arc plasma: A study by TEM and plasma diagnostics. *J. Vac. Sci. Technol. A*, July/August 2001.

[124] P.J. Martin, R.P. Netterfield, and T.J. Kinder. Ion-beam deposited films produced by filtered arc evaporation. *Thin Solid Films*, 193:77–83, 1990.

[125] R. Behrisch. *Sputtering yield of single crystal targets*, chapter 5, page 219. Volume 47 of *Topics in Applied Physics* [17], 1981.

[126] L.Chen, M. Simmonds, S. Habesch, and J.M. Rodenburg. Crystal orientation effects on sputtering and depth resolution in GDOES. accepted for publication, 2000.

[127] H. Ljungcrantz, L.Hultman, J.-E. Sundgren, G. Håkansson, and L. Karlsson. Microstructural investigation of droplets in arc-evaporated TiN films. *Surface & Coatings Technology*, 63:123–128, 1994.

[128] M. I. Lembke, D.B. Lewis, and W.-D. Münz. Localised oxidation defects in TiAlN/CrN superlattice structured hard coatings grown by cathodic arc/unbalanced magnetron deposition on various substrate materials. *Surface and Coatings Technology*, 125(263-268), 2000.

[129] H.W. Wang, M.M. Stack, S.B. Lyon, P. Hovsepian, and W.-D. Münz. The corrosion behavior of macroparticle defects in arc-bond sputtered CrN/NbN superlattice coatings. *Surface & Coatings Technology*, 126:279–287, 2000.

[130] P.J. Martin, D.R. McKenzie, R.P. Netterfield, P. Swift, S.W. Filipczuk, K.H.Müller, C.G. Pacey, and B.James. Characteristics of titanium arc evaporation processes. *Thin Solid Films*, 153:91–102, 1987.

[131] I. Demidenko, N.S. Lomino, V.D.Ovcharenko, V.G. Padalka, and G.N.Polyakova. Ionization mechansim of reaction gas in vacuum-arc discharges. *ZHURNAL TEKHNICHESKOI FIZIKI*, 54(8):1534–1537, 1984.

[132] M. Kühn, R.Pintaske, and F. Richter. Optical emission spectroscopy in cathodic arc deposition. *IEEE Trans. Plas. Sci.*, 25(4):694–699, 1997.

[133] A.P. Ehiasarian. Current PhD project, Sheffield Hallam University.

[134] D.M. Mattox. Surface effects on the growth, adhesion and properties of reactively deposited hard coatings. *Surface & Coatings Technology*, 81(1):8–16, 1996.

[135] Pathikrit Bandyopadhyay. Periodic table. http://www.csrri.iit.edu/periodic-table.html.

[136] U. C. Oh and Jung Ho Je. Effects of strain energy on the preferred orientation of TiN thin films. *Journal of Applied Physics*, 74(3):1692–1696, 1993.

[137] J. Pelleg, L.Z. Zevin, S. Lungo, and N. Croitoru. Reactive-sputter-deposited TiN films on glass substrates. *Thin Solid Films*, 197(1-2):117–128, 1991.

[138] T. Czerwiec, K. Anoun, M. Remy, and H. Michel. Structural study of titanium nitride coating interfaces refalted to plasma diagnostics. *Materials Science and Engineering A*, 139:276–283, 1991.

[139] R.A. Andrievski, I.A. Anisimova, V.P Anisimov, V.P. Makarov, and V.P. Popova. Grain-size and recrystallization of TiN, ZrN, NbN and CrN alloyed and multilayer films. *Thin Solid Films*, 261(1-2):83–86, 1995.

[140] D.J. Eaglesham, J.E. Bower, M.A. Marcus, M. Gross, and S. Merchant. Microstructure of sputtered TiN on Al. *Applied Physiscs Letters*, 71(2):219, 221 1997.

[141] L. de Schepper, M. d'Olieslaeger, G. Knuyt, L.M. Stals, M. van Stappen, B. Malliet, J.P. Celis, and J.R. Roos. Initial growth and epitaxy of PVD TiN layers on austenitic steel. *Thin Solid Films*, 173(2):199–208, 1989.

[142] C. Schönjahn, L.A. Donohue, D.B.Lewis, and W.-D. Münz. Enhanced adhesion through local epitaxy of transition -metal nitride coatings on ferritic

steel promoted by metal ion etching in a combined cathodic arc/unbalanced magnetron deposition system. *Jornal of Vacuum Science and Technology A*, 18(4):1718, 1723 2000.

[143] E. Roman, J.L. Desegovia, A. Alberdi, J. Calvo, and J. Laucirica. Influenec of the temperature of the high speed steel substrate on the interface composition and adhesion of TiN hard coatings by cathodic arc. *Vacuum*, 43(5-7):685–687, 1992.

[144] E. Roman, J.L. Desegovia, A. Alberdi, J. Calvo, and J. Laucirica. Comparative study of the interface composition of TiN and TiCN hard coatings on high speed steel substrates obtained by arc discharge. *Journal of Materials Science and Engineering A*, 163(2):197–200, 1993.

[145] J.G. Han, S.S. Kim, H.J. Kim, D.J Kim, and I.S. Choi. The effect of arc ion pre-bombardment on the impact failure of TiN coating on Co-WC. *Surfcae and Coatings Technology*, 98(1-3):991–996, 1998.

[146] K. A. Bischof, L. Erikson, E. Harju, and A.S. Korhonen. The influence of Ti interlayers on the adhesion of PVD-TiN coatings on oxidized stainless steel substrates. *Surface and Coatings Technology*, 58(3):163–172, 1993.

[147] S.B. Kim, C.B. In, S.K. Choi, and S.S. Chun. The effects of metallic interlayer formation on the adhesion properties of PACVD films on tool steel. *Joural de Physique II*, 1(C2):609–616, 1991.

[148] H. Öttel. Growth related stress development in PVD hard coatings. presented at 4th Sheffield ABS days, July 1998.

[149] B.-J. Kim, Y.-C. Kim, and J.-J. Lee. The effect of $NH_3$ plasma pretreatment on the adhesion property of $Ti_{(1-X)}Al_XN$ coatings deposited by plasma-enhanced chemical vapor deposition. *Surface and Coatings Technology*, 114:85–89, 1999.

[150] W.-D. Münz, G. Nayal, and I.J. Smith. VDI berichte Nr. 155, 2000.

[151] D. Sheeja, B. K. Tay, S. P. Lau, X. Shi, J. Shi, Y. Li, X. Ding, E. Liu, and Z. Sun. Characterization of ta-c films prepared by a two-step filtered vacuum arc deposition technique. *Surface and Coatings Technology*, 127(2-3):246–250, 2000.

[152] M. Lembke. Current PhD project Sheffield Hallam University.

[153] H. Paritong. *Development of Nb based corrosion resistant PVD coatings.* PhD thesis, Sheffield Hallam University, February 2000.

[154] H. Paritong. Improvement of corrosion resistance of unbalanced magnetron deposited Nb coatings by high energy metal ion pretreatment. *Surface Engineering*, 15(2):144, 1999.

# List of Figures

# Appendix A

# Nb-ion bombardment for corrosion protection-initial results

## A.1 Introduction

The main part of this thesis was concerned with interfaces as they can be achieved in high temperature deposition processes (e.g. $T \geq 400°C$) with typical bias voltages of $U_s = 1200\,V$. However, for some applications such as decorative coatings substrate materials, that require much lower process temperatures are often used (e.g. for brass: $T \leq 230°C$). In that case the bias voltage must be decreased. Furthermore, it was shown previously that Nb-ion bombardment at ($U_s = 600\,V$) of stainless steel lead to an improved corrosion resistance ([153] and [154]. Therefore, the question arises if it is possible to protect other substrate materials by such a low bias voltage treatment. First results for low carbon steel and brass substrate are presented here. These results however, are not fully understood yet and require more detailed investigation. They are presented here to wake the awareness for the potential and problems of the use of low bias voltage Nb-ion bombardment for corrosion protection of substrate materials other than stainless steel.

## A.2 Experimental method

### A.2.1 Nb-ion treatment procedure

Polished brass, low carbon steel and stainless steel (stainless was used for reference) were cleaned before loaded to the deposition chamber. After pump down to $p \leq 6 \times 10^{-3}$ Pa the chamber was heated to 230°$C$ and then under vacuum cooled to 170°$C$. Nb-ion bombardment was performed using $\mathrm{U_s} = 600\,\mathrm{V}$ at $p_{Ar} = 6^{-2}$ Pa which lead to an temperature increase to 230°$C$ within 10 minutes. Therefore, Nb-ion bombardment was interrupted in order to allow cooling to 170°$C$ before Nb-ion bombardment was continued for another 10 minutes. The Nb-ion bombardment was followed by reactive UBM deposition of 100 nm CrN at 230°$C$.

### A.2.2 Potentiodynamic polarisation

Potentiodynamic polarisation measurements in a 3% NaCl solution open to air were performed to evaluate the corrosion resistance. In these measurements, the coated sample is polarised as the working electrode. The current $I$ is supplied to the working electrode via two auxiliary carbon electrodes in parallel (AE) placed on each side of the working electrode. The potential $E$ of the working electrode is measured with respect to the reference electrode and adjusted via the current to the nominal potential value $E_N$. A *saturated Calomel electrode* (SCE) was used in the

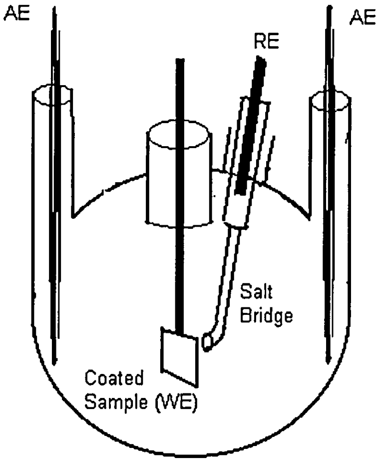

**Figure A.1:** Experimental setup for potentiodynamic polarisation measurements with AE: auxiliary carbon electrodes and RE: Reference electrode (from [153]).

experiments as the reference electrode, which was placed within 1 mm distance to the working electrode via a *Luggin probe.* The potential was increased continuously and the current i.e. current density was recorded as the dependent variable [153]. A schematic drawing of the experimental set up is shown in Figure A.1.

## A.3 Results & Discussion

Figure A.2 shows the surfaces of Nb-ion bombarded stainless steel (Figure A.2a), low carbon steel (Figure A.2b) and brass (Figure A.2c) substrates. The microstructure of the three interfaces is presented in Figure A.3. Figure A.3a shows the Nb-ion bombarded stainless steel in comparison to the Nb-ion bombarded low carbon steel (Figure A.3b) and the Nb-ion bombarded brass in Figure A.3c. Elemental profiles are shown in Figure A.4a-c for stainless steel, low carbon steel and brass, respectively.

### A.3.1 Stainless steel

The optical micrograph of the Nb-ion bombarded stainless steel (Figure A.2a) surface does not show any features that indicate material removal. Therefore, it is not surprising to find a Nb deposition layer in the elemental profile (Figure A.4a). This dense Nb deposition layer (see Figure A.3a) provides corrosion protection in a Cl ion containing medium. The sample shows signs of passivation in Figure A.5. Passivation is not found for the stainless steel sample Nb-ion bombarded at $U_s$= 1200 V, where the Nb is mainly intermixed with the steel.

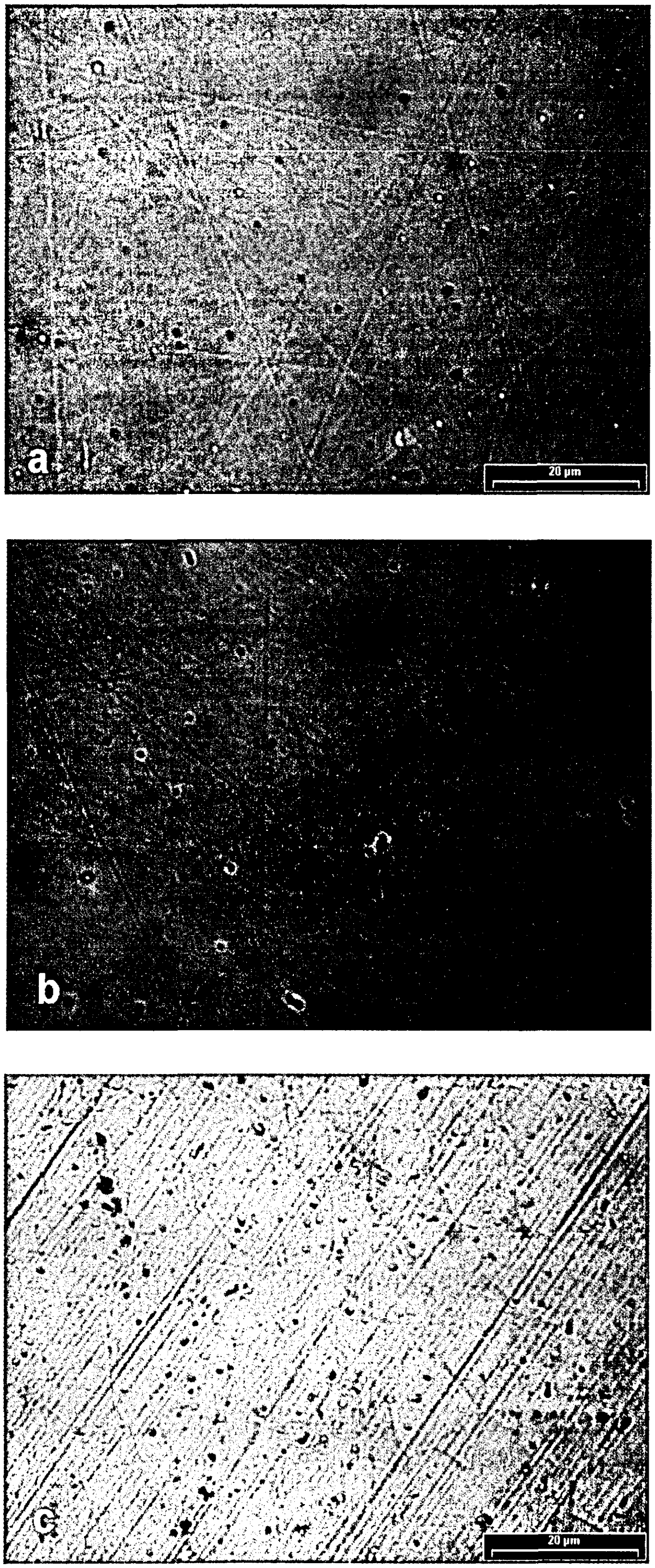

**Figure A.2:** Micrograph of Nb-ion bombarded substrates $U_s$= 600 V for 20 minutes: (a) stainless steel, (b) low carbon steel, and (c) brass.

**Figure A.3:** Interface microstructure after Nb-ion bombardment *Us*— 600 V for 20 minutes for various substrate materials: (a) stainless steel, (b) low carbon steel, and (c) brass.

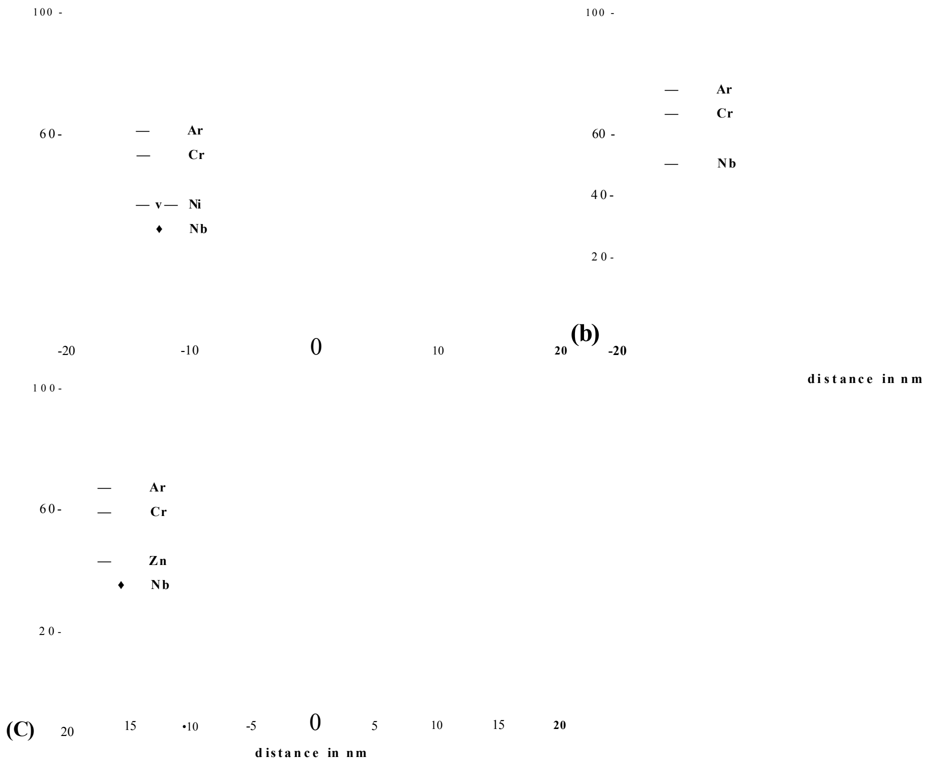

**Figure A.4:** Nb distribution across interface after Nb-ion bombardment at *Us* = 600 V for 20 minutes for various substrate materials: (a) stainless steel, (b) low carbon steel, and (c) brass.

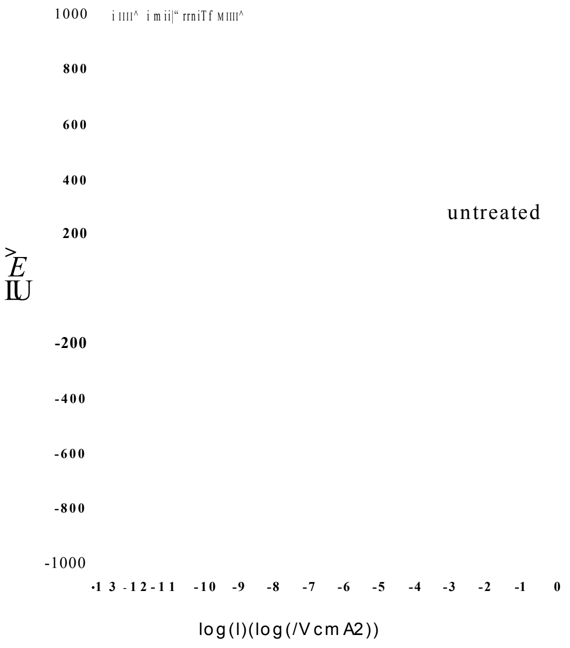

Figure A.5: Potentiodynamic polarisation curves for untreated stainless steel and Nb bombarded stainless steel at $U_s$= 600V and $U_s$= 1200 V, respectively.

## A.3.2 Low carbon steel

Despite the fact that the optical micrograph does not show any grain structure the Nb is not deposited as could be expected. Instead the Nb is intermixed with the steel as can be seen in Figure A.4b. This is surprising and can not be explained yet since the same bias voltage applied to a low carbon steel substrate during Cr ion bombardment lead to the formation of a deposition layer. However, the absence of a Nb deposition layer explains why the Nb ion bombardment does not result in an improved corrosion behaviour as can be seen from Figure A.6. Its behaviour is similar to that of the $U_s$= 1200 V Nb-ion bombarded sample, where Nb was also mainly intermixed with the steel but some indication of etching were found.

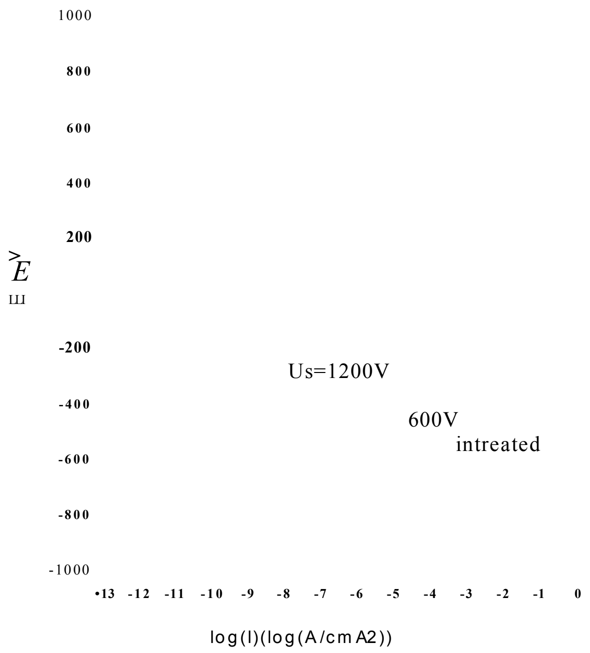

Figure A.6: Potentiodynamic polarisation curves for untreated low carbon steel and Nb-ion bombarded low carbon steel at *Us*= 600 V and *Us*= 1200 V, respectively.

## A.3.3 Brass

The Nb-ion bombarded brass interface exhibits low density regions that are visible in the under focused BF image in Figure A.3c. A well defined interfacial layer corresponding to a homogeneous high Nb concentration is not observed. The high Nb concentration in form of a deposition layer found in the elemental profile in Figure A.4c could be therefore rather localised. Thus, material removal is still possible explaining way grain boundaries are visible in Figure A.2c. At the same time the corrosion behaviour shown in Figure A.7 can be understood. Although there is no sign of passivation (due to the open structure of the Nb layer) the peak around —50 mV,corresponding to the formation of a protective layer of copper oxide, i.e. $CU_2O$ [153] is less pronounced. This could be explained by the fact that Cu is only exposed to the electrolyte where the Nb deposit has holes.

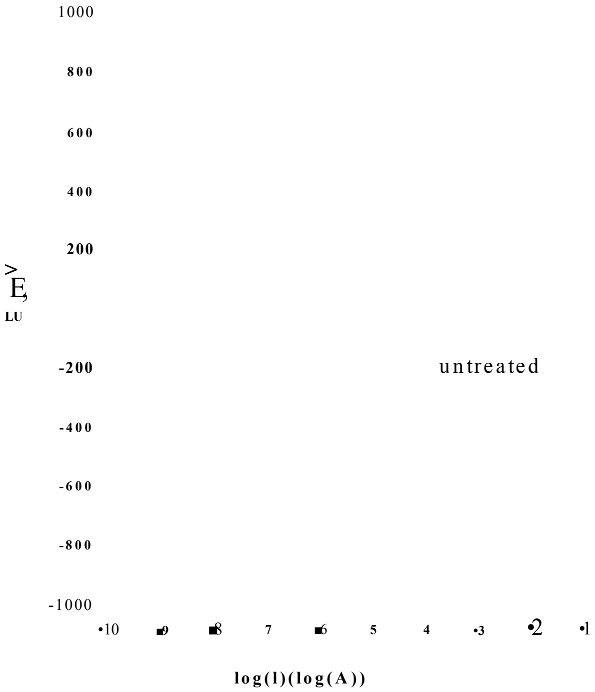

**Figure A.7:** Potentiodynamic polarisation curves for untreated brass and Nb-ion bombarded brass at *Us* = 600 V.

# Appendix B

# TEM sample preparation guide

## B.1 Preparation of cross-sections

Since it is often pointed out that TEM sample preparation is the main obstacle for TEM investigations the following Section is a step by step guide to the preparation of cross-sections. A 2.5 mm wide strip is cut from the centre region of a coated low carbon steel sheet using a precision saw fitted with a diamond wheel. A low feed rate should be used to avoid overheating and deformation of the sample . The centre part of this strip is than further cut into 0.3 mm thick slices. Two slices are fixed on a glass slide using crystal bond so that the coated sides face each other and are in contact (see Figure B.1).

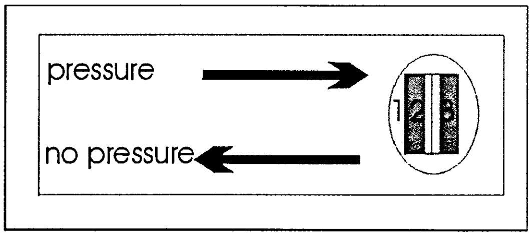

**Figure B.1:** TEM cross-section preparation: specimen (2) and protector (3) are fixed with crystal bond (1) so that coated surfaces (light gray) are in contact.

Care should be taken such that both slices stay in contact over the entire coated area during solidification of the crystal bond to ensure that the cross-section is indeed prepared parallel to the direction of the surface normal of the coating. This is important to avoid a decrease in lateral resolution for elemental profiling. The slice closer to the edge of the glass slide acts as protector and indicator for the remaining sample thickness during the grinding operation in which SiC grinding paper is used (final step grid 600). The sample is ground to a thickness of approximately 150 $\mu$m. To avoid coating delamination in case of coatings with poor adhesion pressure should be only applied during grinding when the glass slide is moved in such a manner that only compressive stress acts at the interface as shown in Figure B.1. The sample is polished using first a 3 $\mu$m diamond coated polymer pad and finally 1 $\mu$m. After each polishing step the integrity of the coated edge of the specimen should be checked by employing an optical microscope. If the coating is too thin to be seen by light microscopy the uncoated side of the specimen should be marked. Both, protector slice and specimen are removed from the class slide by warming up the crystal bond and than turned over simultaneously (protector and specimen stay in contact). To fix the slices on the glass slide more pressure is applied to the specimen such that its entire polished surface has contact with the glass slide while hardly any pressure is applied to the protector piece. This ensures that during final grinding and polishing of the second side when the specimen thickness and hence the crystal bond approaches 15 $\mu$m to 30 $\mu$m the protector piece detaches first from the glass slide while the specimen remains safely attached. The loss of the protector piece at the 600 grid SiC grinding stage usually indicates that the specimen thickness is in the range mentioned above. A thickness below 15 $\mu$m should be avoided because in this case the sample will curl at the coated side which does not allow effective ion beam milling. For samples which are known to be highly stressed or very loosely bonded to the substrate the final thickness should be in the range of 30 $\mu$m to 60 $\mu$m (Note that polishing with 3 $\mu$m and 1 $\mu$m does not reduce the sample thickness). To remove the specimen from the glass slide the remaining crystal bond is dissolved in acetone. When a filter paper is placed on the bottom of the beaker this can be used to lift the specimen, thus avoiding the use of tweezers. The specimen is placed onto a copper grid so that the coated edge is located approximately in the centre of the grid. It can be held in that position by putting the tip of curved tweezers on to one edge of the sample. The sample can be fixed with super glue. This can then be applied for example using a tooth stick which was cut with a razor plate in the shape of a pen nib. Care should be taken not to spill any glue over the coating. For ion beam milling in the GATAN PIPS 691 the copper grid is fixed on the holder and loaded so that the coated edge points away from the person loading it and is slightly of centre towards that person. This ensure for the above mentioned ion beam miller that sputtering takes place from the substrate side leaving the coating undamaged, when the single mode is selected. This means that while the sample rotates (360°) the gun is firing only when it is located roughly opposite to the coating. Then both guns can be used for Ar-ion bombardment from the top or the bottom. Best results (large transparent areas) are obtained when both guns where used from the same direction e.g. from the top (for typically 1 to 2 hours at 24 mA current) at ∓5°. Than both guns are used from the opposite side until the edge of the sample of the thinned region is just still visible as a line in a stereo microscope at highest magnification. Now the sample is close to electron transparency in that region and further thinning should involve both guns firing form opposite directions at ±5° until a small hole becomes visible. Usually the smaller the hole the larger the transparent area. Therefore observation in a light microscope every fife minutes is recommended.

## B.2 Preparation of samples for in plane imaging

An approximately $2 \times 2\,\mathrm{mm}$ square is cut by a diamond wheel from the central region of a low carbon sheet coated with no more than 100 nm TiAlN. The coated surface is fixed on a glass slide (middle) with crystal bond. The sample is ground on a flat surface from the substrate side to a thickness of about $30 - 40\,\mu\mathrm{m}$ and than polished as described above for cross-sections. Care should be taken that the sample thickness stays constant over the entire sample area. The sample is removed from the glass slide and placed in 50 % $H_2SO_4$ (concentration not very crucial) so that it is floating on the surface with the substrate facing the acid. After three to five hours the substrate is completely dissolved which can be seen when the sample curls and has a brown colour. A copper mesh is used to remove the film from the acid. Mesh and specimen are dipped into water to remove remaining acid. The sample will curl so that it needs to be put back on a copper mesh and dipped into IMS where it will uncurl. The film is caught on the copper mesh while in the IMS. When that mesh with the film is placed under a light microscope and transmitted light is used for observation the sample should be transparent exhibiting a brown colour. To avoid loss of the film in the TEM it is sandwiched between two mesh grids.

# Appendix C

# Publications

*Inst. Phys. Conf. Ser. No 161: Section 2*
*Paper presented at Electron Microscopy and Analysis Group Conf. EMAG99, Sheffield, 1999*

# Influence of $Cr^+$ and $Nb^+$ substrate sputter cleaning on the formation of $Ti_{1-x}Al_xN$/steel interfaces generated in a combined cathodic arc/unbalanced magnetron deposition system

**C Schönjahn[a], H Paritong[a], L A Donohue[a], W-D Münz[a], R D Twesten[b], and I Petrov[b]**

**[a]Materials Research Institute, Sheffield Hallam University, Howard Street, Sheffield S11WB UK,**
**[b]Fredrick Seitz Materials Research Laboratory University of Illinois, 104 South Goodwin Avenue, Urbana, Illinois 61801 USA**

ABSTRACT: The choice of arc cathode material (Cr or Nb) and the negative bias potential ($U_b$ = 400-1200 V) during metal ion etching of steel substrates prior to unbalanced magnetron sputter deposition of $Ti_{1-x}Al_xN$ (x=0.54) influences the microstructure and chemistry of the interface region as revealed by XTEM and STEM-EDX analysis. Cr ion bombardment at $U_b$=1200V results in Cr implantation profile with a net etching. Subsequent $Ti_{1-x}Al_xN$ growth exhibits local epitaxy with underlying substrate grains. Cr ion bombardment at $U_b$=400V and Nb at $U_b$ =1200V results in metal implantation and deposition. On such surfaces $Ti_{1-x}Al_xN$ shows a competitive growth with small column size and open boundaries.

## 1. INTRODUCTION

Substrate sputter cleaning is a key step in Physical Vapour Deposition controlling coatings adhesion, which is essential for any coating applications. Generally Ar ion bombardment in an Ar glow discharge plasma is carried out prior to sputter deposition by negatively biasing the substrates. Münz et al (1989) and Håkansson et al (1991) show that Ti metal ion etch in a cathodic arc discharge results in a structurally and compositionally modified layer within the substrates, which was correlated with the improved adhesion. Arc evaporation, however, produces rougher coatings compared to sputtering, due to macro particles, emitted from the cathode. To combine the advantages of metal ion etching with sputter-deposition, a coating system (HTC-1000-4) was developed, which incorporates four cathodes, each of which can be operated in both modes (Münz et al 1992). With four targets, the choice of the target material for ion etching is so no longer limited to the target material required for subsequent sputter deposition. High melting point and high vapour pressure materials can be used as target material in order to minimise number and size of macro particles deposited on the substrate surface during metal ion etching (Münz et al 1997 and Creasey et al 1997). Cr and Nb were found to be well suited in this respect, however, ion etching with the two elements may results in different interface architecture and coating adhesion because of differences in atomic mass, charge distribution and solubility in iron. Here we compare the microstructure and microchemistry of $Ti_{1-x}Al_xN$/steel interfaces formed by Cr and Nb ion bombardment at different bias voltages ($U_b$ = 400 -1200 V) analysed by XTEM and STEM-EDX. The efficiency of substrate material removal is also investigated by measuring the step generated during ion irradiation.

## 2. EXPERIMENT

The HTC 1000-4 system (Münz et al 1992) was equipped with Cr, Nb, and two $Ti_{0.5}Al_{0.5}$ targets. The process consists of pump down, heating and degassing at 400°C, followed by Cr or Nb ion etching at an arc current of 100A. To stabilise arc operation an Ar partial pressure of 6 x $10^{-4}$ mbar (Cr) and 8 x $10^{-4}$ mbar (Nb) was used. The substrate negative bias voltage $U_b$ during metal ion bombardment was varied in the range of 400 to 1200 V. A 100-nm-thick $Ti_{1-x}Al_xN$ (x=0.54 from RBS) was then deposited at 450°C with 8 kW DC power on each of the two $Ti_{50}Al_{50}$ targets at a rate of 10 nm/min. The Ar flow during deposition was 200 sccm, while $N_2$ flow was regulated using an integrating proportional differential controller to maintain a total pressure of 3.5 x$10^{-3}$ mbar. The microchemistry of the interface region in XTEM samples was investigated performing energy dispersive x-ray (EDX analysis) in a VG501 Scanning TEM using ~1nm-diameter electron beam. XTEM imaging was carried out in Philips CM20 equipped with $LaB_6$ filament, operated at 200kV. Substrates were partially covered with a mask during metal ion etching only and the resulting step was measured with a Laserform Talysurf stylus instrument.

## 3. RESULTS AND DISCUSSION

### *Cr ion bombardment*

Cr ion bombardment with $U_b$=1200 V for 20 min removes 90 nm of substrate material. STEM-EDX results, Fig. 1, shows that the Cr profile, with a FWHM of 5 nm, initially parallels the Fe signal at the interface then falls to background levels within a distance of 8 nm. The Cr depth distribution can be interpreted as dominated by ion implantation. Indeed, the projected range, R, for implantation and straggling, S, obtained from TRIM (Ziegler and. Biersack 1985), calculations for the maximum charge of $Cr^{3+}$ (Anders 1997) are 2.7 nm and 1.8 nm, respectively. With the thickness of the etched layer approximately two orders of magnitude larger than the ion range, implantation profiles can be approximated by error functions centred at a depth of R+S, i.e – 4.5nm in this case. The lateral resolution of the EDX analysis, which is factor determining apparent depth profiles, was estimated to be ±2.7 nm from the Al film signal. The Cr signal is, thus, consistent with an implantation profile convoluted with the depth resolution of the technique and, therefore, does not indicate the presence of substantial radiation enhanced diffusion.

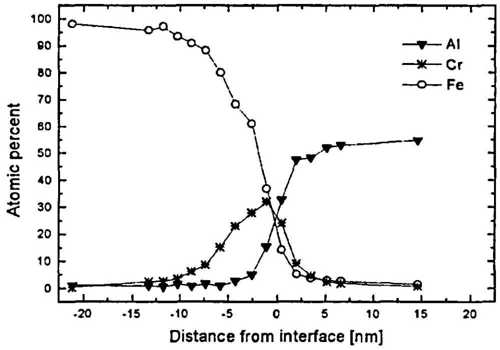

**Figure 1 Interface composition after Cr etch at Ub=1200V**

At $U_b$= 400 V no evidence of substrate removal was found by step measurements. The Cr-

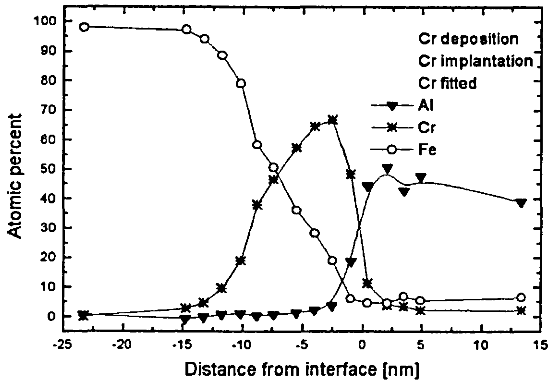

**Figure 2 Interface composition after Cr ion bombardment at Ub=400V**

profile in Fig 2 can be fitted to two components, indicating Cr enrichment in the substrate due to implantation and the presence of a Cr deposition layer. The presence of an overlayer suggests that the net sputtering rate is not high enough to compensate for film growth deposition from Cr atoms emitted by the cathodic arc. Note that the sputtering yields, obtained from TRIM simulations, with $U_b$= 400 V for $Cr^{2+}$ (1.4) and Ar+ (1.1) are a factor of two lower that the corresponding values with $U_b$ = 1200V: 2.8 and 2.4, respectively. Here we have taken the average charge of 2, measured for Cr arcs (Anders 1997).

The different surfaces obtained by Cr bombardment at various $U_b$ values result in different nucleation and coalescence behaviour in subsequent film growth carried out at identical conditions. The bright field XTEM image (Fig. 3(a)) of a sample pre-etched with $U_b$ = 1200 V, shows uniform contrast over large areas, consistent with local epitaxial growth of $Ti_{1-x}Al_xN$ on the clean steel surface as shown in more detail in Schönjahn et al. This growth mode is expected to be beneficial for adhesion as it maximises the bonding energy across the interface. In contrast, a competitive growth with small column size and open boundaries is observed at Ub= 400V as shown in Figure 3(b).

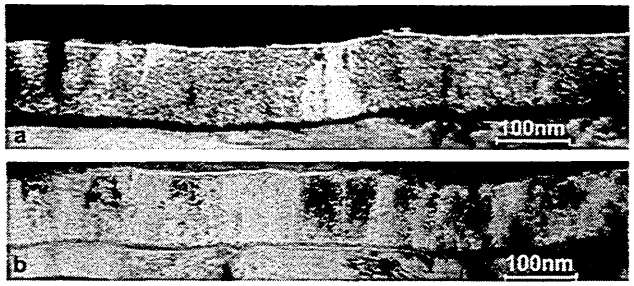

**Figure 3 XTEM BF images of $Ti_{1-x}Al_xN$ grown after Cr ion bombardment at Ub=1200V (a) and Ub=400V (b)**

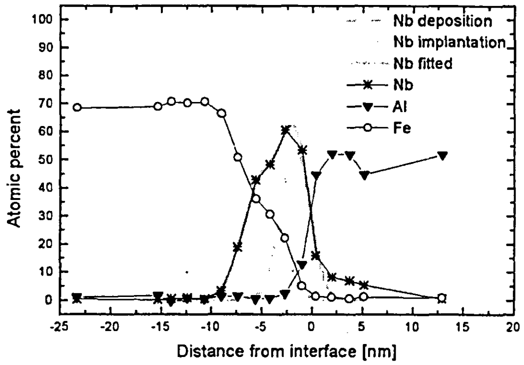

**Figure 4 Interface composition after Nb ion bombardment at Ub=1200V**

*Nb ion bombardment*

The employed step measurement technique was not sensitive enough to show measurable evidence of substrate material removal after Nb ion bombardment independent of the bias voltage. The shape of the Nb profile at $U_b$=1200 V is similar to the one obtained for Cr bombardment at $U_b$=400V, as shown in Figure 4. Again a two component fit was performed to account for a Nb deposition layer and an ion implanted region. The similarity of the Nb profile to the Cr etch at $U_b$=400V can be explained by similar low sputtering yield values (1.4) obtained from TRIM simulation assuming an average charge of $Nb^{3+}$. Interfaces generated after Nb bombardment at lower bias voltage show the same features. The $Ti_{1-x}Al_xN$ coating grown on the Nb layers exhibits competitive growth in analogy to the competitive growth observed on Cr deposition layers.

## 4. CONCLUSION

It is shown by XTEM and STEM-EDX that: substrate sputter cleaning can be achieved by Cr ion bombardment at $U_b$=1200V leading to local epitaxial growth of subsequently deposited $Ti_{1-x}Al_xN$. The formation of a metal deposition layer was observed in case of Cr ion bombardment at $U_b$=400V or for Nb ion bombardment for $U_b$=600V to $U_b$=1200. Metal ion implantation was observed for all cases. The formation of a metal layer hinders local epitaxial growth and leads to competitive growth of $Ti_{1-x}Al_xN$ . The best adhesion should be expected for $Ti_{1-x}Al_xN$ coatings deposited after Cr ion bombardment at $U_b$=1200V as local epitaxy maximises the interface bonding energy.

## REFERENCES

Anders A 1997 Phys. Rev. E **55** 969-981
Creasey S, Lewis D B, Smith I J and Münz W-D 1997 Surf. Coat. Techn **97** 163-175
Håkansson G, Hultman L, Sundgren J-E, Greene J E, Münz W-D 1991 Surf. Coat. Techn. **48,** 51
Münz W D, Schroeder J, Pechstein H, Håkansson G, Hultman L and Sundgren J-E 1989
Proc. SURTEC Berlin, A. Czichos and L G Vollrath (eds) (München:Hanser) p. 61
Münz W-D . Schulze D and Hauzer F J M 1992 Surf. Coat. Techn. **50** 169-178
Münz W-D, Smith I J, Lewis D B and Creasey S Vacuum **48** 473-481.
Schönjahn C, Donohue L A, Lewis D B, Münz W-D, Twesten R D and Petrov I unpublished
Ziegler J and Biersack J A 1985, The Stopping and Ranges of Ions in Matter (New York: Pergamon)

*Shortlisted*

# SUBSTRATE ION ETCHING IN COMBINED STEERED CATHODIC ARC–UBM DEPOSITION SYSTEM: EFFECTS ON INTERFACE ARCHITECTURE, ADHESION, AND TOOL PERFORMANCE

C. Schönjahn, D. B. Lewis, W.-D. Münz, and I. Petrov

*In PVD processes, substrate cleaning by ion etching prior to deposition is a key step in achieving good film adhesion, which is essential for all coating applications. The substrate surface is generally cleaned by bombarding it with metal or gas ions, extracted from a cathodic arc or glow discharge plasma respectively, by negatively biasing the substrate. This alters substrate surface chemistry, topography, and microstructure and affects subsequent film growth and adhesion. The present study involved Cr ion bombardment of steel and tungsten carbide at bias voltages* $U_b$ *of* $-600$ *and* $-1200$ *V as well as ion etching in an Ar glow discharge at* $U_b = -1200$ *V. Ion etching was followed by reactive unbalanced magnetron deposition of TiAlN based coatings. The microstructure and microchemistry of the interface region was investigated by XTEM and STEM–EDX analysis. After Ar ion pretreatment the presence of a low density substrate surface region was observed. This surface promotes the nucleation of randomly oriented grains leading to competitive growth with small column size and open boundaries. Interfaces generated after Cr ion bombardment at* $U_b = -600$ *V exhibit a local Cr deposition layer which leads also to competitive growth. In contrast, Cr ion bombardment at* $U_b = -1200$ *V results in the removal of around 100 nm of substrate material, providing a clean surface, and local epitaxial growth is observed. The different interface architecture is reflected by the critical loads obtained in scratch testing of 3·5 μm thick TiAlCrYN coatings deposited on tungsten carbide, ranging from 33 N for Ar bombardment to 141 N achieved by Cr ion bombardment at* $U_b = -1200$ *V. Cr ion pretreatment at* $U_b = -600$ *V results in a critical load of 68 N. The influence on the lifetime of coated tungsten carbide tools is also discussed.*

*Ms Schönjahn, Dr Lewis, and Professor Münz are at the Materials Research Institute, Sheffield Hallam University, Sheffield S1 1WB, UK and Professor Petrov is in the Frederick Seitz Materials Research Laboratory, University of Illinois, Urbana, IL 61801, USA.*

*Contribution to the 1999 Bodycote International Paper Competition.*

## INTRODUCTION

During the last decade tremendous progress in extending the lifetime of high quality cutting tools has been achieved by developing more sophisticated hard coatings. Today's most challenging market for hard coatings is in high speed machining, for both economic and environmental reasons.[1] In particular, dry high speed cutting reduces production costs in industrial countries dramatically.[2] Dry high speed cutting operations demand hard coatings with high oxidation resistance, high hardness, and low friction coefficient, particularly when tough materials such as die steels have to be machined. A previous paper reported on a new coating with the composition $Ti_{0{\cdot}43}Al_{0{\cdot}52}Cr_{0{\cdot}03}Y_{0{\cdot}02}N$, which met these requirements to a great extent.[3] In the present paper it is demonstrated that adhesion plays a major role in the performance of this specialised hard coating under severe cutting conditions. Fundamental investigations of the coating/substrate interface microstructure and microchemistry, together with adhesion measurements and cutting tests on coated tungsten carbide end mills in die steel, elucidate the intimate relationship between these parameters when tool life is paramount. The work focuses on analysis of the influence of bias voltage $U_b$ and ion species (Cr, Ar) on the properties of the coating/substrate interface. The interface generated by bombardment with multiply ionised Cr ions[4] extracted from a steered cathodic arc plasma is compared with that generated by ion bombardment with singly ionised Ar ions from a glow discharge plasma. The microstructure and microchemistry of the resulting coating/substrate interface are investigated by cross-sectional TEM and STEM–EDX. These results are correlated with experimental indentation and scratch measurement adhesion test results. The relationship between adhesion and tool performance in dry high speed cutting is determined by testing coated tungsten carbide tools in a modern Mazak milling centre.

## EXPERIMENTAL

All ion bombardment and coating deposition experiments were performed in a combined steered cathodic arc–unbalanced magnetron (CA–UBM) deposition system (Hauzer HTC 1000–4 ABS),[5] shown schematically in Fig. 1. The Cr target cathode is operated in the steered CA mode using the permanent magnets, which are shown in the withdrawn position ($B \approx 50$ G). For Ar bombardment and during all coating deposition, the TiAl and TiAlY target cathodes were used in UBM mode ($B \approx 300$ G),

ISSN 0267–0844

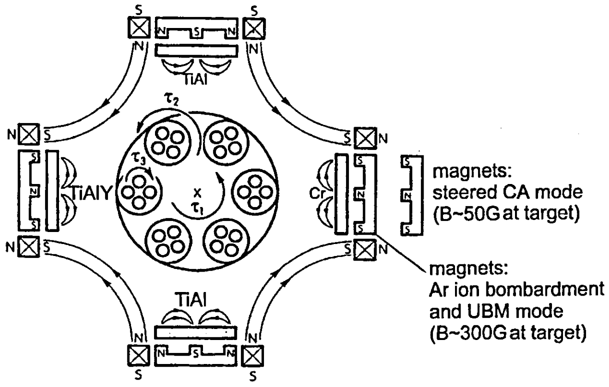

1 *Schematic cross-section of combined steered CA–UBM deposition system*

magnetically coupled to form a closed field and to achieve enhanced ionisation and a high substrate ion current density. To avoid contamination of the substrates with target material during ion bombardment, the targets were covered with moveable shutters. The substrates undergo three axis planetary rotation during ion bombardment as well as deposition. The average distance between the targets and the substrates is 25 cm.

The vacuum chamber was evacuated to a pressure of $6 \times 10^{-3}$ Pa and heated to a temperature of 400°C before any plasma experiments in order to minimise target poisoning resulting from adsorption of residual gases. The pumpdown and heating cycle is followed by a 20 min *in situ* ion bombardment step using the parameters summarised in Table 1. During this step the substrate temperature rises from 400 to 450°C owing to the ion bombardment. In the case of Ar ion bombardment and low bias voltage Cr ion bombardment additional radiant heating is required to maintain a temperature of 450°C. This temperature is kept constant during all TiAlN reactive deposition at a working gas pressure of 0·35 Pa (50:30 $Ar–N_2$ gas mixture). The target power on both TiAl and TiAlY targets was set at 8 kW. Unbalancing coils at a current of 6 A are used for increased ionisation and to improve control of the magnetic coupling. The bias voltage during UBM deposition has been optimised[6] at $U_b = -75$ V.

The experiments were carried out on two different substrates, low carbon steel and cemented carbide. Low carbon steel substrates were used for the ease of TEM specimen preparation and because they are Cr free (Cr would interfere with subsequent STEM–EDX profiling in the context of Cr ion bombardment). Specimens were polished to $R_a =$ 5 nm using 1 μm diamond paste. Substrates were cleaned in an automatic 10 station industrial cleaning line containing a range of aqueous based alkali detergents, rinsed in deionised water, and dried in a vacuum by radiant heating. Low carbon steel substrates were coated with 100 nm TiAlN (10 min duration), which serves as a base layer for TiAlCrYN.[7] STEM–EDX was used to determine the microchemistry in a dedicated FEG–STEM instrument (VG501) with a beam diameter of approximately 1 nm. All tungsten carbide substrates were wet cleaned, as described above, and then coated with a 300 nm TiAlN base layer (30 min) followed by a 3·2 μm layer of TiAlCrYN (210 min) so that tool and scratch tests could be carried out. The microstructure of these specimens was investigated using a Philips CM20 TEM equipped with a $LaB_6$ source and operated at 200 keV. Rockwell indentation tests (VDI standard 3198) and critical load measurements (scratch tests) using a CSEM Revetest instrument were carried out to assess adhesion strength. The critical load was defined as the lowest load at which adhesive failure was visible using reflected light microscopy.

**Table 1 Summary of substrate sputter cleaning parameters: etchant average charges from Ref. 4**

| Etchant | Operation mode | Ar pressure, Pa | Bias voltage, kV |
|---|---|---|---|
| $Ar^+$ | UBM (5 A coil current) | 0·6 | −1·2 |
| $Cr^{1·8+}$ | CA (100 A arc current) | 0·06 | −0·6 |
| $Cr^{1·8+}$ | CA (100 A arc current) | 0·06 | −1·2 |

A Mazak FJV-25 high speed machining centre was used to measure tool performance using A2 steel (58 HRC) as workpiece material under the following conditions: 8 mm diameter ball nosed solid carbide (Hydra-Marwin) end mill, 385 m $min^{-1}$ cutting speed (15 000 rev $min^{-1}$ spindle speed), 4 mm axial feed, 0·1 mm radial feed, 0·1 mm $rev^{-1}$ linear feed. Machining trials were stopped when the power on the spindle exceeded 10%, since higher power led to tool breakage. The time at which this condition is reached defines the tool life.

## RESULTS AND DISCUSSION

### Microchemistry of TiAlN/low carbon steel interface

The STEM–EDX profiles in Fig. 2 describe the microchemistry of three characteristic interfaces generated by ion bombardment with Ar (Fig. 2*a*), Cr at $U_b = -600$ V (Fig. 2*b*), and Cr at $U_b = -1200$ V (Fig. 2*c*). A simple interface structure characterised by a steep decrease in Fe concentration (substrate) and a corresponding steep increase in Ti and Al signal (coating) is revealed in Fig 2*a*. The apparent extent of the zone of intermixing between substrate and coating (>6 nm) is largely a result of the limited lateral resolution (±2·7 nm) of the STEM–EDX analysis. Higher resolution bright field imaging indicated that the interface is much sharper (about 3 nm) than it appears in Fig. 2*a*. The profile clearly shows an accumulation of Ar (5 at.-%) at the interface.

Using relatively low energy Cr ions ($U_b = -600$ V) a completely different result is obtained (Fig. 2*b*). Now the substrate material (Fe) and the coating material (Ti, Al) are clearly separated by a broad Cr peak. A detailed analysis leads to the conclusion that this peak may be resolved into two components. The peak on the substrate side is attributable to Cr implantation into the low carbon steel, whereas the component adjacent to the coating is due to Cr which has been deposited on top of the substrate and not resputtered during the ion bombardment process. The depth profile also clearly shows the incorporation of Ar (6 at.-%). The Ar peak is now located at a position exactly between the implanted and deposited Cr components. The analysis shows further that the coating is not deposited directly on the original substrate surface. In this special case a Cr interlayer with a well defined thickness (around 5 nm) is formed.

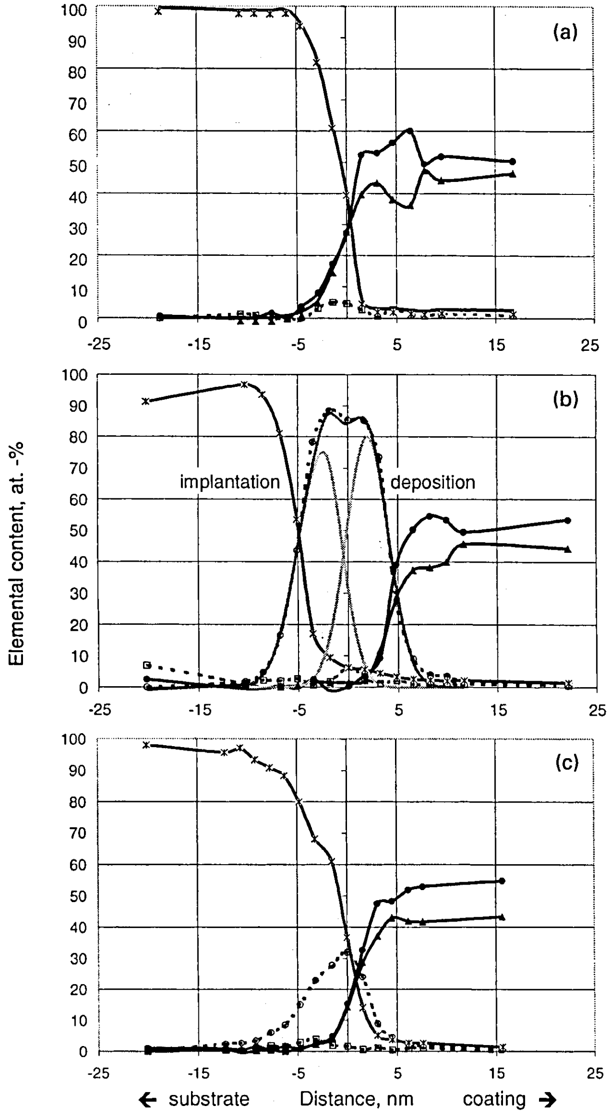

● Al; □ Ar; ▲ Ti; ○ Cr; ✳ Fe
*a* Ar ion bombarded low carbon steel, $U_b = -1200$ V; *b* Cr ion bombarded low carbon steel, $U_b = -600$ V; *c* Cr ion bombarded low carbon steel, $U_b = -1200$ V

2 *Cross-sectional STEM–EDX profiles across coating/substrate interface of given specimens*

Increasing the Cr ion energy by applying a higher bias voltage to the same level as for Ar bombardment leads to a third characteristic depth profile. Now the Cr peak intensity drops dramatically in comparison to the $U_b = -600$ V experiment (Fig. 2*c*). Pronounced penetration of Cr into the steel substrate is observed owing to Cr implantation (on the left of the graph). Consequently a much reduced Cr concentration at the interface has to be assumed. The apparent intermixing between substrate and coating elements is again attributable to the limited lateral resolution of the STEM–EDX analysis. Ar incorporation was also observed, but at a lower level (4 at.-%) than in the other two experiments. The reduced concentration of Cr and Ar at the interface may be attributed to the enhanced resputtering rate of the substrate material in comparison to the $U_b = -600$ V experiment.

## Interfacial microstructure

### *TiAlN/low carbon steel interface*

The distinctive influence of Ar and Cr ion bombardment on the interface microchemistry is accompanied by a change in appearance of the microstructure in the near interface region. The rather sharply defined interface after Ar ion bombardment as suggested by the depth profile results corresponds to a high contrast interface in the underfocused bright field image in Fig. 3*a*. The high contrast indicates the presence of gas inclusions at the interface, which correlates with the rather high Ar content in the STEM–EDX profile. In addition the initiation of competitive growth, typical for the growth of ceramic films on steel substrates,[8] can be observed. In Fig. 3*b* a much broader interface region is observed. The microstructure of the growing film is quite similar to that found after Ar ion bombardment. A chain of white spots (arrows) can be seen, indicating, as in the case of Ar bombardment, gas incorporation in the centre of the broad dark ribbon at the interface. The dark ribbon stems from the Cr deposit as discussed above for Fig. 2*b*. The existence of gas incorporation is confirmed by microchemical analysis. A substantial change in the microstructure of the interface and the growing film is shown in Fig. 3*c*, where the accelerating voltage of the Cr ions is −1200 V. Ar incorporation is only observed in the region of a dark grain in the centre of the image. Dark spots (arrows) are present in the overfocused bright field image, indicating the presence of Ar inclusions. In the two regions on the left and right of the dark grain in the centre of the image are large homogeneous areas of uniform diffraction bright field contrast. This phenomenon can be explained by local epitaxial growth, which is indicative of optimised adhesion.

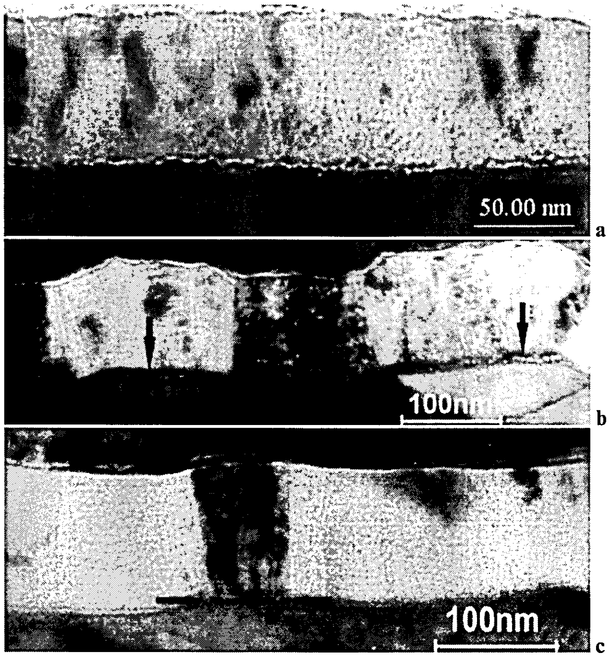

*a* Ar ion bombarded, $U_b = -1200$ V (underfocused); *b* Cr ion bombarded, $U_b = -600$ V (underfocused); *c* Cr ion bombarded, $U_b = -1200$ V (overfocused)

3 *Bright field images of TiAlN/low carbon steel interface of given specimens*

### *TiAlN/tungsten carbide interface*

In the case of tungsten carbide substrates, there is competitive growth typical for the case of Ar ion substrate cleaning, and this is shown in the dark field

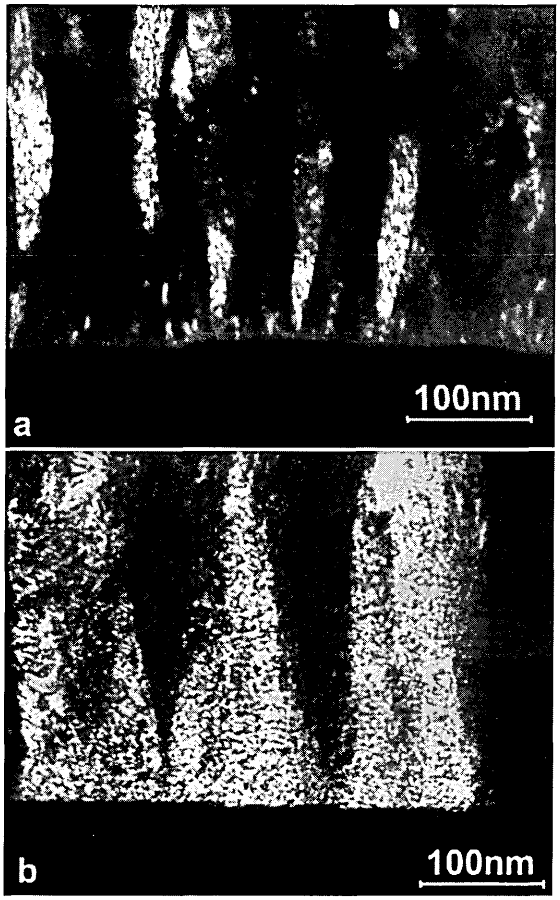

*a* Ar ion bombarded, $U_b = -1200$ V; *b* Cr ion bombarded, $U_b = -600$ V

4 *Dark field images of TiAlN/tungsten carbide interface of given specimens*

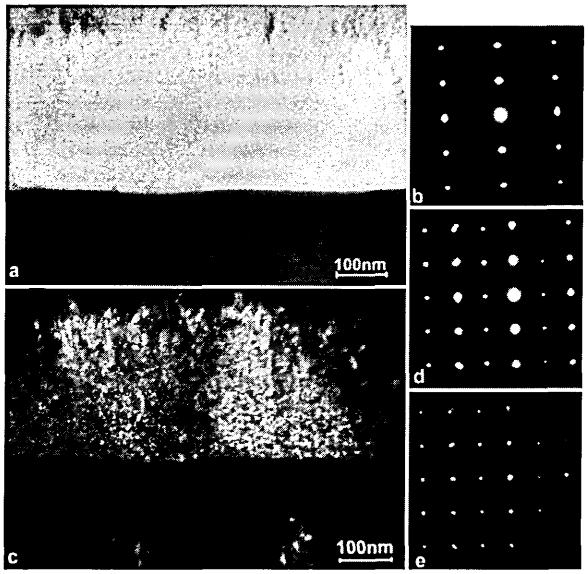

*a* bright field image; *b* SAD pattern of TiAlN grain; *c* dark field image; *d* SAD pattern with SA placed at interface to give superposition of TiAlN and tungsten carbide patterns; *e* SAD pattern of tungsten carbide grain

5 *Images of local epitaxial growth of TiAlN on tungsten carbide after Cr ion bombardment at $U_b = -1200V$*

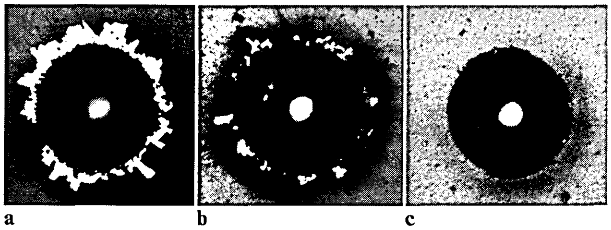

*a* Ar ion bombarded, $U_b = -1200$ V; *b* Cr ion bombarded, $U_b = -600$ V; (c) Cr ion bombarded, $U_b = -1200$ V

6 *Rockwell indentations on given specimens*

image of Fig. 4*a*. In the case of Cr ion bombardment with $U_b = -600$ V, competitive growth is observed, but with much larger grain sizes (Fig. 4*b*). Figure 5*a* shows a bright field image of the TiAlN/tungsten carbide interface (compare the TiAlN/low carbon steel interface of Fig. 3*c*). The dark field image in Fig. 5*c* confirms the existence of local epitaxial growth as it is much more sensitive with respect to changes in crystal orientation than bright field imaging. Conclusive evidence of local epitaxial growth is shown by the selected area diffraction (SAD) patterns. The SAD pattern for TiAlN (fcc) is shown in Fig. 5*b* and the pattern for a tungsten grain is shown in Fig. 5*e*. Figure 5*d* shows a superimposition of the TiAlN SAD pattern onto the pattern for the simple hexagonal lattice of a tungsten carbide grain. The exact match of the two diffraction patterns implies local epitaxial growth and therefore optimised adhesion.

## Adhesion measurements and tool performance

Microchemistry and microstructure results are complemented by adhesion measurements. Rockwell indentations reflect the influence of the interface properties on the adhesion of 3·5 µm TiAlCrYN coatings on tungsten carbide very well. The occurrence of spallation is reduced dramatically when we proceed from Ar, via low bias voltage Cr, to high bias voltage Cr ion bombardment, as shown in Fig. 6. In parallel, critical load measurements (scratch tests) show an increase from 33 N for Ar, to 68 N for Cr at $U_b = -600$ V, to 141 N for Cr ion bombardment at $U_b = -1200$ V. The strong correlation between interface microchemistry, microstructure, and adhesion data invites comparison with findings from studies of epitaxial growth. Coherent or semicoherent interfaces in the case of local epitaxial growth exhibit in general low interfacial energies of up to about 200 mJ m$^{-2}$ for purely coherent and 200–500 mJ m$^{-2}$ for semicoherent interfaces.[9] Interfaces with random orientation of the coating have higher interfacial energies, typically between 500 and 1000 mJ m$^{-2}$. Applying these values to the present work, Ar ion bombardment would be expected to result in high interfacial energies corresponding to weak adhesion and Cr ion bombardment should produce low interfacial energies, confirming the trend found in the adhesion test results.

Tool performance results are summarised in Fig. 7, in which a linear relationship can be observed between tool lifetime and critical load. It is important to emphasise that all tools were coated under identical conditions with a 300 nm thick TiAlN base layer followed by 3·2 µm TiAlCrYN. The ion bombardment conditions prior to coating deposition were varied to investigate the influence of adhesion on tool life. Further values of the bombardment parameters not discussed here were obtained by using two more ion

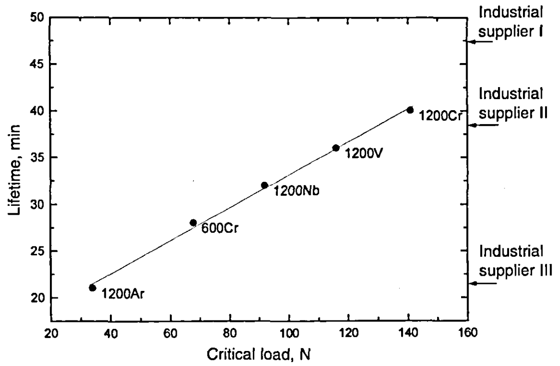

7 *Graph showing correlation between tool life and critical load values determined from same coating deposited after various sputter cleaning procedures, with comparison data for three commercially available hard coatings*

species, namely vanadium and niobium, both at $U_b = -1200$ V. To the best of the authors' knowledge this is the first published evidence that adhesion determined by critical load measurements directly controls the lifetime in high performance machining operations such as high speed cutting. To put the observed results in context, tool lives for three commercially available hard coatings are included in Fig. 7.

## CONCLUSIONS

The parameters used for ion bombardment prior to PVD coating deposition directly influence microchemistry, microstructure, adhesion, and coated tool performance: Ar etching at $U_b = -1200$ V leads to a low density interface region, resulting in competitive columnar growth with small column width, and critical load values around 33 N; Cr ion pretreatment at $U_b = -600$ V leads to a Cr deposit, resulting in competitive columnar growth with larger column width, and a critical load in the region of 68 N; and Cr ion pretreatment at $U_b = -1200$ V provides a clean substrate surface, where Cr is implanted and local epitaxial growth can occur, with a critical load of around 141 N. In dry high speed cutting operations in hardened A2 steel the lifetime of TiAlCrYN coated solid tungsten carbide ball nosed milling cutters is directly correlated with critical load values obtained from scratch testing.

## ACKNOWLEDGEMENTS

The authors would like to thank G. Robinson for performing the milling tests. The authors also acknowledge the technical assistance of Dr R. Twesten and the use of the facilities of the Center for Microanalysis, which is partially supported by DOE, at the University of Illinois. The STEM–EDX analysis was supported under contract DEFG02-ER9645439.

## REFERENCES

1. H. SCHULZ: Proc. 1st French–German Conf. on High Speed Machining, Metz, June 1997, 1.
2. T. CSELLE: Proc. 1st French–German Conf. on High Speed Machining, Metz, June 1997, 307.
3. I. J. SMITH, W.-D. MÜNZ, L. A. DONOHUE, I. PETROV, and J. E. GREENE: *Surf. Eng.*, 1998, **4**, 37.
4. I. G. BROWN, B. FEINBERG, and J. E. GALVIN: *J. Appl. Phys.*, 1988, **63**, 4889.
5. W.-D. MÜNZ, D. SCHULZE, and F. J. M. HAUZER: *Surf. Coat. Technol.*, 1992, **50**, 169.
6. I. J. SMITH: PhD thesis, Sheffield Hallam University, UK, 1998.
7. L. A. DONOHUE, I. J. SMITH, W.-D. MÜNZ, I. PETROV, and J. E. GREENE: *Surf. Coat. Technol.*, 1997, **94/95**, 226.
8. G. HÅKANSSON, J.-E. SUNDGREN, D. MCINTYRE, J. E. GREENE, and W.-D. MÜNZ: *Thin Solid Films*, 1987, **153**, 55.
9. D. A. PORTER and K. E. EASTERLING: in 'Phase transformations in metals and alloys', Chap. 3, 142–147; 1992, London, Chapman & Hall.

**Reprinted from**

SURFACE
& COATINGS
TECHNOLOGY

---

Surface and Coatings Technology 125 (2000) 66–70

# The interface between TiAlN hard coatings and steel substrates generated by high energetic $Cr^+$ bombardment

C. Schönjahn *, M. Bamford, L.A. Donohue, D.B. Lewis, S. Forder, W.-D. Münz

*Sheffield Hallam University, Materials Research Institute, Howard Street, Sheffield S1 1WB, UK*

ELSEVIER

## 2. Experimental procedure

Cr ion etching and coating deposition has been performed employing a combined CA/UBM deposition system [8] as shown in Fig. 1. The chromium cathode is operated in the CA mode during metal ion etching. For coating deposition the cathodes are coupled via electromagnetic coils to form a closed magnetic field and the $Ti_{0.5}Al_{0.5}$ targets are operated in the UBM mode. The substrates are undergoing three-fold rotation during substrate sputter cleaning and coating deposition (see Fig. 1 with $\tau_1 = 7.5$ rpm, $\tau_2 = 27$ rpm, $\tau_3 = 4.5$ rpm) and have an average distance of 250 mm from the targets. The chamber was evacuated to a pressure of $6 \times 10^{-5}$ mbar and heated to 400°C (measured with a thermocouple attached to a dummy substrate). The pump down and heating is followed by a Cr metal-ion bombardment. The etching of the substrate is carried out over a period of 20 min by biasing the substrates at $-1200$ V, $-1000$ V, $-800$ V or $-600$ V and operating the steered cathodic Cr arc at an arc current of 100 A. The Ar working pressure was kept at $6 \times 10^{-4}$ mbar for stable arc operation. During the Cr-ion etching step the substrate temperature is raised to 450°C either by high-energy ion impact at high bias voltages ($-1200$ V and $-1000$ V) or in the other cases additional radiant substrate heating. The temperature is kept constant by radiant substrate heating during TiAlN reactive deposition at a working gas pressure of $3.4 \times 10^{-3}$ mbar (50:30 Ar:$N_2$ gas mixture). The target power on both TiAl targets was set to 8 kW and the unbalancing coil current was 6 A. The bias voltage during coating growth is reduced to $-75$ V. UBM deposition has been performed for 10 min giving a coating thickness of ~100 nm in order to stay below the escape depth of conversion electrons used in Mössbauer spectroscopy.

The substrate material was mild steel ($25 \times 25 \times 0.7$ mm$^3$). All substrates were polished using 1 μm diamond paste in the final step resulting in a roughness $R_a = 5$ nm. The substrates were wet cleaned in an automatic 10 station industrial cleaning line containing a range of aqueous based alkali detergents, de-ionised water and vacuum radiant heating.

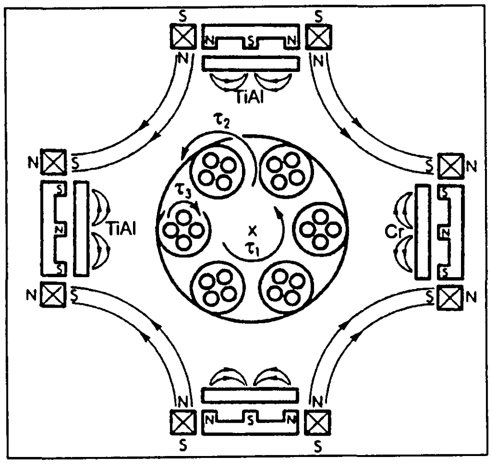

Fig. 1. Schematic drawing of the combined CA/UBM four-target deposition system.

The XTEM samples were prepared using a diamond saw to obtain $2 \times 0.5$ mm$^2$ slabs which were further thinned to 20 μm by mechanical polishing. The samples were mounted on a Cu slot grid and $Ar^+$ (5 keV, 16 mA, 5°) ion milled to electron transparency. The transmission electron microscopy has been carried out using a Philips CM20 microscope operated at 200 kV acceleration voltage. Chromium etched mild steel samples were studied using conversion electron Mössbauer spectroscopy in a gas flow proportional counter with an anode wire potential of 1500 V. A 25 mCu cobalt 57 radionuclide source in a rhodium matrix was placed on a Wissel velocity transducer, and data was collected by an EG&G ORTEC multi-channel analyser.

## 3. Results and discussion

### 3.1. Compositional changes of the substrate

The CEMS studies of the various etched samples show a reduction in relative counts when the bias voltage is reduced, showing that the overall coating thickness (TiAlN+Cr) is increased due to increasing chromium deposition. The effect of the etching process suggests the presence of the iron rich α-FeCr phase. As the bias voltage is decreased the amount of FeCr similarly reduces (see Table 1 and Fig. 2).

The presence of the FeCr phase is shown by the change in isomer shift $\delta$ and quadrupole interaction $\Delta E_Q$ (see Table 2) at the substrate surface.

For an untreated mild steel sample a symmetrical sextet with little or no quadrupole interaction would be expected. For Cr etched samples it was found that the line half-widths at half-maximum height were uneven, showing the presence of a second sextet at a similar position to the substrate.

The isomer shift becomes less negative showing a reduction in the 's' electron density at the iron nuclei coupled with an increase in electric field gradient shown by the increase in the quadrupole field. This represents

Table 1
Observed parameters of the substrate and interface for all bias voltages

| Bias voltage $U_b$ (V) | Relative area of FeCr to Fe (%) |
|---|---|
| −1200 | 16 |
| −1000 | 13 |
| −800 | 10 |
| −600 | 8 |

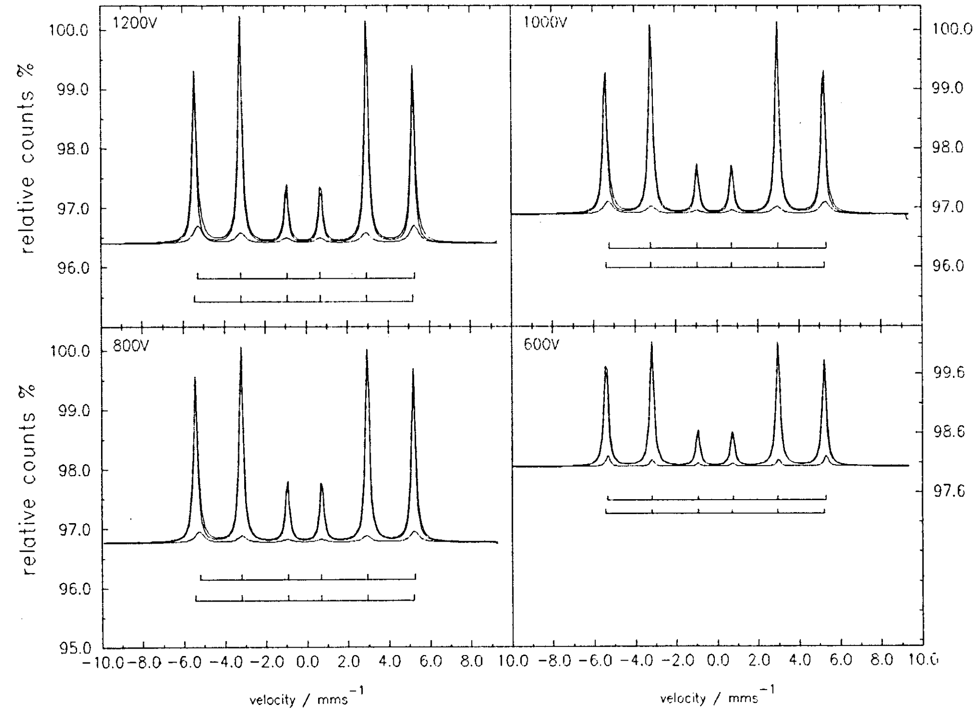

Fig. 2. Comparison of CEMS studies at varying bias voltages. The more intense sextet of mild steel substrate overlays the sextet of the interface region.

Table 2
Change in relative peak area of interface to substrate material for different bias voltage

| | Substrate steel | Interface material |
|---|---|---|
| $\delta$ (mm s$^{-1}$) | $-0.11 \pm 0.02$ | $-0.05 \pm 0.02$ |
| $\Delta E_Q$ (mm s$^{-1}$) | $0.00 \pm 0.01$ | $0.06 \pm 0.01$ |
| $H$ (T) | $33.0 \pm 0.1$ | $32.5 \pm 0.1$ |

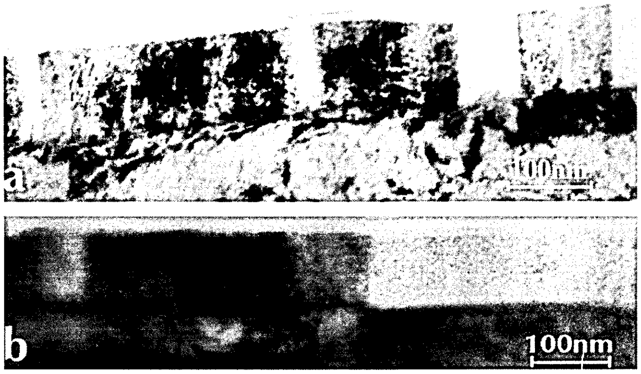

Fig. 3. Bias voltage during cathodic Cr arc: (a) $U_b = -800$ V; (b) $U_b = -1000$ V.

a change in the surroundings of the iron sites due to the presence of chromium. There is a slight reduction in the magnetic field strength $H$ also, showing the presence of Cr, since alloys of FeCr with high levels of Cr are paramagnetic as opposed to ferromagnetic iron. These parameters remain constant throughout the range of bias voltages showing that the same phase is formed each time although in smaller amounts at lower bias voltages.

### 3.2. Microstructure of the interfacial region

Figs. 3–5 show bright field images of the interfacial region for samples etched at different bias voltages. In Fig. 4(a) a typical interface region of a sample etched at a bias voltage of $-600$ V, taken in underfocused conditions, is shown so that regions of low-density material appear bright. These regions were only found for substrates etched at $-600$ V. Fig. 4(b) shows such an area at higher magnification. The dark layer presumably formed during the substrate cleaning varies in thickness considerably. CEMS suggests that this layer is a deposited chromium layer.

Fig. 5 presents the interface region for a bias voltage of $-1200$ V. In Fig. 5(c) evidence of removal of substrate material of ~100 nm is visible. The substrate beneath the droplet is ~100 nm thicker than the surrounding substrate, which was exposed to further ion impact indicating that an etch rate of at least 5 nm/min is obtained under these cleaning conditions. Therefore, the marked area in Fig. 5(f) can be identified as the modified substrate in contrast to the deposition layer in Fig. 4. Because of the similarity of Cr and Fe in the atomic mass (atomic number 24 and 26, respectively), the visible contrast is not attributed to atomic number but is believed to be due to local strain fields caused by

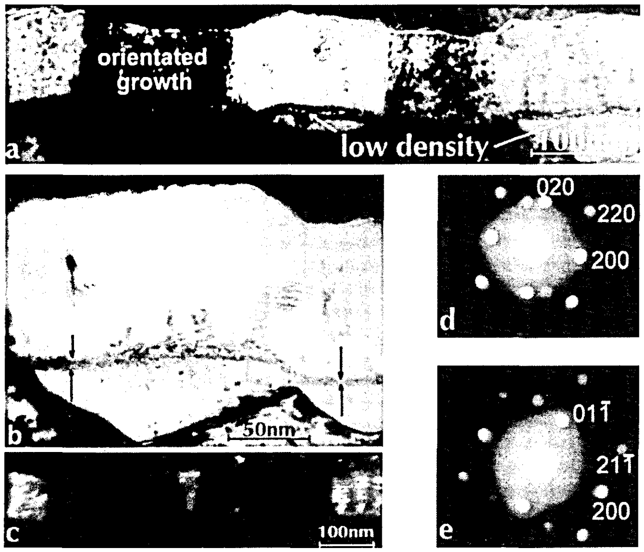

Fig. 4. Bias voltage during cathodic Cr arc $U_b = -600$ V: (a) bright field image (BF) (underfocused); (b) BF at higher magnification (overfocused); (c) dark field image (DF); (d) convergent beam diffraction pattern from TiAlN; (e) CEBD from steel substrate.

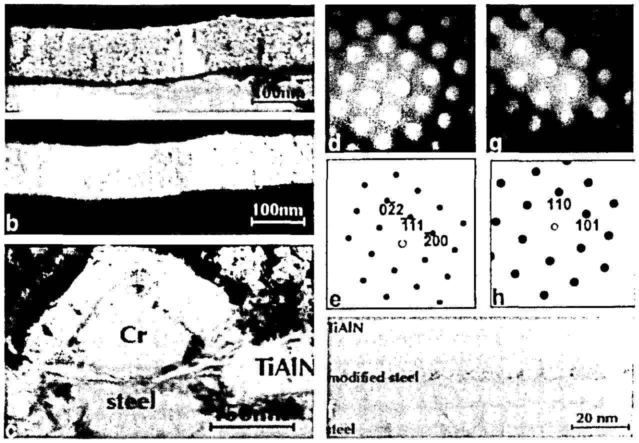

Fig. 5. Bias voltage during cathodic Cr arc $U_b = -1200$ V: (a) BF; (b) DF from (220) reflection; (c) BF showing droplet and protected steel; (d) CBED TiAlN; (e) schematic DP of TiAlN; (f) BF higher magnification; (g) CBED from steel substrate; (h) schematic DP of steel.

dislocation cores or defect clusters generated by highly energetic Cr ion impact. The thickness of the modified region was measured by XTEM imaging to be ~5 nm. TRIM [9] simulation assuming an acceleration potential of 1.2 kV applied to the Fe substrates and a maximum charge state of $Cr^{3+}$ [10] shows that target displacement events and vacancy production takes place in a depth of up to 6 nm.

Because the described surface modification due to metal ion etching leads to modified initial nucleation conditions, the microstructure of the TiAl coating is expected to be affected by the substrate pre-treatment. Indeed, an increase in grain size is found for high etching bias voltages as demonstrated in Fig. 3(a), (b) and Fig. 5(a). Here the grain boundaries of the coating match the grain boundaries of the substrate, as can most clearly be seen in Fig. 3(b). This indicates local epitaxial growth of the coating (fcc, $a = 0.417$ nm [11]) on the ferritic steel (bcc, $a = 0.286$ nm [12]). The dark field image taken from the (220) reflection shown in Fig. 5(b) demonstrates the large dimension of areas with the same orientation. In Fig. 5(d) and (g) convergent beam diffraction patterns (CBED) of the TiAlN coating and the steel substrate are presented, showing that the [011] zone axis of the coating is parallel to the $[\bar{1}11]$ zone axis of the steel substrate. This shows that although some damage has been induced in the substrate surface during the Cr ion bombardment, the crystallinity of the substrate surface is preserved so that local epitaxial growth can occur [bright almost structureless area in Fig. 5(b)].

In contrast the low etching bias voltage of $-600$ V gives rise to finer grain size as can be seen from Fig. 4(a) and (c). Porosity between the grains is observed. On some areas local orientated growth can still be observed. This is confirmed in Fig. 4(d) and (e) showing a [001] zone axis CBED pattern of the coating and a [011] CBED pattern of the underlying steel grain, respectively.

The presence of the above described film porosity can be avoided when the substrates are treated at higher bias voltages ($U_b = -800$ to $-1200$ V). It is thought that the improved nucleation conditions of a 'cleaner' substrate surface stimulate void free film growth in contrast to the possibly gas bubble containing Cr deposits as shown in Fig. 4(a) labelled 'low density'.

## 4. Conclusions

CEMS and XTEM investigations on ferritic steel samples coated with TiAlN after Cr ion bombardment at different bias voltages ($U_b = -600$ V, $-800$ V, $-1000$ V and $-1200$ V) have been carried out. Significant differences in substrate surface modification, such as substrate material removal for $U_b = -1200$ V (etching) and deposition of low density material for $U_b = -600$ V, have been observed. This led to substantial changes in microstructure of the subsequently grown TiAlN coating, ranging from columnar growth with an open structure for $U_b = -600$ V to local epitaxial growth at $U_b = -1200$ V. In the latter case an improved adhesion of the coating on the steel is expected. For verification thicker TiAlN coatings should be deposited in order to perform adhesion tests.

## References

[1] W.-D. Münz, J. Schroeder, H. Pechterstein, G. Håkansson, L. Hultman, J.-E. Sundgren, in: A. Czichos, L.G. Vollrath (Eds.), Proc. SURTEC, Berlin, Hanser, Munich, 1989, p. 61.

[2] G. Håkansson, L. Hultman, J.-E. Sundgren, J.E. Green, W.-D. Münz, Surf. Coat. Technol. 48 (1991) 51–67.

[3] I. Petrov, P. Losbichler, D. Bergstrom, J.E. Greene, W.-D. Münz, T. Hurkmans, T. Trinh, Thin Solid Films 302 (1997) 179–192.

[4] W.-D. Münz, I.J. Smith, D.B. Lewis, S. Creasey, Vacuum 48 (1997) 473–481.

[5] S. Creasey, D.B. Lewis, I.J. Smith, W.-D. Münz, Surf. Coat. Technol. 97 (1997) 163–175.

[6] Surface EngineeringASTM Handbook Vol. 51, ASTM International, Materials Park, OH, 1994, p. 558.

[7] J. Musil, J. Vyskocil, S. Kadlec, Physics of Thin Films 14 (1993) 79–144.

[8] W.-D. Münz, D. Schulze, F.J.M. Hauzer, Surf. Coat. Technol. 50 (1992) 169–178.

[9] J. Ziegler, J.A. Biersack, The Stopping and Ranges of Ions in Matter, Pergamon, New York, 1985.

[10] I.G. Brown, B. Feinberg, J.E. Galvin, J. Appl. Phys. 63 (1988) 4889–4897.

[11] I.J. Smith, D. Gillibrand, J.S. Brooks, W.-D. Münz, S. Harvey, R. Goodwin, Surf. Coat. Technol. 90 (1997) 164–171.

[12] G.V. Raynor, Metal Physics and Physical Metallurgy Vol. 4, Pergamon Press, Oxford, 1964, p. 125.

# Instructions for Authors

## Submission of Papers

Manuscripts (original and two clear copies) should be submitted to one of the Editors:

for authors in the Americas
**Dr. B. D. Sartwell,** Surface Chemistry Branch,
Naval Research Laboratory, Code 6170, Washington,
DC 20375, USA;

and for authors elsewhere
**Professor A. Matthews,** Director, The Research Centre in Surface Engineering, The University of Hull, Cottingham Road, North Humberside, HU6 7RX, UK.

Contributions are accepted on the understanding that the authors have obtained the necessary authority for publication. Submission of a manuscript implies that it is not under consideration for publication elsewhere.

## Types of contributions

— original papers
— invited or contributed reviews on specific topics
— brief communications on topics of immediate interest
— notices of meetings, symposia and short courses
— technical notes for "Current Industrial Practices" section

## Languages

Papers will be published in English. Both English and US spelling are permitted, provided that spelling is consistent within an article.

Authors in Japan please note that information about how to have the English of your paper checked, corrected and improved (*before submission*) is available from: Elsevier Science K.K., Editorial Service, 1-9-15 Higashi Azabu, Minato-ku, Tokyo 106-0044, Japan; Tel.: +81 3 5561 5032; Fax: +81 3 5561 5045.

## Manuscript preparation

Three copies of the manuscript should be submitted, in double-spaced typing on pages of uniform size with a wide margin on the left. The title page should be a separate sheet, bearing title, author(s)' name(s) and their full addresses, and a footnote with the corresponding author's Telephone, Fax numbers and E-mail Address.

Some flexibility of presentation will be allowed but authors are urged to arrange the subject matter clearly under such headings as Introduction, Experimental details, Results, Discussion etc. Each paper should have an abstract of 100–200 words.

References should be numbered consecutively (numerals in square brackets) throughout the text and collected together in a reference list at the end of the paper. Journal titles should be abbreviated according to the Chemical Abstracts Service Source Index, 1970 edition, and supplements. The abbreviated title should be followed by volume number, year (in parentheses) and page number.

## Submission of electronic text

The final text should be submitted on a 3.5 in or 5.25 in diskette (in addition to a hard copy with original figures). Double density (DD) or high density (HD) diskettes formatted for MS-DOS or Apple Macintosh compatibility are acceptable, but must be formatted to their capacity before the files are copied on to them. The files should be saved in the native format of the wordprocessing program used. Most popular wordprocessor file formats are acceptable. It is essential that the name and version of the wordprocessing program, type of computer on which the text was prepared, and format of the text files are clearly indicated.

## Illustrations

Line drawings and cyclic or aromatic formulae should be in a form suitable for reproduction. They may be drawn in black ink on drawing paper (letter height, 3–5 mm), but the use of good quality computer-generated figures is encouraged. They should preferably all require the same degree of reduction, and should be submitted on paper of the same size as, or smaller than, the main text to prevent damage in transit. Photographs should be submitted as clear black-and-white prints on glossy paper. Each illustration must be clearly numbered.

Illustrations can be printed in colour when they are judged by the Editor to be essential to the presentation. The publisher and the author will each bear part of the extra costs involved. Further information concerning colour illustrations and the costs to the author can be obtained from the publisher.

Legends to the illustrations must be submitted in a separate list.

All tables and illustrations should be numbered consecutively and separately throughout the paper.

## Proofs

Authors will receive proofs, which they are requested to correct and return as soon as possible. No new material may be inserted in the text at the time of proofreading. All joint communications must indicate the name and full postal address of the author to whom proofs should be sent.

## Further information

All questions arising after the acceptance of manuscripts, especially those relating to proofs, should be directed to: Elsevier Science Ireland Ltd. Elsevier House, Brookvale Plaza, East Park, Shannon, Co. Clare, Ireland. Tel.: +353 61 709609; fax: +353 61 709107.

The full and complete instructions to authors can be found on the World Wide Web: please visit our website which is accessible via the Elsevier Surfaces and Interfaces HomePage at http://www.elsevier.nl/locate/surfaces

## Offprints

Twenty-five offprints will be supplied free of charge to the author(s). Additional offprints can be ordered at prices shown on the offprint order form which accompanies the proofs.

# Enhanced adhesion through local epitaxy of transition-metal nitride coatings on ferritic steel promoted by metal ion etching in a combined cathodic arc/unbalanced magnetron deposition system

C. Schönjahn,[a] L. A. Donohue, D. B. Lewis, and W.-D. Münz
*Materials Research Institute, Sheffield Hallam University, Sheffield S11WB, United Kingdom*

R. D. Twesten and I. Petrov
*Fredrick Seitz Materials Research Laboratory University of Illinois, Urbana, Illinois 61801*

(Received 1 October 1999; accepted 6 December 1999)

*In situ* substrate cleaning by ion etching prior to deposition in physical vapor deposition processes is a key step in achieving good film adhesion, which is essential for all coating applications. Irradiation with metal or gas ions alters substrate surface chemistry, topography, and microstructure thus affecting subsequent film growth. This study compares $Ti_{1-x}Al_xN$/ferritic steel ($x=0.54$) interfaces formed after Cr ion bombardment at negative substrate biases, $U_s$, ranging from 600 to 1200 V during a Cr cathodic arc discharge, stabilized with a 0.06 Pa Ar background pressure. Samples biased with $-1200$ V in an Ar glow discharge at a pressure of 0.6 Pa were also investigated. Microstructure and microchemistry of the interfaces was studied by scanning transmission electron microscopy with energy dispersive x-ray analysis using cross-sectional samples. Cr ion etching with $U_s=1200\,\mathrm{V}$ resulted in a net removal of over 100 nm of substrate material with the formation, through implantation, of a Cr-enriched near-surface region extending to a depth of $\sim$10 nm. As $U_s$ was reduced to 600 V, Cr accumulated at the surface as a $\gtrsim$5 nm thick layer. Ar was incorporated at the surface to levels of 4–6 at. % during both Cr arc and Ar glow discharge etching. The microstructure of $Ti_{1-x}Al_xN$ overlayers was dramatically affected by pretreatment procedures. Ar sputter cleaned steel surfaces ($U_s=1200\,\mathrm{V}$) promote nucleation of randomly oriented grains leading to a competitive column growth with small column size and open boundaries. In contrast, Cr irradiation at the same bias voltage results in local epitaxial growth of $Ti_{1-x}Al_xN$ on steel and lead to a superior performance in scratch testing compared to coatings deposited after Cr treatment with $U_s=600\,\mathrm{V}$ or Ar ion bombardment at $U_s=1200\,\mathrm{V}$. Critical loads were 63, 47, and 27 N, respectively. © *2000 American Vacuum Society.*
[S0734-2101(00)01804-2]

## I. INTRODUCTION

Substrate sputter cleaning is performed prior to coating deposition in order to remove surface contaminants and oxide layers. Ions are extracted from a plasma by negatively biasing the substrate at bias voltages in the range of 200 V to 1.5 kV.[1] In sputter deposition or e-beam evaporation systems Ar ions are usually extracted from an Ar glow discharge and used for substrate cleaning, whereas in arc deposition sysems the metal-ion-containing plasma generated by the arc serves as an ion source. In the case of sputter cleaning using a Ti arc it was shown that the Ti ion implantation and radiaion damage enhanced diffusion takes place leading to a graded interface resulting in an enhanced adhesion.[1–3] This observation led to the development of a combined cathodic arc/unbalanced magnetron (CA/UBM) deposition system in order to join the excellent adhesion promoted by metal ion modification of the substrate surface with the versatility of material selection offerred by the magnetron source and the elimination of macroparticle generation during deposition.[4] It was found later[5] that the microstructure and microchemistry of interfaces generated by this combined technology strongly depend on the target material used for metal ion etching. Local epitaxial growth of B1–NaCl–structure transition metal nitride coatings on ferritic bcc steel substrates, which is potentially attractive for maximizing interfacial adhesion, was observed for TiAl cathode arc etching indicating that a relatively clean growth surface with well preserved crystalline order has been achieved. The presence of heavier and more energetic Nb-ions during the $Ti_{0.85}Nb_{0.15}$ cathode arc etching led to the formation of an amorphous interface layer and subsequent competitive columnar growth.[5] Another factor when choosing the best cathode material for substrate arc etching is the generation of macroparticles, which produce defects in subsequent film growth. Previous investigations have shown that high melting point metals, which also have high vapor pressure, should be used as etching materials in order to minimize the number and size of macroparticles.[6,7] Thus, Cr with its medium atomic mass (lighter than Fe), relatively high melting point, and extremely high vapor pressure[8] is attractive for use in metal ion etching and is the subject of this study. Cathodic arcs emit a mixture of multiply ionized metal ions and neutral atoms. The bias voltage accelerating the ions to the substrate is a crucial parameter in the cleaning process since high ion energies may cause sub-

---

[a] Electronic mail: schonjahn@shu.ac.uk

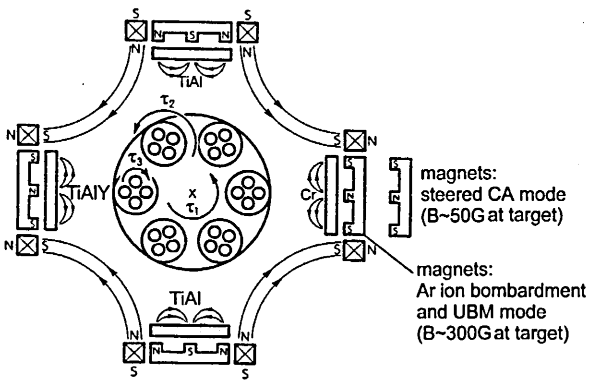

FIG. 1. Schematic cross section of the combined CA/UBM four-target deposition system.

stantial resputtering whereas low ion energies will result in metal deposition rather than substrate sputter cleaning.[9]

In the present study $Ti_{1-x}Al_xN$/steel interface regions formed by UBM deposition carried out after Cr- or Ar-ion bombardment are investigated. The influence of the bias voltage (600–1200 V) during steered cathodic arc Cr-ion bombardment on the interface region was studied. We find that Cr etch with 1200 V promotes local epitaxy on underlying substrate grains that results in significantly improved coating adhesion.

## II. EXPERIMENT

The experiments were performed in a combined CA/UBM deposition system shown schematically in Fig. 1. The Cr cathode is operated in the steered CA mode during sputter cleaning with the permanent magnets in a withdrawn position ($B = 50$ G). For $Ar^+$ sputter cleaning the cathodes are used in the UBM mode ($B = 300$ G) with the magnetic field lines coupled to form a closed magnetic field and to achieve enhanced ionization resulting in a high ion current to the substrate. To avoid cross contamination, the targets are covered with shutters during sputter cleaning. The substrates are undergoing three-axis planetary motion during substrate sputter cleaning and deposition at an average distance from the targets of 25 cm.

The chamber was evacuated to a pressure of $6 \times 10^{-3}$ Pa and heated to 400 °C (measured with a thermocouple attached to a dummy substrate). *In situ* sputter cleaning was then carried out for 20 min with the parameters summarized in Table I. During this step the substrate temperature is raised to 450 °C by Cr-ion bombardment with $U_s = 1200$ V. For Ar- and Cr-ion bombardment at lower bias voltages additional radiant heating was required to reach 450 °C. $Ti_{1-x}Al_xN$ films are deposited at the same temperature at a working pressure of 0.35 Pa (50:30Ar:$N_2$ mixture). The target power on both TiAl targets was 8 kW and bias voltage during growth −75 V. Deposition time was 10 min giving a coating thickness of ~100 nm. The substrates, low carbon ferritic [body centered cubic (bcc)] steel (25 mm × 25 mm × 0.7 mm), were polished using 1 μm diamond paste in the final step resulting in a surface roughness $R_a$ = 5 nm, then wet cleaned in an automatic ten station industrial cleaning line containing a range of aqueous based alkali detergents, deionized water and dried by vacuum radiant heating.

TABLE I. Parameters for substrate sputter cleaning pretreatment.

| Etchant and average charge (Ref. 12) | Operation mode | Ar pressure (Pa) | Bias voltage (kV) |
|---|---|---|---|
| $Ar^+$ | UBM: 5 A coil current | 0.6 | 1.2 |
| $Cr^{1.8+}$ | CA: arc current 100 A | 0.06 | 0.6 |
| $Cr^{1.8+}$ | CA: arc current 100 A | 0.06 | 1.2 |

Samples for transmission electron microscopy (TEM) observation were cut to slices and mechanically thinned to 20 μm and mounted on Cu grids. Argon ion beam milling (5 keV, 15 mA, 5°) was carried out from the substrate side only. The coating was protected against redeposition in the ion miller in case of in plan-view samples. The microchemistry was investigated performing energy dispersive x-ray (EDX) analysis in a VG5.01 scanning transmission electron microscope (STEM). The electron beam was focussed to ~1 nm diameter. The takeoff angle for x-ray collection was 40°. Quantification of the data was done using the ISIS software assuming a sample thickness of 50 nm.

Coating adhesion was assessed by scratch tests performed on coatings consisting of a ~300 nm $Ti_{1-x}Al_xN$ base layer, deposited at the conditions described above, and ~3.2 μm thick $Ti_{0.44}Al_{0.53}Cr_{0.03}Y_{0.02}N$ coating. CSEM REVETEST scratch tester was used. The critical load is defined as the first occurrences of adhesive failure determined by reflected light microscopy.

## III. RESULTS AND DISCUSSION

### A. Substrate surface modification

Figure 2 shows bright field cross-sectional transmission electron microscopy (XTEM) micrographs of the film/substrate area of samples prepared with Cr arc etch with $U_s = 600$ V [Figs. 2(a) and 2(b)], $U_s = 1200$ V [Figs. 2(c), 2(d), and 2(f)] and with the Ar discharge etch [Fig. 2(e)]. In all cases a modified layer is present at the interface with a thickness of several nanometers. In the case Cr-600 V etch, on top of some substrate grains, the modified layer exhibits a phase contrast (contrast change by going through focus) indicating the presence of a low density material. This is evident in most of the interface region shown in Fig. 2(a) and also in region 1 in Fig. 2(b). In other areas a dense but thinner interfacial layer is observed labeled with 2 in Fig. 2(b). Overall the coating in this sample as well as the Ar etched sample presented in Fig. 2(e), exhibits a relatively small column size, approximately 50–150 nm, with less dense column boundaries. In contrast the coating deposited on a substrate etched in a Cr arc with $U_s = 1200$ V shows

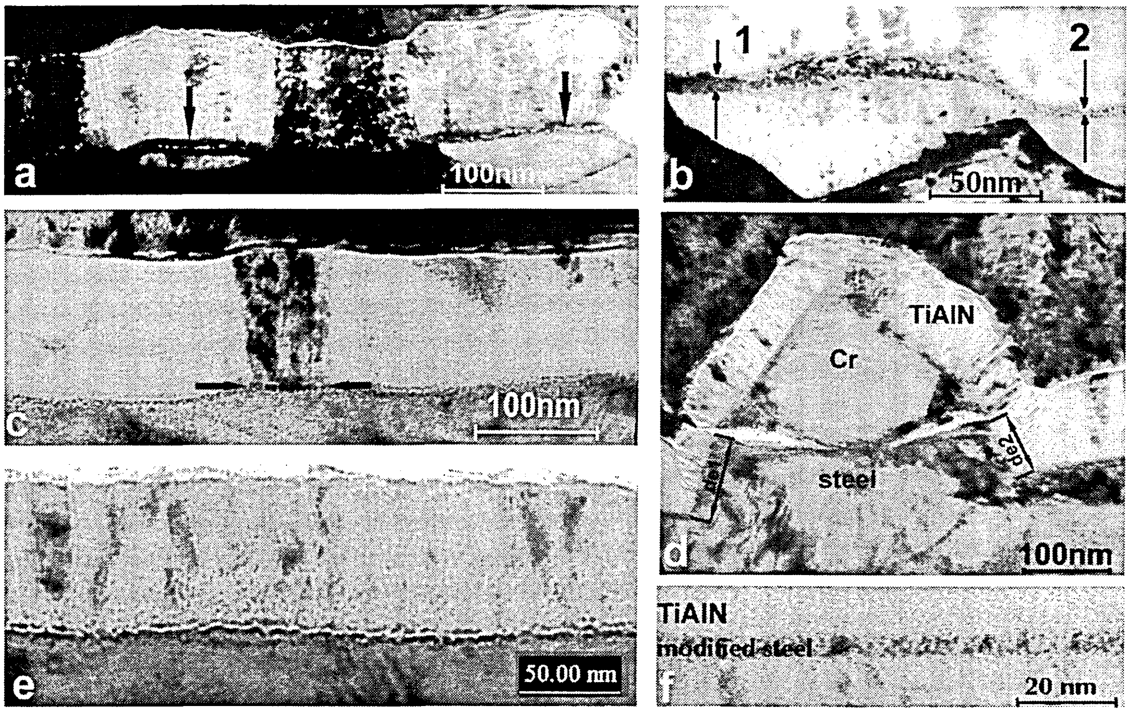

FIG. 2. XTEM images of (a) Cr etch $U_s = 600$ V under-focused such that less dense regions are bright, (b) Cr etch $U_s = 600$ V at higher magnification in over-focused condition such that less dense regions are dark. Note the variation in thickness of the Cr deposition layer in the two regions, (c) Cr etch $U_s = 1200$ V over-focused image without pronounced phase contrast, except in central region, (d) Cr etch $U_s = 1200$ V shows evidence of substrate material removal of ~100 nm, (e) Ar etch $U_s = 1200$ V where a pronounced phase contrast along entire interface indicates low density interface, and (f) higher magnification Cr $U_s = 1200$ V.

uniform crystallographic contrast on micron size areas, indicative of local epitaxial growth on underlying substrate grains. The coating microstructure is further investigated below with cross-sectional and plan view TEM.

STEM-EDX profiles across the interface region taken on different areas of the sample etched with $U_s = 600$ V show significant differences in the Cr distribution as demonstrated in two selected cases. The profile in Fig. 3(a), taken from region 1 in Fig. 2(b), shows a pronounced Cr deposition layer with a thickness of about 10 nm. The STEM-EDX profiling lateral resolution was estimated to be ±2.7 nm from the 15%–85% rise in the Ti and Al profiles in the samples measured in this study which includes possible finite width of the $Ti_{1-x}Al_xN$/substrate interface. Thus, this number is a lower limit for the resolution. In Fig. 3 the width of the Cr/Fe interface is approximately two times broader than the Cr/coating interface. The Cr film is deposited with concurrent energetic ion irradiation, thus the Cr profile gives evidence of a limited mixing and implantation in the substrate in agreement with TRIM[10] simulation. A relatively high Ar level with a maximum concentration of 6 at. % within the deposited Cr layer was detected. It is reasonable to assume that it resides predominantly in the less dense regions, evident in Figs. 2(a) and 2(b).

A STEM-EDX profile taken from region 2 in Fig. 2(b) is presented in Fig. 3(b). The Cr distribution, in agreement with the bright field image, shows that the modified layer thickness is ~5 nm, i.e., a factor of 2 smaller than in region 1. The variation in Cr layer thickness can be explained by the crystallographic dependence of the sputtering yield and Cr sticking coefficient. On grains, exposing crystallographic orientations with higher sputtering yield and lower sticking coefficient values, it will take longer to form a continuous Cr deposition layer, resulting in a thinner layer. In extreme cases even net removal of substrate material at grains with the highest sputtering yield may take place analogous to the selective deposition processes described by Berg *et al.*[11] Increasing the bias voltage to 1200 V results in net etching for all grain orientations.

A typical interfacial composition profile for a sample exposed to $U_s = 1200$ V is shown in Fig. 4(a). The maximum Cr concentration is located within the iron rich region indicating that Cr is implanted rather than deposited. Projected range $R$ and straggle $S$ obtained from TRIM calculations assuming a maximum charge[12] of $Cr^{3+}$ and an acceleration potential of −1200 V are $R = 2.7$ nm and $S = 1.8$ nm. Under these conditions, where the thickness of the etched layer is approximately two orders of magnitude larger than the ion range, implantation profiles can be approximated by error functions extending to a depth of $R+S$, which is in this case 4.5 nm. This is in agreement with the experimental profile when accounting for the lateral resolution of the EDX analysis of ±2.7 nm. Thus, no substantial radiation-enhanced diffusion was observed since it would broaden the Cr distribution beyond the ion-implantation depths. The substrate removal is confirmed by XTEM imaging. Using a droplet which has been deposited during etching as an auxiliary mask, evidence of removal of substrate material of ~100 nm

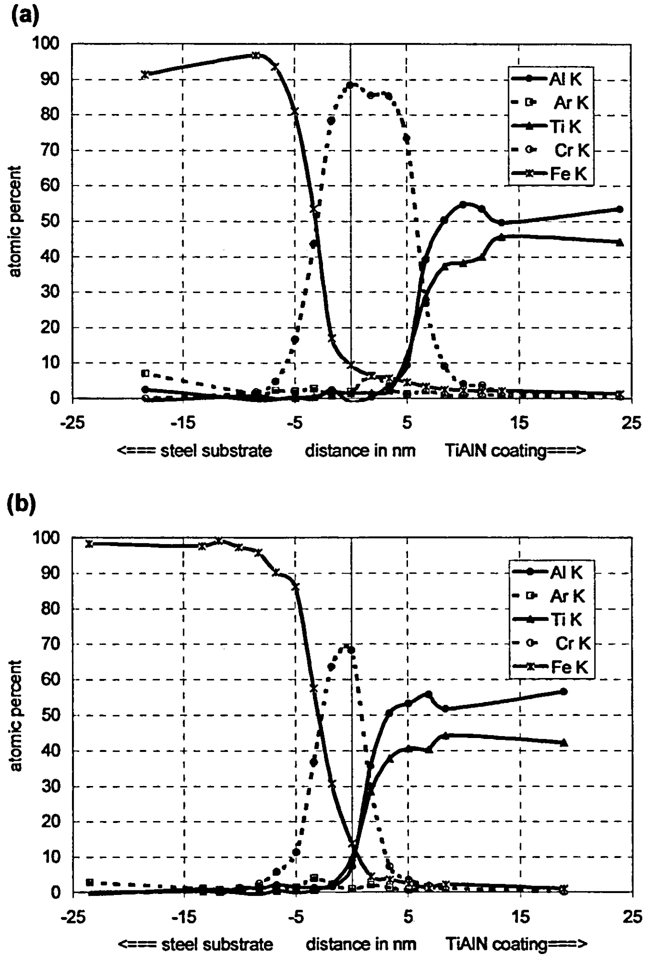

FIG. 3. STEM-EDX profiles of the interface region (a) Cr etch $U_s=600$ V region 1 shows a pronounced Cr deposition layer corresponding to region 1 in Figs. 2(b) and 2(d) Cr etch $U_s=600$ V region 2 with a thinner Cr deposition layer corresponding to region 2 in Fig. 2(b).

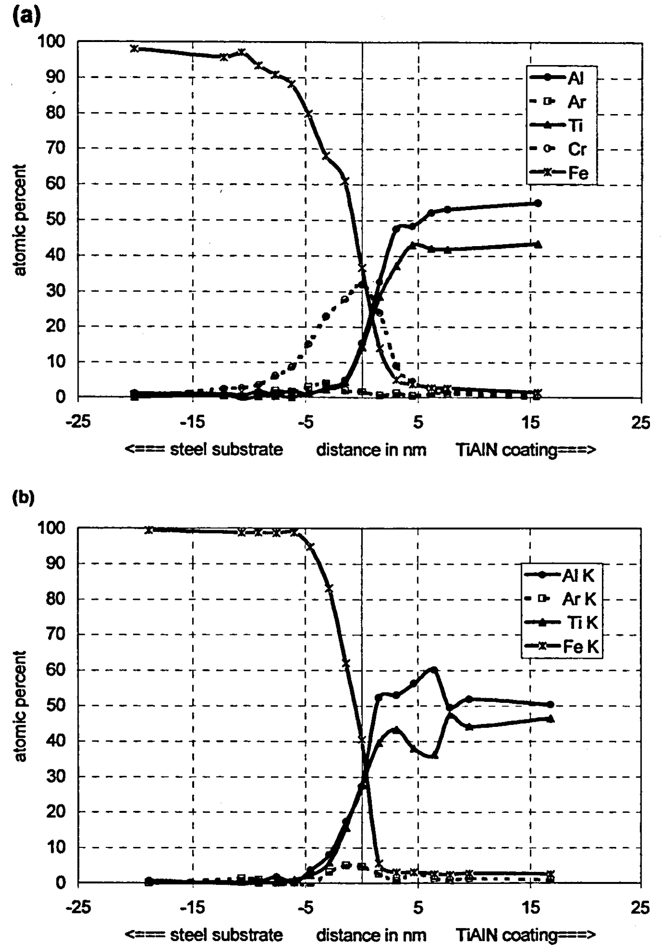

FIG. 4. STEM-EDX profiles of the interface region (a) Cr etch $U_s=1200$ V: The maximum Cr concentration is located within the iron-rich region indicating that Cr is implanted rather than deposited and (b) Ar etch $U_s=1200$ V.

is visible in Fig. 2(d). The substrate beneath the droplet is ~100 nm thicker than the surrounding areas, exposed to further ion bombardment. Since it is not known when the droplet arrived at the surface the steps gives only a lower limit of the etch rate of 5 nm per minute. Figure 2(d) also demonstrates the differences in sputtering yield for different substrate grains. More material is removed ($de_1$ is smaller than $de_2$) on the grain on the left side of the image, since the droplet is located on top of a grain boundary in the substrate. The higher magnification image of the interface region shown in Fig. 2(f) is taken from the etched region of the substrate grain seen on the left side of Fig. 2(d). It is labeled "modified steel" in Fig. 2(f) to be distinguished from the deposited layer in Figs. 2(a) and 2(b). Because of the similar atomic mass of Cr and Fe (52 and 58.9 amu, respectively) the visible contrast cannot be explained by absorption effects and is partially due to local strain fields caused by dislocation cores or defect clusters generated by highly energetic Cr-ion impact. The image presented in Fig. 2(c) was taken in over-focused conditions such that gas inclusions appear dark. The maximum concentration of Ar in this sample is 4 at. % while in the sample etch by $Ar^+$ bombardment this value is 5 at. % as shown in the STEM-EDX profile in Fig. 4(b). Despite the close value of the Ar concentration the modified layer in the Ar etch samples contains visibly more pronounced less dense region in the bright field XTEM images. This is attributed to arise from oxides, which are not removed by Ar pretreatment. Secondary ion mass spectrometry (SIMS) depth profiling confirms an increased oxygen level at this interface.[13]

### B. Microstructure of the $Ti_{1-x}Al_xN$ coating

The microstructure of the $Ti_{1-x}Al_xN$ coatings ranges from competitive columnar growth to local epitaxial growth depending on the substrate surface conditions created by the ion irradiation. In case of $Ar^+$ etching, where oxygen is present at the interface, the nucleation of randomly oriented grains is promoted leading to a competitive column growth with small column size and open boundaries. This can be seen from the bright field (BF) TEM image in Fig. 5(a), which was taken in under-focused conditions such that the open grain boundaries appear bright. The small column size is also reflected by the ring pattern of the selected area dif-

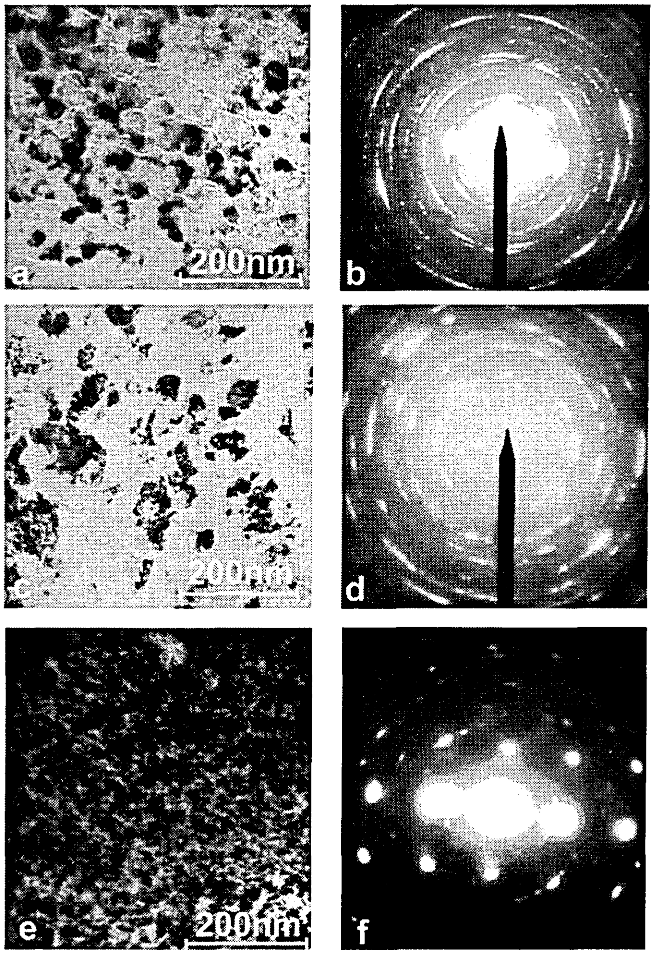

FIG. 5. Plan view and selected area diffraction pattern of Ti$_{1-x}$Al$_x$N coating after (a) Ar etch $U_s$ = 1200 V, (b) polycrystalline SADP taken from (a), (c) Cr etch $U_s$ = 600 V, (d) polycrystalline SADP taken from (c), (e) Cr etch $U_s$ = 1200 V and (f) single crystal SADP taken from (e).

fraction pattern (SADP) in Fig. 5(b) taken from an area of ~1 $\mu$m. A small column size is also typical for Ti$_{1-x}$Al$_x$N grown after Cr bombardment at $U_s$ = 600 V shown in Figs. 5(c) and 5(d). The ring patterns in Figs. 5(b) and 5(d) are not completely uniform and reveal some in-plane orientation, indicative of a limited degree of texture inheritance from the underlying micron-size substrate grains. In contrast the BF TEM image of the Ti$_{1-x}$Al$_x$N coating grown after Cr etching at $U_s$ = 1200 V, which is shown in Fig. 5(e), exhibits the same crystal orientation over the entire region shown in this figure and the corresponding SADP in Fig. 5(f) [same aperture size as in Figs. 5(b) and 5(d)] is of a single crystal character. The lateral extent of the coating grains exceeds several microns and is further illustrated in lower magnification in Figs. 6(a)–6(c). A grain boundary is visible in Fig. 6(a) and Figs. 6(b) and 6(c) represent the dark field (DF) images of the two neighboring grains exhibiting diffraction patterns with a single crystalline nature.

Figures 7(a)–7(f) illustrates the local epitaxy in a cross-sectional view. Figs. 7(a) and 7(b) show convergent beam electron diffractions (CBED) from the film and substrate areas shown in Fig. 7(c). The CBED patterns are indexed in Fig. 7(d) and 7(e) show that [200]TiAlN$\|$[101]$\alpha$-Fe. At the same time the [011] zone axis of the film is within several degrees away from the [$\bar{1}$11] zone axis pattern of the bcc substrate. The observed relationship is therefore consistent with one established in Ref. 5, where the film lattice is 45° rotated around the [001] substrate grain so that the lattice mismatched is decreased from ~31% to ~3% compression. Fig. 7(g) clearly shows that the diffraction contrast in the film grains changes over substrate grain boundaries and is therefore related to crystal orientation of the substrate grain which means that local epitaxial growth occurs for all different substrate grain orientations. The DF image in Fig. 7(f) is taken from the same region as the BF in Fig. 7(c) using the (220) reflection. The uniform contrast here shows again the

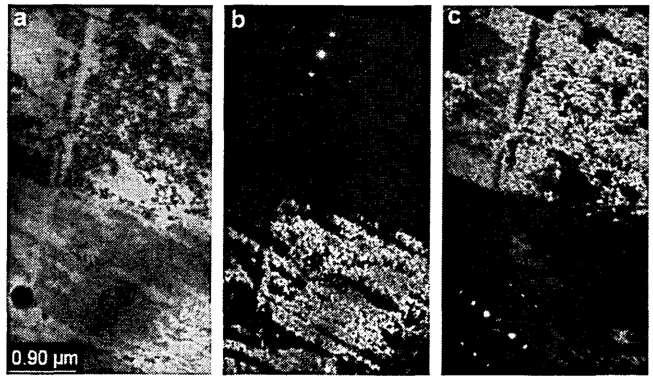

FIG. 6. Plan view Ti$_{1-x}$Al$_x$N after Cr etch $U_s$ = 1200 V at low magnification (a) BF grain boundary, (b) DF and single crystal SADP taken from grain 1 and (c) DF and single crystal SADP taken from grain 2.

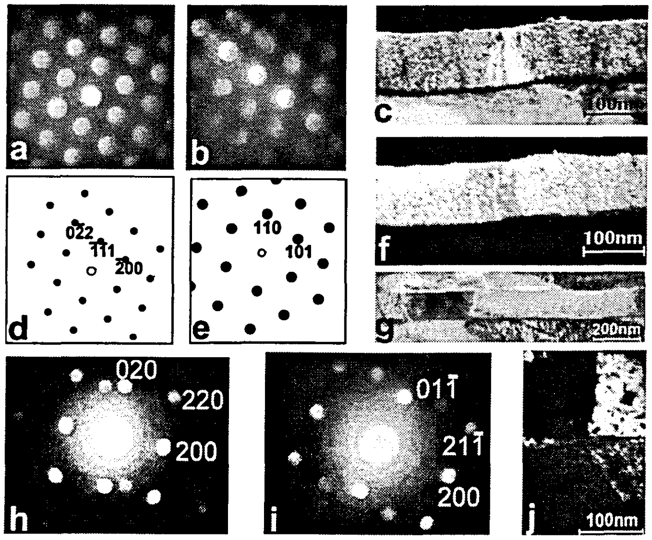

FIG. 7. (a)–(g) XTEM of Ti$_{1-x}$Al$_x$N after Cr etch $U_s$ = 1200 V: (a) CBEDTi$_{1-x}$Al$_x$N, (b) CBED from steel substrate, (c) BF, (d) schematic DP of Ti$_{1-x}$Al$_x$N, (e) schematic DP of steel, (f) DF from (220) reflection, (g) BF shows grain boundary in Ti$_{1-x}$Al$_x$N at same location as grain boundary in steel substrate. (h)–(i) XTEM of Ti$_{1-x}$Al$_x$N after Cr etch $U_s$ = 600 V: (h) CBED of Ti$_{1-x}$Al$_x$N, (i) CBED of underlying steel grain, and (j) DF of Ti$_{1-x}$Al$_x$N(200) reflection.

size of the coating grains as well as the uniform BF contrast in Fig. 2(c). However, a misoriented grain is found on a small region in the middle of the field of view, where a pronounced phase contrast is observed at the interface, demonstrating how crucial a clean substrate surface is in order to obtain local epitaxial growth.

Finally, DF imaging and CBED pattern from the Cr-600 V sample, shown in Figs. 7(h)–7(j) provide evidence of limited local epitaxial relationship between film and underlying substrate grain, in agreement with the plan-view TEM in Figs. 5(c) and 5(d). It is much less pronounced than in the 1200 V case and we assume it occurred in areas with a thinner and cleaner Cr layer as region 2 shown in Fig. 2(b), where substrate grains are oriented favorably for higher sputtering rates. Note that, Cr has a very good lattice match, Fe of 0.8%, and can easily preserve the crystallographic template of the underlying grains.

### C. Interface architecture and adhesion

Scratch tests give a semiquantitative measure of adhesion and the observed failure modes and critical load values can be related to the differences in interface architecture. On Ar-etched samples wedge spallation is observed at a load of 27±3 N. The occurrence of this failure is indicative of a weak interface and strong coating[14] as expected from the low density interface observed in XTEM imaging. In contrast for Cr-ion pretreated samples buckling is observed indicating the presence of a strong interface. Here the localized low density at the interface for $U_s = 600\,\text{V}$ is reflected by a critical load value of 47±5 N in comparison to 63±2 N for the dense interface obtained with $U_s = 1200\,\text{V}$ exhibiting local epitaxial growth of dense layers. This can be understood on the basis of the coherency conditions at the interface. Coherent or semicoherent interfaces as in the case of local epitaxial growth exhibit low interfacial energies in general up to about 200 $\text{mJ}\,\text{m}^{-2}$ for coherent and 200–500 $\text{mJ}\,\text{m}^{-2}$ for semicoherent interfaces.[15] Interfaces with random orientation of the coating, and consequently incoherent, have higher interfacial energies[15] between 500 and 1000 $\text{mJ}\,\text{m}^{-2}$.

## IV. CONCLUSION

(1) Ar etching at $U_s = 1200\,\text{V}$ leads to a low density interface region promoting a competitive columnar growth with small column size and open boundaries resulting in critical load values of 27±3 N.

(2) Cr-ion pretreatment at $U_s = 600\,\text{V}$ leads either to the formation of a Cr deposit resulting in competitive columnar growth with small column size and open boundaries or partially to local oriented growth. The critical load was 47 ±5 N.

(3) Cr-ion pretreatment at $U_s = 1200\,\text{V}$ removes at least 100 nm of the steel substrate and Cr is implanted thus providing a clean substrate surface so that local epitaxial growth can occur. In this case the critical load was evaluated to be 63±2 N.

[1] G. Håkansson, L. Hultman, J.-E. Sundgren, J. E. Greene, and W.-D. Münz, Surf. Coat. Technol. **48**, 51 (1991).

[2] P. J. Martin, in *Handbook of Vacuum Arc Science and Technology*, edited by R. L. Boxman, P. J. Martin, and D. M. Sanders (Noyes, Park Ridge, NJ, 1995), p. 385.

[3] W.-D. Münz, J. Schroeder, H. Peterstein, G. Håkansson, L. Hultman, and J.-E. Sundgren, in *Proc. SURTEC Berlin*, edited by A. Czichos and L. G. Vollrath (C. Hanser, München, 1989), p. 61.

[4] W.-D. Münz, D. Schulze, and F. J. M. Hauzer, Surf. Coat. Technol. **50**, 169 (1992).

[5] I. Petrov, P. Losbichler, D. Bergstrom, J. E. Greene, W.-D. Münz, T. Hurkmans, and T. Trinh, Thin Solid Films **302**, 179 (1997).

[6] W.-D. Münz, I. J. Smith, D. B. Lewis, and S. Creasey, Vacuum **48**, 473 (1997).

[7] S. Creasey, D. B. Lewis, I. J. Smith, and W.-D. Münz, Surf. Coat. Technol. **97**, 163 (1997).

[8] *ASTM Handbook*, Surface Engineering Vol. 51 (ASTM International, Metals Park, OH, 1994), p. 558.

[9] J. Musil, J. Vyskocil, and S. Kadlec, Phys. Thin Films **14**, 79 (1993).

[10] J. Ziegler and J. A. Biersack, *The Stopping and Ranges of Ions in Matter* (Pergamon, New York, 1985).

[11] S. Berg, I. V. Katardjiev, C. Nender, and P. Carlsson, Thin Solid Films **241**, 1 (1994).

[12] I. G. Brown, B. Feinberg, and J. E. Galvin, J. Appl. Phys. **63**, 4889 (1988).

[13] H. Kheyrandish MATS, Warrington, UK (private communication).

[14] S. J. Bull, Tribol. Int. **30**, 491 (1997).

[15] D. A. Porter and K. E. Easterling, *Phase Transformations in Metals and Alloys* (Chapman & Hall, London, 1992), Chap. 3, pp. 142–147.